

STAVEBNÍ OBZOR

číslo 2/2020



Obsah:

12	THE EFFECT OF CONCRETE-STEEL INTERFACE MODEL ON FINITE ELEMENT ANALYSIS OF CONCRETE FILLED SQUARE STEEL TUBE BEAM <i>Mahmud Kori Effendi</i>
13	PERFORMANCE ANALYSIS OF HIGH STEEL TUBE LATTICE SUPPORT SYSTEM IN TYPHOON AREA <i>Shijie Wang, Quansheng Sun, Jianxi Yang</i>
14	EFFECT OF FREEZING AND THAWING ON THE STRENGTH AND DURABILITY OF SANDY SUBGRADE CONTAINING FIBRILLATING NETWORK FIBER FOR PAVEMENT <i>Mohammad Mehdi Khabiri and Bahareh Ebrahimialavijeh</i>
15	STABILITY ANALYSIS OF A ROCKY SLOPE CONSIDERING EXCAVATION UNLOADING EFFECT <i>Chuan Zhao, Linlin Jiang, Xiaopeng Li, Simin Luo</i>
16	CHANGE IN RESILIENT MODULUS OF BASE LAYERS IN ASPHALT PAVEMENT STRUCTURES OVER TEXAS <i>Nitish Raj Bastola, Mena Souliman</i>
17	EFFECT OF VEHICLE QUALITY AND SPEED ON THE IMPACT CHARACTERISTICS OF AN OVERPASS BRIDGE PIER <i>Shijie Wang, Quansheng Sun, Jianxi Yang</i>
18	EXPERIMENTAL STUDY ON THE SEISMIC DAMAGE OF AEOLIAN SAND CONCRETE COLUMNS WITH DIFFERENT REINFORCEMENTS <i>Yaohong Wang, Xiaoyan Ma, Qing Han, Qi Chu, Zeping Zhang</i>
19	ENVIRONMENTAL LEAKAGE POLLUTIONS EVALUATIONS IN URBAN WATER DISTRIBUTION NETWORK USING UNACCOUNTED WATER PRINCIPLES (SHOKHIEH INDUSTRIAL TOWN IN IRAN) <i>Siamak Boudaghpour, Saeideh Sabooteh</i>
20	FIELD LOADING-TEST BASED SHM SYSTEM SAFETY STANDARD DETERMINATION <i>Jiaping Yu, Chunwei Li, Quansheng Sun</i>
21	GEOSPATIAL AND TEMPORAL ANALYSES OF RURAL AREA FOR VEGETATION ANALYSIS <i>Paulina Raeva, Karel Pavelka, Jr.</i>

22	FILTRATION VELOCITY OF WATER IN COARSE PLASTIC PARTICLES Lukaš Svoboda, Tomaš Picek, Štěpan Zrostlik, Mikolaš Kesely
23	DESIGN OF HIGH-SPEED RAILWAY (HSR) LONG-DISTANCE TUNNEL INDEPENDENT CONTROL NETWORK <i>Alhossein Mohamed, Peng Qiyuan</i>

THE EFFECT OF CONCRETE-STEEL INTERFACE MODEL ON FINITE ELEMENT ANALYSIS OF CONCRETE FILLED SQUARE STEEL TUBE BEAM

Mahmud Kori Effendi

Department of Civil Engineering, Faculty of Civil Engineering and Planning,
Universitas Islam Indonesia (UII), Indonesia;
kori.effendi@uii.ac.id

ABSTRACT

Three-dimensional nonlinear finite element (FEA) is developed to predict the experimental behaviour of concrete filled square steel tubular member. The FEA is conducted to determine moment carrying capacity at ultimate load for simple beam. The concrete-steel interface model is the important parameter affecting the result of FEA simulation. Based on the experimental result, there is a local buckling near the loading contact point. To investigate the local buckling phenomenon, concrete-steel interface model is studied by using contact analysis between concrete and steel elements, by using rigid bar element (rbe2 element) and by using interface elements. The geometrical non-linearity, material non-linearity, loading, boundary conditions is the same for all analysis models. To account for all of these properties, FEA model by means MSC Marc Mentat software is developed. The proposed model can predict the ultimate strength with difference only 5-30%. The collapse modes by FEA model are also compared. Based on the numerical analysis, it can be seen that the local buckling is clearly shown in the FEA model with the concrete and steel interface by using interface elements.

KEYWORDS

Concrete filled steel tube, Finite element analysis, Concrete-steel interface

INTRODUCTION

Concrete filled steel tubes (CFST) are composite members comprise of steel tubes with concrete infill. It became popular for modern structural projects. Its ductility is better than conventional structures such as steel and reinforced concrete structures [1-3]. The concrete infill restrains inward buckling of the steel tube, while the steel tubes act as tensile reinforcement for the concrete infill. Studies on flexural behaviour of CFST beam have been conducted by many researchers [4-6]. The concrete infill improves the flexural strength and ductility of structural members of CFST beam as well as to prevent local buckling of steel tubes [7]. A series of experiments of CFST beam with D/t ratios ranging from 74 to 110 is conducted to examine geometrical instabilities.

Finite element analysis (FEA) has been used by many researchers to study the behaviour of CFST beams under pure bending. Karrech et al [8] conducted FEA of cold-formed Circular Hollow Section (CHS) beams filled with concrete subjected to a static plastic pure bending. A damaged plasticity model with softening effect was used for concrete and Von-Miseselasto-plasticity with hardening was used for steel. Three dimensional FEA of concrete filled steel tubes has been used by many researchers, by using ANSYS software [9-11] and by ABAQUS software [12-14].



A Three-dimensional nonlinear finite element (FEA) is developed to predict the experimental behaviour of concrete filled square steel tubular member by using MSC Software, MSC Marc-Mentat [15]. The FEA is conducted to determine moment carrying capacity at ultimate load for simple beam. The concrete and steel material model is modelled by using the nonlinear material. The nonlinear geometry is conducted by means of large displacement analysis. The result of the three-dimensional finite element analysis is then verified against the experimental results by Effendi [16].

The concrete-steel interface model is the important parameter affecting the result of FEA simulation. A Three-dimensional nonlinear finite element (FEA) is developed to predict the experimental behaviour of concrete filled square steel tubular member. The FEA is conducted to determine strength for CSFT simple beam.

EXPERIMENTAL PROGRAM

In order to verify the proposed model, one specimen in total had been tested. The detail of specimen in the experimental study has been shown in Table 1.

Material Properties

The test specimen of square tube, Sfs ($B/t=33.2$), had been tested at the Department of Architecture, Kyushu University [16]. Square shapes of cross section of steel tubular members as well as the specimen length and the position of loading which was analysed in this study is shown in Figure 1. The yield stress of square tubular members was 385 N/mm^2 . The Poisson's ratio, ν is 0.3. Table 1 summarizes the dimensions and material properties.

Experimental Set-up

The test setup for static loading is illustrated in Figure 2. The supports were pin and roller supports at both ends. Roller support was a simple one which was just greased between the bottom end plate of a specimen and testing bed which was made by H-shaped steel, so that specimen ends can freely slide in the member axis direction.

Two displacement transducers were installed to measure the displacement of a loading head, and a laser displacement sensor was placed at the bottom of the mid-span of a tubular member to measure the overall displacement. Strain gauges were installed at the bottom of the mid and quarter span for a square tube.

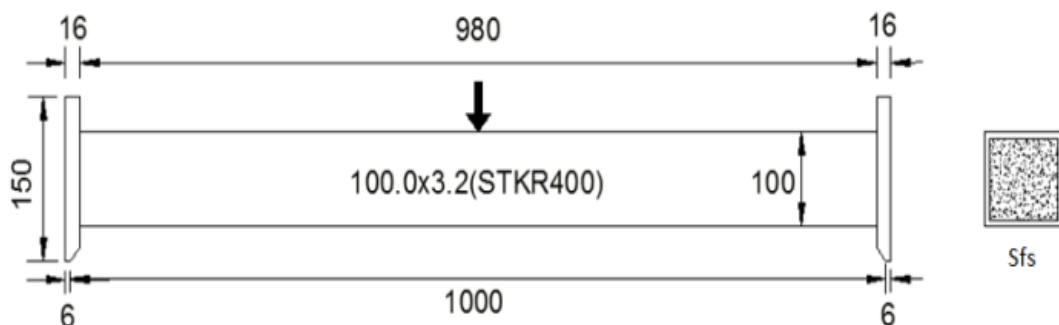


Fig. 1 – Specimen's Illustration (unit: mm)

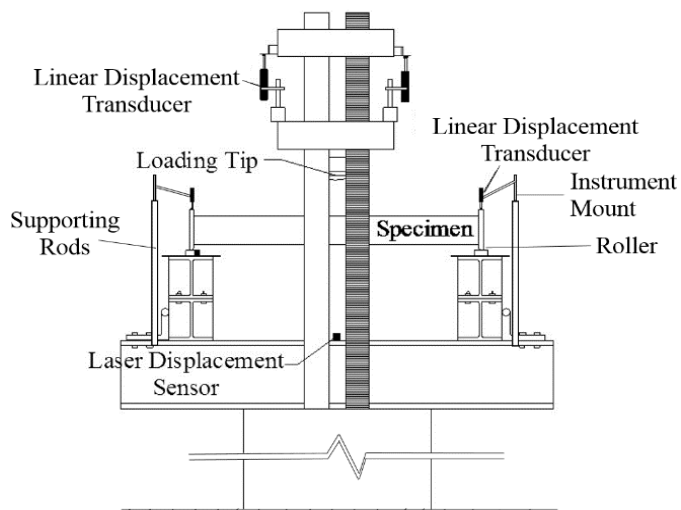


Fig. 2 – Experimental Setup

Tab. 1 - Measured Dimensions and Material Properties of Specimen

Name of Specimen	Steel Tube				Concrete	
	sB (mm)	t (mm)	f_y (N/mm 2)	E_s (N/mm 2)	$c\sigma_B$ (N/mm 2)	E_c (N/mm 2)
Sfs	100.0	3.01	385	188000	71.5	39900

FINITE ELEMENT ANALYSIS

In this study, the commercial software package, MSC Marc-Mentat is used. MSC Marc, general-purpose finite element software, has been used as the analytical tool. MSC Mentat was employed to generate the mesh, material and geometry assignment, loading conditions and boundary conditions. FEM analysis can simulate accurately the response of structure under static loading if the model is used properly. The validity of FEM analysis was justified by comparing with the experimental results. The full Newton-Raphson iterative procedure is chosen to solve the iteration process. The iterative procedure is terminated when the convergence ratio is less than criterion of tolerance, residual checking and displacement checking.

Material Model

MSC Marc [14] requires the stress and strain characteristics to be entered as the true stress and the equivalent plastic strain, respectively. The tensile strength of steel tubes taken from tensile test is represented as in Figure 3. The von Mises yield criterion and the kinematic hardening rule are used as the plastic flow conditions.

The infill concrete is simulated by implementing the Mohr-Coulomb yield criterion combined with the isotropic hardening rule. The concrete model in compressive path is as shown in Figure 4. The tensile model is the cracking stress specified to be a very small value and the tension softening modulus specified to almost zero. The Poisson's ratio is assumed as 0.2.

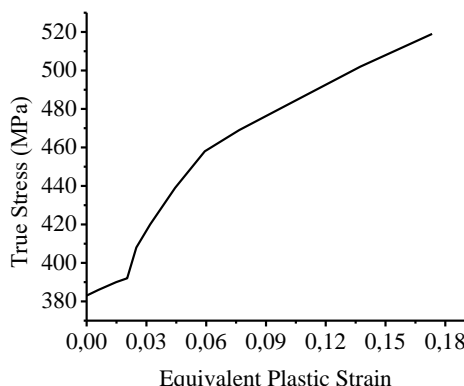


Fig. 3 – .Equivalent Plastic Strain and True Stress Relationships of Steel Tubes

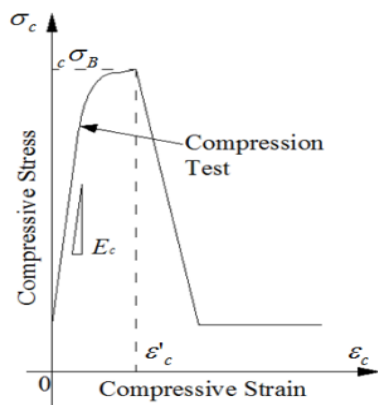


Fig. 4 – Concrete Model in Compressive Path

Element Type, Boundary Conditions and Mesh Segmentation

The FEA model with contact option can be seen in Figure 5 and with interface element can be seen in Figure 6. Both models use the eight-node solid, isoparametric, arbitrary hexahedral element with three degrees of freedom per a node (u , v and w), (the element type 7 of MSC Marc [17], for the analytical model of a steel tubular and concrete elements. While, FEA model with rbe2 element can be seen in Figure 7. The steel used the element type 75 of MSC Marc. The element is a four-node, thick-shell element with global displacements and rotations as degrees of freedom. The coordinates, displacements and the rotations use bilinear interpolation.

The supporting conditions were the simple beam to which the concentrated lateral load applied at the mid-span. The all nodes on both supports were constrained in the direction of Y axis and an additional one node in the mid of the nodes were constrained in the direction of Z axis to stabilize the analysis. The remaining degrees of freedom were set to be free.

The displacements of one node at the bottom of cross section at mid span were constrained in the direction of X axis. The loading tip, which is a rigid body composed of rigid surface elements, applies lateral loads to a steel tube that was composed of deformable elements. The vertical displacement of the loading tip was increased by the displacement control method. With respect to end plate, the shell elements are used with the elastic material properties.

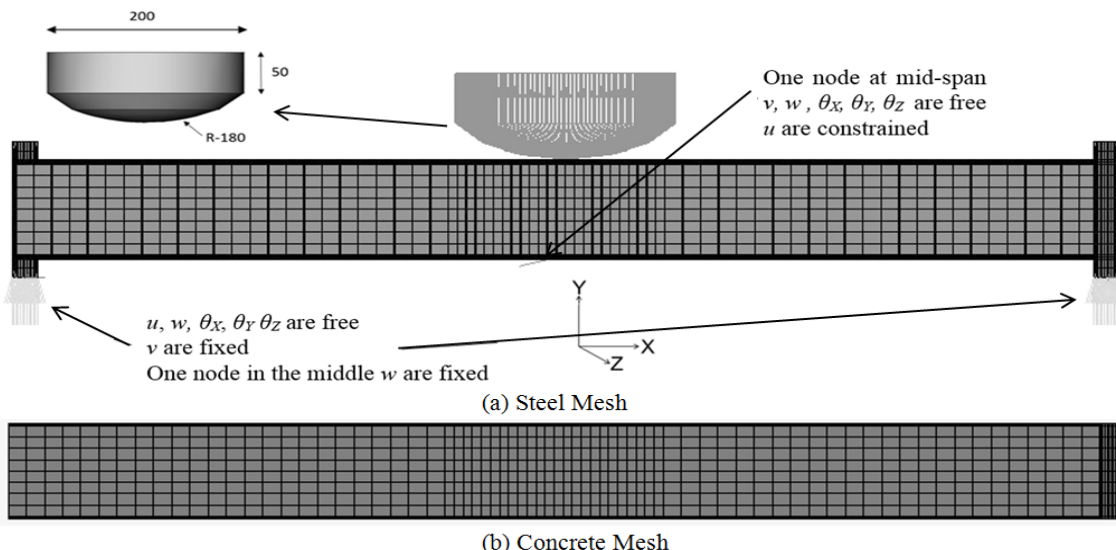


Fig. 5 – Boundary Conditions and Mesh Segmentation with Contact Analysis

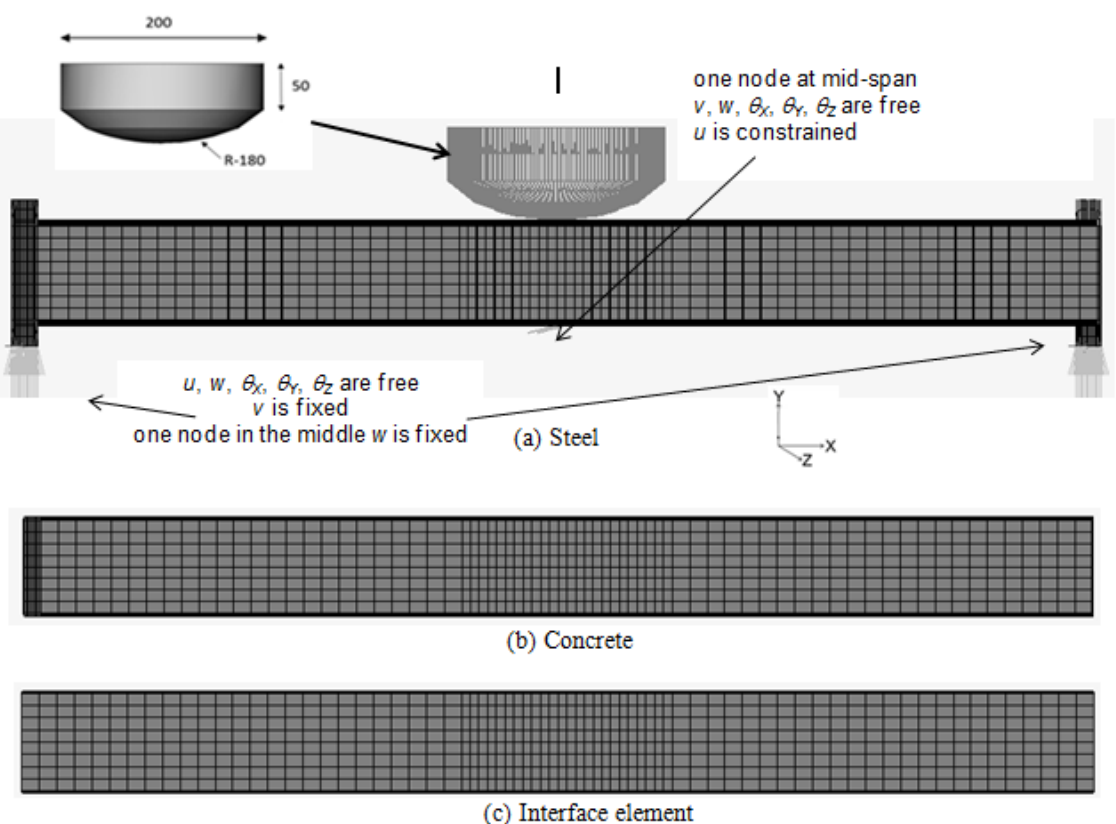


Fig. 6 – Boundary Conditions and Mesh Segmentation with Interface Element

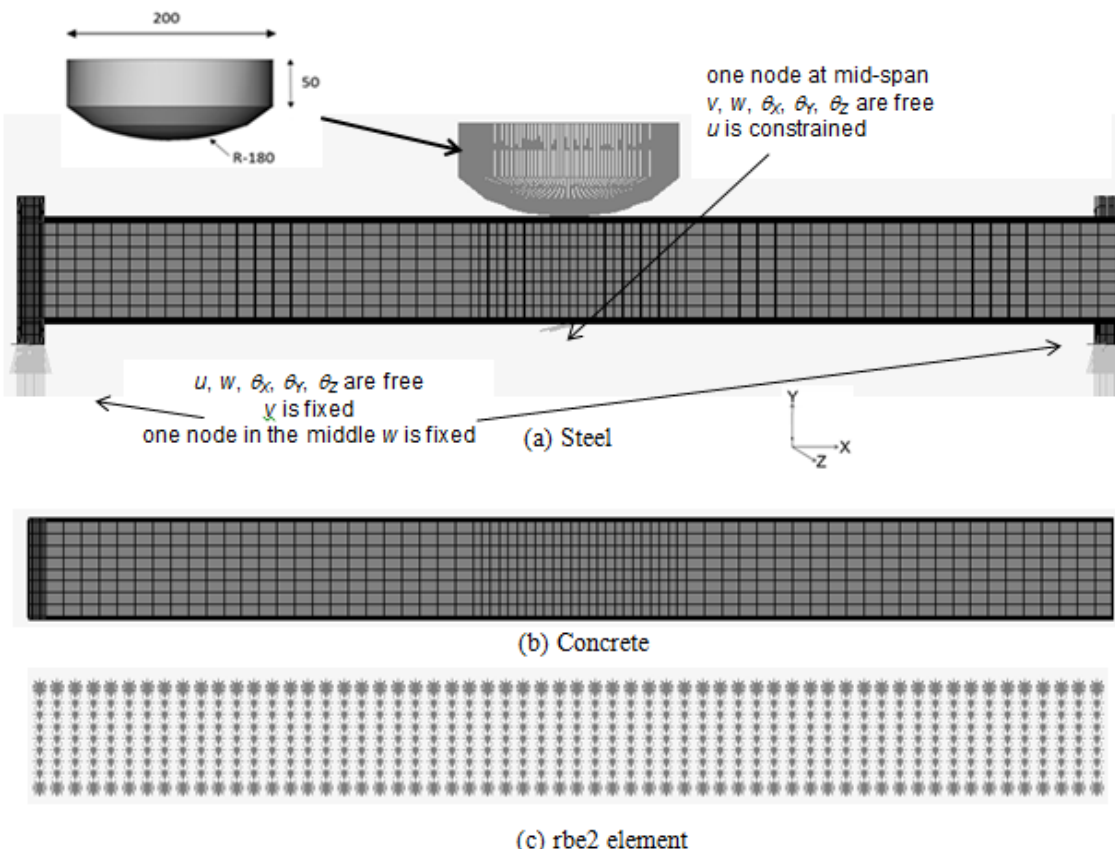


Fig. 7 – Boundary Conditions and Mesh Segmentation with rbe2 element

Contact Analysis

The contact interactions are considered between a rigid body of the loading tip and a deformable body of steel tubular member as well as between steel tubular elements and concrete elements. The contact tolerance of the deformable body was defined to be between plus and minus of 0.1 mm. The MSC Marc deals with the contact analysis by the direct constraint procedure.

Interface Element

The interface element is set between steel elements and concrete elements. The element type 188 of MSC Marc [18], an eight-node three-dimensional interface element, is used to simulate the onset and progress of delamination. The connectivity of the element is shown in Figure 8 where the nodes 1, 2, 3 and 4 correspond to the bottom of the interface and nodes 5, 6, 7 and 8 to the top. The bottom of the interface side is contact with the concrete element and the top is contact with the steel element. The stress components of the element are one normal traction and two shear tractions, which are expressed with respect to the local coordinate system, indicated in Figure 8. The corresponding deformations are the relative displacements between the top and the bottom face of the element. The element is set to be infinitely thin or zero thickness, in which case the faces 1-2-3-4 and 5-6-7-8 coincide.

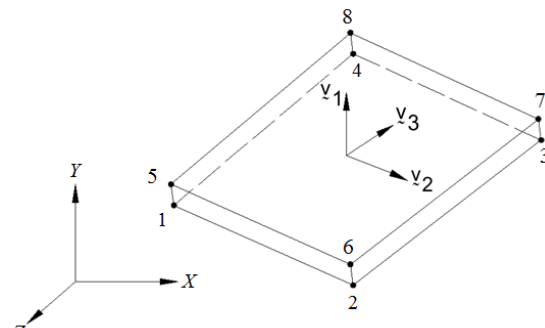


Fig. 8 – The connectivity of the interface element

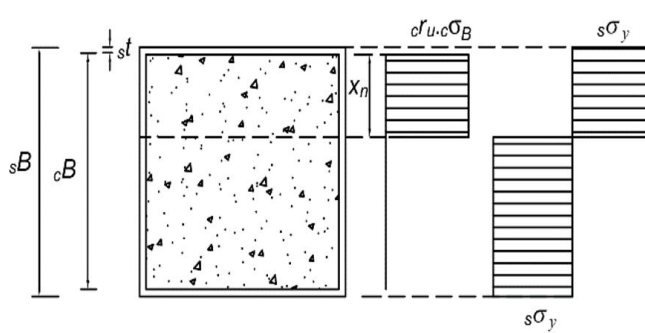


Fig. 9 – Stress Block for CFST Members' Ultimate Bending Capacity

Rigid Bar Element

The rigid bar element (rbe2 element) can be used for connecting two nodes to model a pinned connection with 3 translational DOFs. The connection is between a single retained node with dependent degrees of freedom specified at an arbitrary number of tied nodes. These elements artificially add stiffness by constraining the system to follow a one to one linear displacement and/or rotational relationship between the connected nodes. The distance between the tied nodes to the retained node must be greater than zero. The updated Lagrange is set and large rotation formulation is automatically used in the analysis.

THEORETICAL BACKGROUND

The theoretical value of the ultimate moment, M_u which is the full plastic moment of a CFST member, is based on the Recommendations by AIJ [19], where the stress distributions are assumed as shown in Figure 9. The neutral axis, x_n is obtained by trial and error so the sum of ultimate axial force, Equation (1) close or equal to zero. Then, M_u can be calculated from Equation (2). The concrete and steel tubes contribution in ultimate axial force calculation is determined by Equation (3) and Equation (5). The concrete and steel tubes contribution in ultimate moment is determined by Equation (4) and Equation (6). It was assumed that there was no concrete strength reduction so the value of $c r_u$, reduction factor for concrete strength, is set equal to 1.

$$N_u = {}_c N_u + {}_s N = 0 \quad (1)$$

$$M_u = {}_c M_u + {}_s M_u \quad (2)$$

$${}_c N_u = x_n \cdot {}_c B \cdot {}_c r_u \cdot {}_c \sigma_B \quad (3)$$



$${}_c M_u = \frac{1}{2} ({}_c B - x_n) x_n \cdot {}_c B \cdot {}_c r_u \cdot {}_c \sigma_B \quad (4)$$

$${}_s N_u = 2 (2x_n - {}_c B) {}_s t \cdot {}_s \sigma_y \quad (5)$$

$${}_s M_u = [({}_s B - {}_s t) {}_s B + 2 ({}_c B - x_n) x_n] {}_s t \cdot {}_s \sigma_y \quad (6)$$

The theoretical value of the ultimate strength, P_u , is calculated based on the equilibrium of simple beam as Equation (7). The ultimate strength by FEA and experiment are defined as the point at which the tangent stiffness of the load-deflection curve becomes one-sixth of the initial stiffness as shown in Figure 10 [20].

$$P_u = 4M_u/L \quad (7)$$

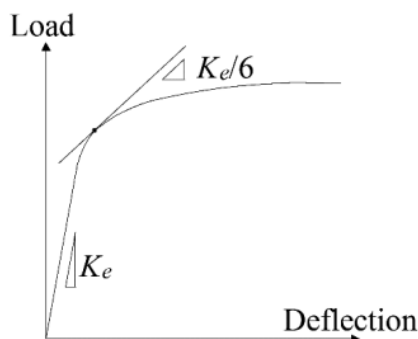


Fig. 10 – Definition of Ultimate Strength by Experimental

RESULTS AND DISCUSSION

Comparison of Load-Deflection Relationships by Experiments and by Finite Element Analysis

In Figure 11, it is seen that the load-deflection curve of the FEA in the elastic range is similar as that of experimental results. However, after the elastic behaviour is extended the FEA using contact analysis is almost the same as that of experimental results. FEA using interface element and using rbe2 element are stiffer than FEA using contact analysis in the initial slope. After the yielding of the steel tube is extended, FEA using rbe2 element did not show strength degradation. The strength is increasing as the deflection is increasing. The rbe2 element increases the stiffness of the specimen.

The dot mark shows the ultimate strength both FEA and experiment. The ultimate strength resulted from the FEA using contact analysis, interface element and rbe2 element have a different value to the theoretical value of the experimental load with 6.5%, 16.7% and 27.3%, respectively as shown in Table 2. While, the ultimate strength resulted from the experimental has a difference value to the theoretical value of the experimental load with 9.3% as shown in Table 2. This proves that the theoretical value is safe for the CFST beam.

Comparison of Load-Strain Relationships by Experiments and by Finite Element Analysis

The strain is taken from the mid of midspan of the specimen. In Figure 12, it is seen that the elastic range of FEA using rbe2 element is stiffer than others. It is caused by the additional stiffness from the rbe2 element. The strain from FEA using interface element is the same as that of

experiment. The strain from FEA using contact analysis is the same as that of experimental in the elastic range, however in the plastic range the strain is lower than that of experiment.

Tab. 2 - Comparison between Ultimate Strengths by Experiment and Theory

		Ultimate Strength (kN)	Ultimate Strength Ratio (%)*)
Theoretical		77.4	100
Experiment		84.6	109.3
FEA	Contact	82.4	106.5
	Interface	90.3	116.7
	rbe2	98.6	127.3

*Ultimate Strength Ratio with respect to Theoretical value (%)

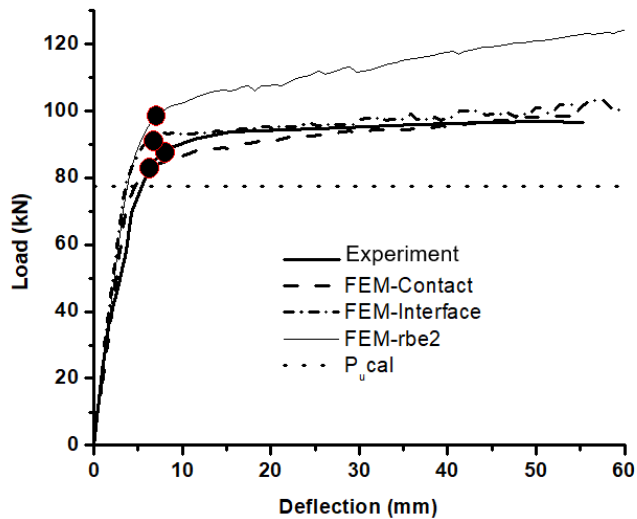


Fig. 11 – Boundary Conditions and Mesh Segmentation with rbe2 element

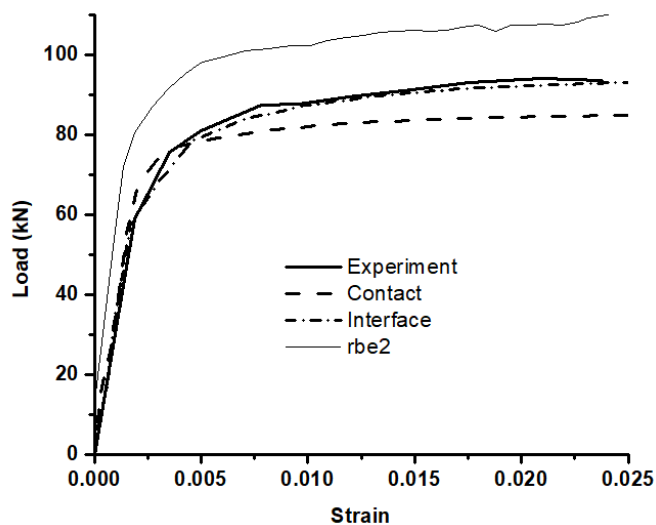
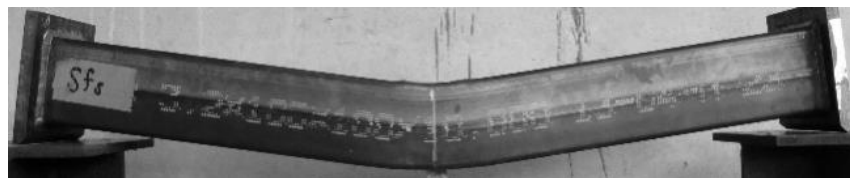


Fig. 12 – Load-Strain Relationships by Experiments and by Finite Element Analysis

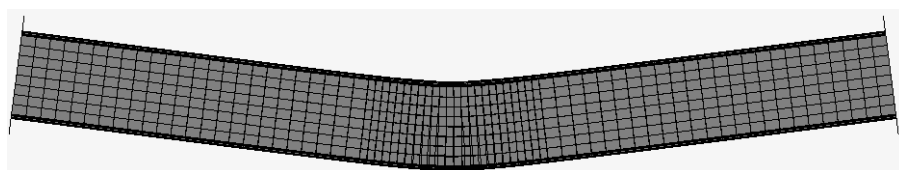


Comparison of Collapse Modes by Experiments and by Finite Element Analysis

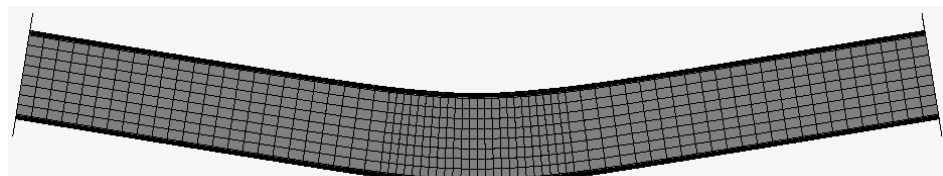
Figure 13(a) and Figure 13 (b-d) show the collapse mode of specimen by experiment and by FEA. It appears that the collapse shape of the FEA results is almost similar to the experimental results. In the experimental results there is local buckling near the loading point as shown in Figure 14(a). FEA using contact and rbe2 element did not show any local buckling near the loading point. However, FEA using interface element shows local buckling near the loading point as shown in Figure 14(b).



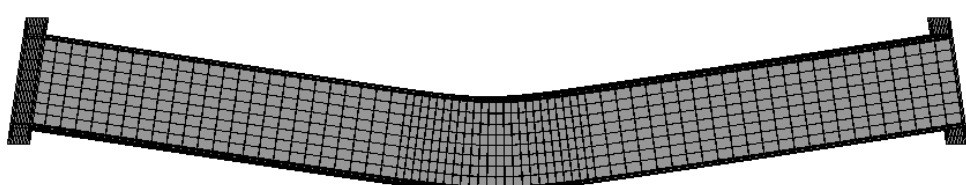
(a) Experiment



(b) Contact Analysis



(c) rbe2 Element

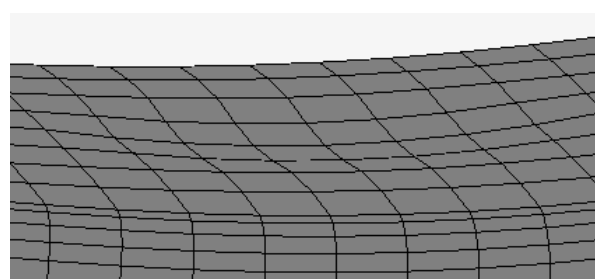


(d) Interface Element

Fig. 13 – Collapse Modes by Experiments and by Finite Element Analysis



(a) Experiment



(b) Interface Element

Fig. 14 – Zoom in of Upper-side of the Beam

CONCLUSION

From the limited research reported in the paper, it can be concluded as follows:

1. The proposed FEA model using interface element and contact analysis can generally model the experiment of the concrete filled steel tube beam. However, the FEA model using rbe2 element is stiffer than others FEA models because the rbe2 element add the stiffness of concrete and steel.
2. The load-deflection results of the FEA model using interface element and contact analysis can be considered coincide with the experimental results. However, FEA model using rbe2 element is higher than others FEA models.
3. The load-strain results of the FEA model using interface element is matching with the experimental results. The strain of FEA model using contact analysis is lower than that of experimental results. The strain of FEA model using rbe2 element is higher than that of experimental results.
4. The collapse modes are basically identical as that of the experimental are almost identical
5. The local buckling of specimen near the loading point can be modelled only in FEA model using interface element.

ACKNOWLEDGEMENTS

We thank to Prof. Akihiko Kawano and Assoc. Prof. Shintaro Matsuo of Department Architecture, Kyushu University for supporting this research through the research facility.

REFERENCES

- [1] Y. Zhang, C. Xu, X. Lu., 2007. Experimental Study of Hysteretic Behaviour for Concrete-filled Square Thin-walled Steel Tubular Columns. *Journal of Constructional Steel Research*, 63(3), 317-325
- [2] Y. C.Tang, L. J. Li, W. X. Feng, F. Liu, B. Liao., 2017. Seismic Performance of Recycled Aggregate Concrete-filled Steel Tube Columns. *Journal of Constructional Steel Research*, 133, 112-124
- [3] X. S.Shi, Q. Y.Wang, X. L.Zhao, F. G.Collins., 2015. Structural Behaviour of Geopolymeric Recycled Concrete Filled Steel Tubular Columns under axial loading. *Construction and Building Materials*, 81, 187-197
- [4] Y. F.An, L. H.Han, C.Roeder., 2014. Flexural Performance of Concrete-encased Concrete-filled Steel Tubes. *Magazine of Concrete Research*, 66(5), 249-267
- [5] G.Li, D.Liu, Z.Yang, C.Zhang., 2017. Flexural Behavior of High Strength Concrete Filled High Strength Square Steel Tube. *Journal of Constructional Steel Research*, 128, 732-744
- [6] C. C.Hou, L. H.Han, Q. L.Wang, C. Hou., 2016. Flexural behavior of circular concrete filled steel tubes (CFST) under sustained load and chloride corrosion. *Thin-Walled Structures*, 107, 182-196
- [7] M. Elchalakani, X. L. Zhao,R. Grzebieta., 2000. Concrete-filled Circular Steel Tubes Subjected to Pure Bending. *Journal of Construction Steel Research*, 57:1141-1168
- [8] A.Karrech, M.Elchalakani, H.Basarir., 2017. Finite Element Modelling of Concrete Filled Steel Tubes Subjected to Static Pure Bending. In H. Hao, & C. Zhang (Eds.),*Mechanics of Structures and Materials XXIV: Proceedings of the 24th Australian Conference on the Mechanics of Structures and Materials* (Vol. 1, pp. 143-148). London
- [9] F. K.Idan., 2017. Finite Element Analysis of Concrete-filled Aluminum tube columns. *International Journal of Applied Engineering Research*, 12(12), 3054-3062
- [10] S.Arivalagan, S.Kandasamy., 2010. Finite element analysis on the flexural behaviour of concrete filled steel tube beams. *Journal of Theoretical and Applied Mechanics*, 48(2), 505-516
- [11] Z.Ting, C.Zhihua, L.Hongbo., 2011. Nonlinear finite element analysis of concrete-filled steel tubular column. In *Electric Technology and Civil Engineering (ICETCE)*, 2011 International Conference on (pp. 2396-2399). IEEE
- [12] P. K.Gupta, H.Singh., 2014. Numerical study of confinement in short concrete filled steel tube columns. *Latin American Journal of Solids and Structures*, 11(8), 1445-1462



- [13] M. H.Mollazadeh, Y. C. Wang., 2014. New insights into the mechanism of load introduction into concrete-filled steel tubular column through shear connection. *Engineering Structures*, 75, 139-151
- [14] Wenchao, L., Wanlin, C., Qiyun, Q., Lele, R. and Ruwei, W., 2018. Study on the Seismic Performance of Recycled Aggregate Concrete-filled Lightweight Steel Tube Frame with Different Assembly Joints. *Civil Engineering Journal-Stavebni Obzor*, 3.
- [15] MSC. MARC., 2012. User's Guide, MSC. Software Corporation
- [16] M. K.Effendi, A.Kawano., 2017. A study on the static and impact structural behavior of concrete filled steel tubular members under Tsunami flotsam collision. In *AIP Conference Proceedings* (Vol. 1818, No. 1, p. 020011). AIP Publishing
- [17] MSC. MARC., 2012. Volume B, MSC. Software Corporation
- [18] MSC. MARC., 2012. Volume A, MSC. Software Corporation
- [19] Architectural Institute of Japan (AIJ)., 2008. Recommendations for design and construction of concrete-filledsteeltubular structures (in Japanese)
- [20] M. Eslami, H. Namba., 2014. Effects of width-to-thickness ratio of RHS column on the elastoplasticbehavior of composite beam, *Memoirs of the GraduateSchools of Engineering and System Informatics Kobe University*, No.6

PERFORMANCE ANALYSIS OF HIGH STEEL TUBE LATTICE SUPPORT SYSTEM IN TYPHOON AREA

Shijie Wang¹, Quansheng Sun¹ and Jianxi Yang²

1. Department of Civil Engineering, Northeast Forestry University, Harbin 150040, China; twfxwsj@163.com; hrbsqs@126.com;
2. College of Civil and Architectural Engineering, Heilongjiang Institute of Technology, Harbin 150050, China; yangjianxi@nefu.edu.cn

ABSTRACT

Research on safety of high steel tube lattice support systems in typhoon areas is still in the preliminary stage. The purpose of this paper is to study the overall buckling and overturning stability of the high steel tube lattice support systems in typhoon area. By constructing the spatial finite element model of the high steel tube lattice support system via MIDAS Civil, the optimal design of the steel tube lattice support system is carried out through the analysis of the main influencing parameters. The stability of steel pipe lattice support system is calculated theoretically, and the optimal design of steel pipe lattice support system is studied by finite element numerical method in Typhoon area. The calculation results show that Critical buckling load coefficient increases with the increase in diameter of the steel tube when the δ/d ratio of steel pipe structure is fixed. The critical load factor of the six-limb support system is slightly larger than that of the four-limb support system. When the transverse space of the support system is from 5 m to 7 m, stability increases rapidly. The best stability of the support system is obtained when the transverse space is approximately 7 m. The diagonal brace can significantly improve the stability of the steel tube lattice falsework.

KEYWORDS

High Steel Tube Lattice Support System, Stability, Finite Element Model, Wind Load

INTRODUCTION

The steel tube lattice support system is widely used in the construction of long-span bridges. However, when the support system reaches a certain height, the entire structure becomes flexible and the mechanical properties become complex. The existing research on mechanical analysis of the double limb lattice column and concrete-filled steel tube of lattice wind tower turbine [1-3] has been carried out. Some scholars also studied the mechanical properties of lattice columns by experimental and numerical methods [4-6]. Some achievements have also been made in the influence of bearing capacity of lattice columns [7] and optimization design of composite tower for large wind turbine systems [8]. Furthermore, the elastic buckling [9-10] and stability of lattice columns is also very important, some research results have also been obtained [11-16].

Under wind load, forced vibration occurs in the high lattice support system, leading to changes in surface pressure that result in vibration effects [17]. Wind load generally consists of mean wind and fluctuating wind loads. Mean wind load can be approximated to the static load acting on the structure, whereas fluctuating wind load causes the dynamic response of the structure [18-19]. The influence of the fluctuating wind load on the structure must be considered; moreover, the load is important to the safety of the flexible lattice support system in typhoon areas [20]. In this study, the influence of wind load on the bracing system of steel tube lattice formwork is



analysed, and the optimisation of the structural system is studied based on the actual project located in the typhoon area with a wind speed magnitude of 14m/s. This paper mainly studies the overall buckling and overturning stability of the high steel tube lattice support systems in typhoon area.

ESTABLISHMENT OF FINITE ELEMENT MODEL

Background

Dalian Island Bridge is located in the central area of Pingtan Strait and 7.85 km from the nearest point of the mainland. The area experiences strong winds all year round and waterways are flooded. The highway part of Dalian Island Bridge is divided into five units. The bridge span arrangement was a continuous beam with dimensions of $4 \times 40\text{ m} + 4 \times 40\text{ m} + 6 \times 40\text{ m} + 5 \times 40\text{ m} + 4 \times 32\text{ m}$. The pier height ranged from 13 m to 50.5 m. The main beam adopted the cast-in-place bracket construction method, which used steel tube columns and the combined structural system of Bailey beam. The flat joint and diagonal bracings between mid-spans were connected by $\Phi 400 \times 8\text{ mm}$ steel tubes. D9#–D19# columns utilised $\Phi 1,200 \times 14\text{ mm}$ steel tubes. Mid-span flat joints adopted $\Phi 720 \times 14\text{ mm}$ steel tubes. Diagonal bracings used $\Phi 400 \times 8\text{ mm}$ steel tubes. In this study, the highest bracket D10#–D11# (61.702 m) segment was selected as the research object. Figure 1 and Figure 2 show the structure form of the bracket and D10–D11 Steel tube lattice support system, respectively.



Fig. 1 - On-site bracket support system

(a)

(b)

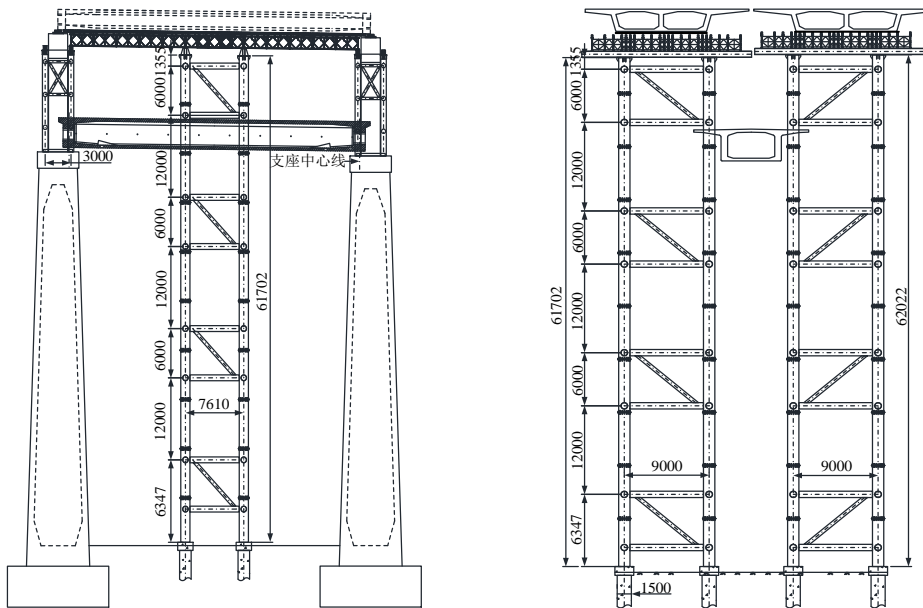


Fig. 2 - D10-D11 Steel tube lattice support system (a) longitudinal and (b) cross-section views

Finite element Model

MIDAS/Civil software was used to establish the finite element model for the high falsework. The model set the node at the connecting point of the member and connection of the foundation. Elements were divided based on the actual steel structure. The high steel tube lattice falsework was composed of 3,688 nodes and 6,993 elements. Bailey beams and steel tube lattice brackets were modelled as truss and beam elements, respectively. Figure 3 and Figure 4 present the falsework finite element discrete model and 3D finite element models of the falsework, respectively. The maximum wind load in the working state of the falsework was considered a grade 8 wind, and the wind speed was 20.7 m/s. The wind load of the nonworking state was considered in the 10-year typhoon period, and the wind speed was 45.4 m/s.

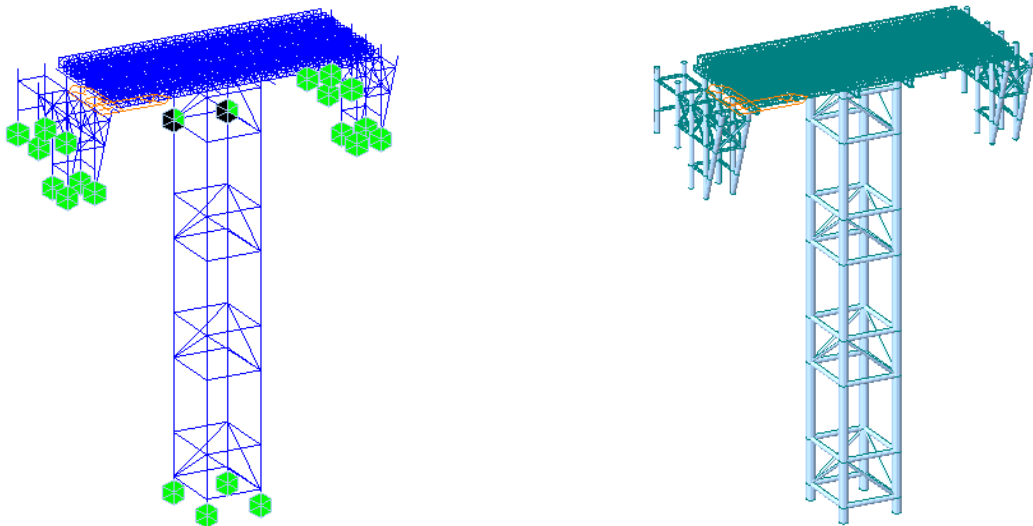


Fig. 3 - Falsework Finite Element Discrete Model

Fig. 4 - 3D Falsework Finite Element model

FORMWORK SUPPORT SYSTEM CALCULATION AND STABILITY ANALYSIS

Details of Formwork support on working stage conditions are shown in Table1.

Tab. 1 - Details on working stage conditions

Condition	Description	Load combination	Purpose
C-I	Shoring tower completed, prior to rebar installation, nonworking stage	$0.9 \times (② + ③ + ⑦)$	Structure and overturning stability verification
C-II	Concrete casting, prior to stretch prestressing, nonworking stage	$1.2 (① + ②) + 0.9 \times 1.4 (③ + ④ + ⑤ + ⑦)$	Shoring tower stability verification
C-III	Concrete casting completed, shoring towers are now load bearing	$1.2 (① + ②) + 1.4 (③ + ⑦)$	Shoring tower robustness verification
C-IV	Normal working stage	$① + ②$	Shoring tower stiffness verification

In Table 1:

- ① Reinforced concrete bulk density of main beam: 26 kN/m³.
- ② Formwork deadweight: 3.0 kN/m².
- ③ Construction crew, materials and construction machines and tool load:
 - a. For shoring column calculations, load was uniformly distributed at 2 kN/m².
 - b. For horizontal and diagonal brace calculation, load as uniformly distributed at 1.5 kN/m².
 - c. Props and other accessory structures were at 1 kN/m².
- ④ Vibration load: Load generated by mixing concrete was 2 kN/m².
- ⑤ Impact load: Impact generated when pouring and casting concrete was 2 kN/m².
- ⑥ Dead weight of falsework system: Bailey beam and steel lattice column were 78.5 kN/m³.
- ⑦ Static wind load: Static wind load was calculated according to 'Load Code for the Design of Building Structures' as follows:

$$w_k = \beta_z \mu_z \mu_s w_0 \quad (1)$$

where:

w_k —standard value of wind load (kN/m²)

β_z —wind vibration coefficient at height z is 1.0

μ_s —wind load shape factor, column and Bailey beams are considered and calculated as round tubes and truss beams, respectively

μ_z —wind pressure height coefficient is 2.12

w_0 —basic wind pressure (kN/m²), $w_0 = v^2 / 1600$



Formwork Support System Design and Calculation

Internal force and stress of bailey beam, cross beam, column and bracket connection system (horizontal and oblique brace) were calculated. Under the most unfavourable circumstances, the maximum axial force of the main chord in Bailey beam, vertical bar and oblique rod were -390.16, -192.13 and 139.15 kN, respectively. The maximum stress of the vertical column, the maximum displacement of the falsework, the maximum sheer force of the connection joints and the maximum stress were -126.81 MPa, 21.46 mm, -150.41kN and -84.14 MPa, respectively. According to design code of steel structures, the design value for the upper and lower chords of Bailey beams, vertical columns and diagonal bracings were 510, 193 and 156kN, respectively. The design compressive strength of grade Q235 steel was 195 MPa. Therefore, actual load as lower than designed bearing load of the structure, and strength of the structure fulfilled the load-bearing requirements.

Stability Analysis

The lattice column at mid-span bears not only the bending moment M_y caused by the asymmetry of the bridge construction but also the bending moment M_x caused by the longitudinal wind load. The lattice column was the crucial part under the eccentric compression state, causing the column to be under the state of bidirectional bending. The stability was related to all three variables N , M_x and M_y . Lattice column falsework section property and internal force calculation results are shown in Table 2 and Table 3.

Tab. 2 - Lattice column falsework section property

A (cm ²)	W (cm ³)	I (cm ⁴)	EA (kN)
522	15,288	1,834,563	1,075,320

Tab. 3 - Lattice column falsework internal force calculation results

Condition	Axle force, N (kN)	Bending moment, M_x (kN·m)	Bending moment, M_y (kN·m)
C-I	1,063	29	102
C-II	4,067	94	148

(1) Working stage condition C-I

At condition C-I, the falsework was completed but under the nonworking state. Overall analysis on buckling and stability was conducted. The results are as follows:

a. Buckling Stability

Slenderness ratio: $\lambda_x = \lambda_y = L/i = 10000/420 = 23.8$, based on type B cross section and stability coefficient $\varphi_x = \varphi_y = 0.957$.

If $E = 206,000,000 \text{ kN/m}^2$, then $A = 0.00522 \text{ m}^2$, $\lambda_x = 23.8$, then N'_{Ex} can be calculated as follows:

$$N'_{Ex} = \frac{\pi^2 EA}{1.1\lambda_x^2} = \frac{\pi^2 \times 206000000 \times 0.00522}{1.1 \times 23.8^2} = 17016 \text{ kN}$$

$$\sigma_1 = \frac{N}{\varphi_x A} + \frac{\beta_{mx} M_x}{\gamma_x W_x (1 - 0.8 \frac{N}{N'_{Ex}})} + \eta \frac{\beta_{ty} M_y}{\varphi_{by} W_y} = 27.7 \text{ MPa} < f = 195 \text{ MPa}$$



$$\sigma_2 = \frac{N}{\varphi_y A} + \frac{\beta_{my} M_y}{\gamma_y W_y (1 - 0.8 \frac{N}{N' E_y})} + \eta \frac{\beta_{tx} M_x}{\varphi_{bx} W_x} = (21.3 + 1.3 + 6.1) MPa = 28.7 MPa < f = 195 MPa$$

Therefore, the falsework is in good stability under this working stage condition.

b. Anti-overturning Stability:

Overturning stability of the shoring tower under nonworking stage was analysed according to the following equation:

$$k = \frac{M_k}{M_q}$$

$$M_k = 6000 \times 30 / 2 = 90000 kN \cdot m$$

$$M_q = M_{formwork} + M_{stent} = 124 \times 60 \times 1.28 + 162 \times 30 \times 1.28 = 15744 kN \cdot m$$

$$k = \frac{90000}{15744} = 5.7 > 1.5$$

The calculated overturning stability coefficient was 5.7, which was significantly larger than that required in the design code. Therefore, overturning stability was high.

(2) Condition C-II

At condition C-II, the beams on top of the falsework completed casting, but prestressing was not stretched and under the nonworking state. The calculation process is as follows:

$$\sigma_1 = \frac{N}{\varphi_x A} + \frac{\beta_{mx} M_x}{\gamma_x W_x (1 - 0.8 \frac{N}{N' E_x})} + \eta \frac{\beta_{ty} M_y}{\varphi_{by} W_y} = 94.8 MPa < f = 195 MPa$$

$$\sigma_2 = \frac{N}{\varphi_y A} + \frac{\beta_{my} M_y}{\gamma_y W_y (1 - 0.8 \frac{N}{N' E_y})} + \eta \frac{\beta_{tx} M_x}{\varphi_{bx} W_x} = 96.4 MPa < f = 195 MPa$$

Stability under condition C-II met the requirement.

OPTIMAL DESIGN OF STEEL TUBE LATTICE FALSEWORK

Influence of Steel Tube Diameter

The falsework column was assumed to have identical cross sections. The force line of the column was consistent with the longitudinal axis of the cross section, and the material was completely uniform and elastic. The critical load of the column could be obtained by using the Euler critical force formula.

The ratio of the wall thickness δ to the diameter d of the steel tube was considered the control parameter. By solving the buckling stability coefficient of columns with different diameter and thickness values, the optimum diameter and thickness were obtained, as shown in Figure 5.

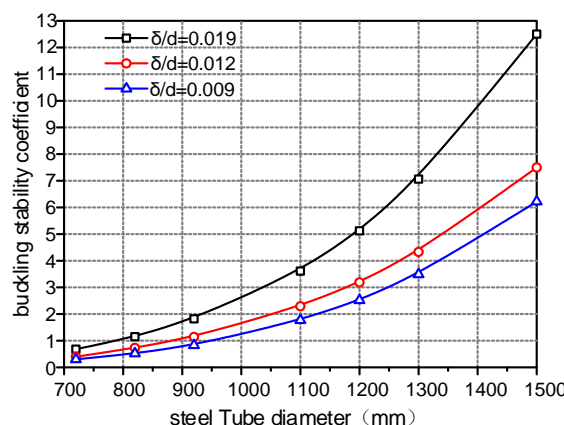


Fig. 5 - Comparison of the different δ/d ratios and buckling coefficients



Figure 5 shows that the critical buckling load coefficient increases at an exponential rate as the diameter of the steel tube increases when δ/d ratio is fixed. When the diameter of the steel tube was constant, the critical load coefficient of the structure increased with the increase in wall thickness. The enlarged diameter of steel pipe increases the change in the critical load coefficient. Therefore, the cross-section size of the structure was the main factor affecting the stability of falsework.

Influence of the number of limbs

According to the design drawings, the falsework was constructed with $\Phi 1,200$ steel tube vertical column, $\Phi 720$ horizontal bracing and $\Phi 400$ diagonal bracing. The influence of steel column number on the stability was studied by establishing the finite element model of single- limb, double-limb, four- limbs and six-limbs falseworks. The buckling diagrams of the different types of steel tube lattice column models are shown in Figure 6. Critical load coefficients of the different types of falseworks are shown in Table 4.

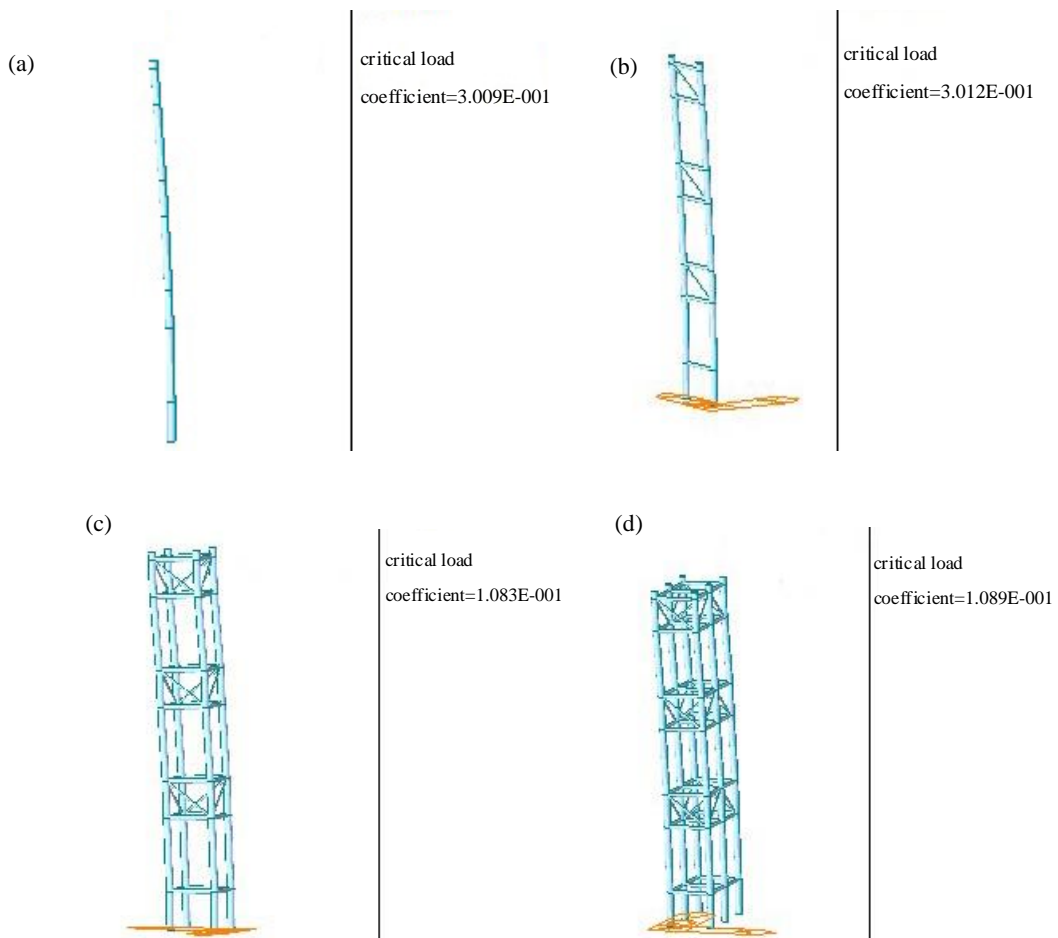


Fig. 6 - buckling diagrams of the different types of steel tube lattice column models

Notes:(a) Single limb; (b) Double limbs; (c) Four limbs; (d) Six limbs

Tab. 4 - Critical load coefficient of the different types of falseworks

Limb(s)	Critical Load Coefficient	Model Diagram	Configuration
Single	0.30	(a)	—
Double	0.31	(b)	9 m spacing
Four	10.83	(c)	9 m transverse, 7.61 m longitudinal
Six	10.89	(d)	2 × 9 m transverse, 7.61 m longitudinal

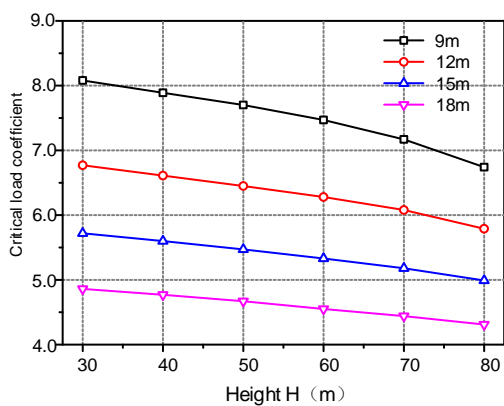
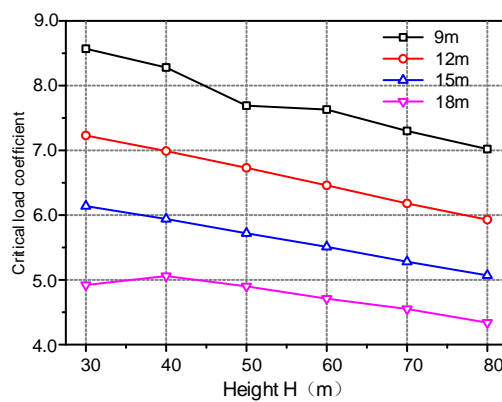
Figure 6 results of buckling calculations and data from Table 4 show the critical load coefficient calculated value of single- and double-limb structures were close, thereby the result indicated that stability of the double-limb structure was almost similar to that of the single-limb structure. However, when the number of limbs increased to four, the critical load coefficient also increased significantly. The stability of the lattice column improved at this time as the resistance to external load also increased. When the number of limbs increased to six, the critical load coefficient increased to less than 4 limbs, thereby indicating that the four-limb steel tubular column was the most cost-effective option.

Influence of Segment length and Height

When the height of the falsework was high, the high falsework was usually divided into segments with lengths of 9, 12, 15 and 18 m. The critical load coefficient at heights 30, 40, 50, 60, 70 and 80 m was analysed, and the critical load coefficient in the first three orders buckling of falsework was obtained. The critical load coefficient of different segment Lengths of falsework is shown in Table 5. Figure 7 and Figure 8 show the first-order and second-order critical load coefficient results at different segment height.

Tab.5 - Critical load coefficient of Different Segment Lengths

Segment Length (m)	Falsework Height (m)	first-order buckling	Second -order buckling	Third -order buckling
9	30	8.08	8.57	11.61
	40	7.89	8.28	11.60
	50	7.70	7.69	11.59
	60	7.47	7.63	11.59
	70	7.17	7.30	11.59
	80	6.74	7.02	11.58
	30	6.77	7.23	10.88
	40	6.61	6.99	10.87
12	50	6.45	6.73	10.86
	60	6.28	6.46	10.86
	70	6.08	6.18	10.86
	80	5.79	5.93	10.85
	30	5.72	6.14	10.39
	40	5.60	5.94	10.37
	50	5.47	5.72	9.46
	60	5.33	5.51	10.36
15	70	5.18	5.28	9.66
	80	4.99	5.07	9.80
	30	4.56	4.92	10.02
	40	4.77	5.06	10.01
	50	4.67	4.90	9.35
	60	4.55	4.71	6.62
	70	4.44	4.55	8.36
	80	4.31	4.34	7.43


Fig. 7 - First-order critical load coefficient

Fig. 8 - Second-order critical Load coefficient

The data from Table 5 show that the critical coefficient of the third-order load is significantly larger than that of the first two-order load at the different segment height, thereby indicating that the structure can hardly reach its third stage of instability. Failure mainly occurred in the first two stages of loading. Figure 7 and Figure 8 illustrate that the critical load coefficient decreases as falsework height increases, thereby indicating poor stability. However, critical load coefficient was guaranteed to exceed 4.0, which satisfied the basic stability requirement when structure segment was not more than 18 m. By contrast, the critical load coefficient decreases drastically when falsework is more than 70 m high. Therefore, in the falsework design, the reasonable segment length and total height of the falsework could be selected based on the different critical coefficients.



Influence of Transverse and longitudinal Spacing

The longitudinal and transverse spacing of a steel tube column was an important parameter that reflected the support area. To study the effect of longitudinal and transverse distances on stability, falsework with segment length and height of 12 and 60 m were used, respectively. With varying transverse and longitudinal spacing, critical load coefficients were calculated. Critical Load coefficient of different spacing of falsework is shown in Table 6.

Tab. 6 - Critical Load coefficient of different spacing

Transverse and Longitudinal spacing	Critical Load Coefficient
5 m × 5 m	5.66
6 m × 6 m	6.20
7 m × 7 m	6.39
8 m × 8 m	6.38
9 m × 9 m	6.26
10 m × 10 m	6.09

Figure 9 shows that spacing and critical load coefficient were set as the x- and y-axes based on the values in Table 6.

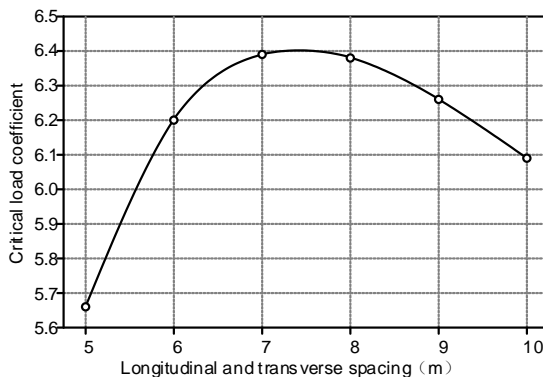


Fig. 9 - Transverse spacing versus critical load coefficient graph

Figure 9 shows that the relationship between the critical load coefficient and the transverse spacing is a parabolic curve. When the latticed column spacing was less than 6 m, the change was rapid and exponential. The rate of increase in the critical load coefficient decreased when the latticed column spacing was 6–7 m. The critical load coefficient reached the peak value at 7 m. The curve reached a plateau immediately after transverse spacing reached 7 m. Therefore, the falsework obtained the most stable and safest condition at spacing of around 7 m.

Influence of Diagonal Bracing

For lattice columns, lateral bracing was essential to maintain its stability, whereas the effect of diagonal bracing must still be determined. Finite element software was used to simulate the influence of braces on the stability of the lattice support. The first three stages of instability modes for structures with and without diagonal braces are shown in Figure 10.

Figure 10 shows that the critical load coefficient of the first-stage load is 6.28 and 4.91 with and without diagonal brace respectively.

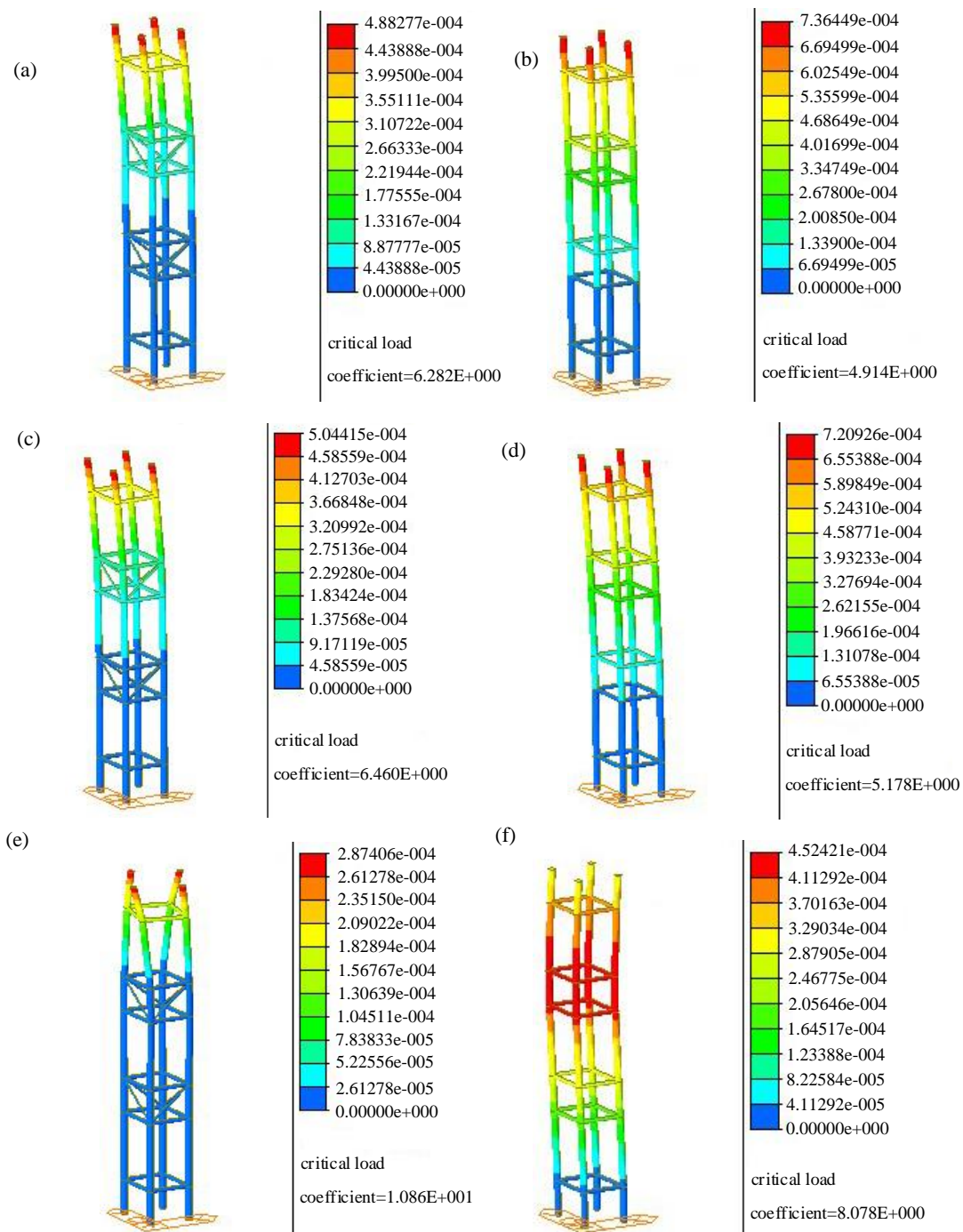


Fig. 10 - Stability of Shoring Tower with and without Diagonal Brace (a) First Stage with Diagonal Brace;(b) First Stage without Diagonal Brace; (c) Second Stage with Diagonal Brace;(d) Second Stage without Diagonal Brace; (e) Third Stage with Diagonal Brace; (f) Third Stage without Diagonal Brace

Figure 10 shows that the diagonal brace increased the critical load coefficient by 27.9%. The critical load coefficient of the second stage was 6.46 and 5.18 with and without diagonal brace, respectively. An increase of 24.7% in the critical load coefficient was not a significant improvement

compared with that of the first stage. The 34.4% improvement in critical load coefficient of the third stage was 10.86 and 8.08 with and without diagonal brace, respectively. Therefore, diagonal bracing significantly improved stability, especially during structure failure under higher orders of loading. Diagonal bracings should be considered an essential component in the design of high steel tube lattice support systems.

CONCLUSION

The finite element model of steel tube lattice column formwork support system in typhoon construction sites is established to ensure that the strength of the support system can meet the design requirements under the most unfavourable load conditions. The falsework-latticed column is simplified as a bidirectional bending member, and the stability of the falsework is calculated. The results show that the falsework meets the stability requirements. The influence of steel tube diameter, limb number, segment length, height, spacing and the presence of oblique braces on the critical load coefficient of the support structure is studied, and the optimal design size of the falsework is obtained. This study can provide a reference for similar types of falsework construction. The main results are as follows:

- (1) When the ratio of wall thickness δ to diameter d of latticed column is fixed, the critical load coefficient increases rapidly with the increase in steel tube diameter d . As δ/d increases, the stability of the falsework is enhanced.
- (2) Four-limb high steel tube lattice column is more stable than double- or single-limb structures, but the difference is not much compared with the bearing capacity of the six-limb structure. Therefore, four-limb high steel tube lattice column is the most cost-effective solution.
- (3) When the total height of the lattice column is constant, the small segment length enhances the stability of the structure, but the total height should not exceed 70 m. When the total height is more than 70 m, the stability of the falsework structure is poor. Considering the economy of the material used for the latticed column, the maximum length of the segment should not exceed 3 times the length of the joint system to ensure the stability of the structure effectively.
- (4) When the longitudinal and transverse spacing of the latticed column falsework is 5–7 m, the stability of the falsework increases rapidly and reaches the peak at around 7 m. When the longitudinal and transverse spacing is greater than 7 m, the stability of the falsework decreases gradually.
- (5) The critical load coefficient of the latticed column is 27.9% higher than that of the non-inclined brace, and the stability of latticed column is significantly improved by using the oblique brace.

ACKNOWLEDGEMENTS

This paper is supported by the Harbin Talent Fund Project (grant number: RC2017QN012019)

REFERENCES

- [1] Li Fengyun. ,2014. Mechanical Analysis of the Double Limb Lattice Column-Bailey Beam Formwork Supports System in Space, dissertation for the degree of master, Chongqing University, Chongqing, pp.55-78
- [2] Liu Xiang,Wang Min,Li Jian. ,2010. The Force Analysis of Concrete-filled Steel Tube of Lattice Wind Tower Turbine, Journal of Wuhan University of Technology, Vol.32 No.9: 175-177.
- [3] Hu Bin, Wu Lin-Zhi,Xiong Jian.,2019.Mechanical properties of a node-interlocking pyramidal welded tube lattice sandwich structure, Mechanics of Materials, No.129: 290-305.
- [4] Xu F, Chen J, Jin W.,2014.Experimental investigation of thin-walled concrete-filled steel tube columns with reinforced lattice angle.Steel Construction, Vol.84:59-67.
- [5] Huang F Y, Yu G, Chen B C , et al.,2014.Experiment Study on Influence of Initial Stress in Concrete Filled Steel Tubular Latticed Columns under Axial Load. Applied Mechanics and Materials, Vol.518:170-177.



- [6] Paluch M J, Cappellari T O, Riera J D.,2007.Experimental and numerical assessment of EPS wind action on long span transmission line conductors. Journal of Wind Engineering & Industrial Aerodynamics,Vol.95 No.7,pp.473–492.
- [7] Yin Haiyun, Yin Haixiong.,2012.The influence of double oblique Bar on the bearing capacity of Lattice columns.Architectural Design Management, No.10:70-72
- [8] Chen Junling, Yang Rongchang, Ma Renle.,2015.Structural Design Optimization of a Composite Tower for Large Wind Turbine Systems.Journal of Hunan University (Natural Sciences), Vol.42 No.5:29-35
- [9] Lan Yong, Guo Yanlin, Chen Guodong. ,2002.Elastic Buckling Behavior of Shuttle-shape Steel Latticed Column. Journal of Building Structures, Vol.23 No.5:18-24.
- [10] Thomas See , Richard E. McConnel. ,1986.Large displacement elastic buckling of space structures.Journal of Structural Engineering,1986, Vol.112 No.5: 1052-1069.
- [11] Tian Wei,Zhao Yang,Xiang Xin-an,Dong Shi-lin.,2010. Stability Behavior of Shuttle-Shaped Steel Lattice Columns With Bending Moment. Journal of Civil, Architectural & Environmental Engineering, Vol.32 No.6:22-27.
- [12] Guo Y , Wang J .,2009.Instability behavior and application of prismatic multi-tube latticed steel column, Journal of Constructional Steel Research, Vol.65 No.1:12-22.
- [13] Zhang Liuyu.,2016. Study on Stability and Status Monitoring Technology of Cuplok Scaffold System in Bridge Construction, dissertation for the degree of doctor, Chang'an University, Xi'an:77-156.
- [14] Yang Chunlai,Wu Qiong. ,2015). Stability calculation of cast-in-situ support for Wulitang right Line extra-large continuous Box girder Bridge, Jiangxi Building Materials, No.04:130-135
- [15] Ma Li. ,2012. Analysis on Dynamic Characteristics and Dynamic Stability of Fastener-style Tubular Formwork Support, dissertation for the degree of master, Chang'an University, Xi'an:45-62.
- [16] Liu Zhifang.,2014.Study on Crucial Technique of Construction Control for Long-span Steel Truss Arch Bridges in Typhoon Area, South China University of Technology: 33-50
- [17] Jiang Jinchen.,2017.Study on Wind-induced response of long-span Pipeline suspension Bridge in Xiaobi River.dissertation for the degree of master, Southwest Petroleum University, Chengdu:59-88.
- [18] Lv Yanxia. ,2013. Dynamic Study on the Wind Load of Steel TV Tower. dissertation for the degree of master, Zhengzhou University, Zhengzhou:19-38.
- [19] Zhao Lin, Ge Yaojun, Xiang Haifan. ,2004.Prediction of Extreme Wind Speed based on Numerical Simulation of Typhoon. Proceedings of the 11th National Conference on structural Wind Engineering:105-110.
- [20] Zhan Yanyan, Zhao Lin, Liang Yuwen. et al.,2017.Comprehensive Assessment of Wind-Induced Interference Criteria about Large Cooling Towers with Typical Six-Towers Double-Columns Arrangements. Engineering Mechanics, Vol.34 No.11:66-76.

EFFECT OF FREEZING AND THAWING ON THE STRENGTH AND DURABILITY OF SANDY SUBGRADE CONTAINING FIBRILLATING NETWORK FIBER FOR PAVEMENT

Mohammad Mehdi Khabiri and Bahareh Ebrahimialavijeh

Yazd University, Faculty of Civil Engineering, Department of Geotechnique and Highway, Yazd, Safiaah, Pajohesh, IRAN; mkhabiri@yazd.ac.ir, bahare.ebrahim71@ymail.com

ABSTRACT

One of the challenges of road construction is encountering soils with lack of required strength and durability. Nowadays, various stabilization techniques are applicable for improving the engineering properties of soils. In the present study, dune sand, as subgrade of pavements, was treated using various contents of fibrillating network (FN) fiber and cement. Dune sand has low bearing capacity that makes it unsuitable for construction activities such as pavement applications. The common solution is improving the strength properties of dune sand so that it can be used for civil engineering projects. Stability of subgrade is very important since the layer provides the stability for the whole pavement structure and the upper layers, namely subbase, base, and asphalt layers. In this regard, compression strength and California bearing ratio (CBR) tests were carried out. Freezing-thawing cycle is one of the most important factors affecting the mechanical properties of soils. Several researchers reported that freezing-thawing cycle could change the physical and mechanical behaviours of soils. The influence of freezing and thawing (up to 18 cycles) on the properties of samples was also studied. Based on the results, the inclusion of FN-fiber to the sand led to increasing the ductility and compressive strength. Also, the addition of cement reduced the ductility, and increased the compressive strength. By increasing the freezing-thawing cycles, the soil strength significantly decreased. Results showed that the stabilized sand soil as subgrade layer led to reducing the compressive strain under the applied wheel load, and therefore reduced the possibility of rutting failure of subgrade.

KEYWORDS

Freezing and Thawing, Sand, Fibrillating network fiber, Cement, Subgrade

INTRODUCTION

Freezing-thawing cycle is one of the most important factors affecting the mechanical properties of soils. Several researchers reported that freezing-thawing cycle could change the physical and mechanical behaviours of soils [1]. These changes may negatively affect the performance of pavement structure including subgrade. It has been reported that cohesion, elasticity modulus, tangent modulus, and compression strength of soils decreased after freezing-thawing process [2,3,4].

Stabilization and reinforcing techniques have been used in road construction projects to improve the strength properties of subgrade. Cement is generally used for improving the stability of subgrade [5]. Cement kiln dust was added to the oil-contaminated sand that resulted in increasing



the compressive strength and bearing capacity. Addition of cement to soils led to increasing the compressive strength, shear strength, and bearing capacity, and also increased the soils brittleness [6,7]. Decreasing the internal water content in the cement stabilized soil resulted in producing higher amounts of calcium carbonate which led to an increase of the compressive strength [8]. In some regions where is the possibility of sulfate attack, cement with lower aluminate content had better engineering performance in stabilization of the sand soil [9].

Inclusion of fiber to soil causes the interlocking between the soil particles and the fiber that results in generation of friction forces. The forces, resulted from interlocking and friction, mobilize the tensile strength in the mixture [10]. It has been reported that by addition of fibers to the soils, the shear and tensile properties, the optimum moisture content, compression strength, and shrinkage limit of the soils increased [11]. By increasing the fiber content, the ultimate bearing capacity improved, and settlements of the footing rested on the fiber-reinforced sand decreased [12]. Addition of fiber to the cement-stabilized soils led to improving the soil strength parameters and also increases the ductility of the samples which is one of the main criteria for flexibility[13]. Resistance to tensile strength is one of the important weaknesses of the soil. The presence of soil-reinforcing fibers increases the shear strength of the soil mixture. These fibers reduce the accumulation of stabilized and hardened soil, increase vulnerability and increase resistance to fatigue and increase the hardness of the mixture. These network fibers as Forta are made from a large number of single-stranded fibers. When these fibers are added to the stabilized soil, due to the mixing and abrasion of the aggregates on top of each other, the structure of these fibers opens from the transverse direction and creates a large number of single strands in the soil, which leads to very good control of primary cracks. Another advantage of these fibers is that they do not absorb water and have a very high resistance in acidic and alkaline environments, which has led to its widespread expansion in recent years. As it was already mentioned, freezing and thawing affect the strength and stability of pavement layers. Several studies have been evaluated the effects of freezing-thawing process on the cement-treated soils; however, very limited information exist about the influences of freezing-thawing process on the cement-fiber-treated dune sand used as subgrade of pavements. Therefore, the aim of this study is to evaluate the effects of cement and fibrillating network fiber on the strength properties of dune sand for pavement subgrade applications. Compression strength and California bearing ratio tests were carried out in the laboratory on the sand samples stabilized with different contents of FN-fiber and cement.

MATERIALS AND METHODS

Sand soil

Based on the AASHTO soil classification, the soil used in the present study was classified as fine sand (A-3). Gradation curve and mechanical properties of the soil are presented in Figure 1 and Table 1, respectively. Figure 1 also shows the compaction test results of the soil. Maximum dry density and optimum moisture content of the sand obtained from Figure 1(b) is also provided in Table 1. Figure 2 shows a view of the sand used and the soil operation volume related to the road construction.

Cement

Chemical additives and possible cementitious additives, including pozzolans and water, are hardened materials with special engineering properties. In this study we will investigate and introduce the application of cement in the road construction industry. In this study, Portland cement type II was also used. Different percentages of cement were added to the soil at 2.5%, 5%, and 7.5% by dry weight of the soil. These contents of cement were previously used by other researchers [14]. Figure 3(a) shows a view of cement used. Chemical compositions of the cement



obtained from XRF results are provided in Table 2. Table 3 summarizes the physical properties of the Portland cement.

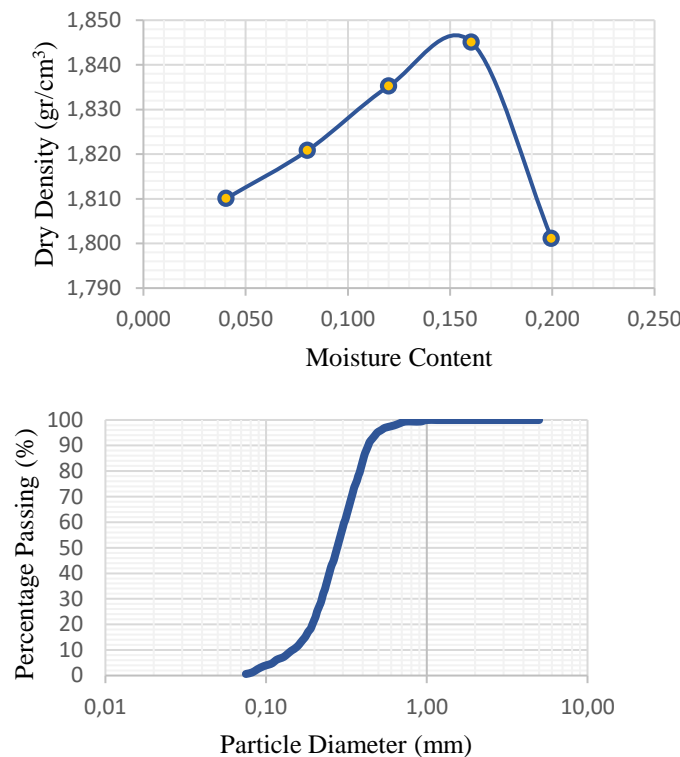


Fig. 1- Gradation curve(above), and compaction test results of the soil (below).



Fig. 2- A view of the sand collected from the planned site for the construction of the pavement.

Tab. 1 - Mechanical properties of the sand soil.

Parameter	Content	Unit	Standard used
Soil classification	A-3	-	AASHTO M 145 or ASTM D3282
G_s	2.7	-	ASTM D-854
CBR	28.5	(%)	ASTM D-1883
C	0.1	(kPa)	ASTM D-3080
ϕ	46	(degree)	ASTM D-3080
ω_{opt}	16	(%)	ASTM D-698
γ_{max}	1.845	(g/cm ³)	ASTM D-698



Fig. 3 - A view of the Portland cement type II (left), and FN-fiber (right)

Tab. 2 - Chemical compositions of the Portland cement type II used in the experiments.

Chemical compositions	Percentage (%)
SiO ₂	20
Al ₂ O ₃	6
Fe ₂ O ₃	6
MgO	5
SO ₃	3
LOI	3
Insoluble residue	0.75
C3A	8

Tab. 3 - Physical properties of the Portland cement.

Physical properties	Value
Specific area of 1 cm ² /g	2800
Expansion of autoclave test (%)	0.8
Setting time with Vicat method	
Initial (min)	45
Final (hour)	6
Compressive strength (kg/cm ²)	
3 day	100
7 day	175
28 day	315
Hydration heat (Cal/g)	70

Fibrillating Network Fiber

The fiber used in the present study is classified as Fibrillating Network fiber (FN-fiber), which was added to the soil by 1%, 1.5%, and 2.5% by dry weight of the soil. Similar contents were also used by other researches [15]. In this study, a commercial fiber, known as "Forfa" fiber, was used. Table 4 shows a view of the FN-fiber and its properties, respectively. Compared to two-dimensional fibers, 3D fibers can be used in advanced technologies due to their properties such as thickness, shear strength, tear tolerance and damage that are important for many applications. In addition, its multi-directional structures can lead to increased stiffness and strength characteristics by further strengthening the thickness. Soil and fiber mixture samples. Compression strength test was conducted based on ASTM C-109 standard. Compressive strength was measured using 2 kN loading capacity compression device. To investigate the effects of freezing and thawing process on the strength properties of the samples, different cycles of freezing-thawing were considered based on ASTM D-560 standard. Bearing capacity of the soils is one of the effective and important parameters in road and pavement constructions. For this purpose, California bearing ratio (CBR)

test was conducted based on ASTM D-1883 standard. Compressive strength experiment, measuring deformation in the failure moment and the California bearing ratio for samples with different content of cement and FN-fiber was carried out. FN-fiber in 1%, 1.5% and 2% and cement in 2.5%, 5% and 7.5% by the dry weight of soil are added to the soil. For constructing sample, sand, given the desired frame volume and calculated density in compaction experiment, cement and FN-fiber in defined weight ratio respect to dry weight of soil are weighed and used. The mentioned materials with optimum moisture content plus the same content of cement, water were added and were mixed to obtain the uniform and homogeneous mixture. Resulting compound is molded and compacted. For curing, it was kept in the enclosure to perform the chemical reaction of the cement in the compound and to increase the strength of the samples, for three days and then was experimented [16]. Figure 4 shows an image of samples used in the experiment.



Fig 4- Stabilized sand samples with cement and reinforced with FN-fibers (right). Close view of reinforced and stabilized samples (left)

RESULTS AND DISCUSSION

Compressive Strength and Deformation Experiment

Compressive strength and deformation in the failure moment of soil mixed with cement and FN-fiber were measured. Addition of FN-fiber and cement, will improve the sand soil strength. In Figure 5, the view of how the fiber and soil are interlocked is shown. FN-fiber in soil are deformed after applying the normal force and the interlocking created between soil particles and fiber in this stage and also the friction force between soil particles mobilized the tensile force in fiber and increase the compressive strength [17]. In Figure 7 and Figure 8 the simultaneous effect of cement and FN-fiber on the compressive strength and deformations is shown. In fixed FN-fiber content, by increasing the cement content, the compressive strength and deformation are increased and reduced, respectively. In fixed cement content, by increasing the fiber up to 1.5 %, the compressive strength increased and after this content reduced. Therefore, fiber content up to optimum amount will lead to increase in compressive strength [18]. But, the amount of change of deformation shows an incremental trend by increasing the FN-fiber content. Therefore, according to Figure 6, maximum compressive strength is obtained in 7.5 % of cement and 1.5 % of FN-fiber. In Figure 7, soil mixed with the minimum amount of cement and the most FN-fiber has the maximum deformation.



Fig. 5 - The view of how FN-fibers and soil interlocked, application of FN-fibers for preventing crack in loading moment

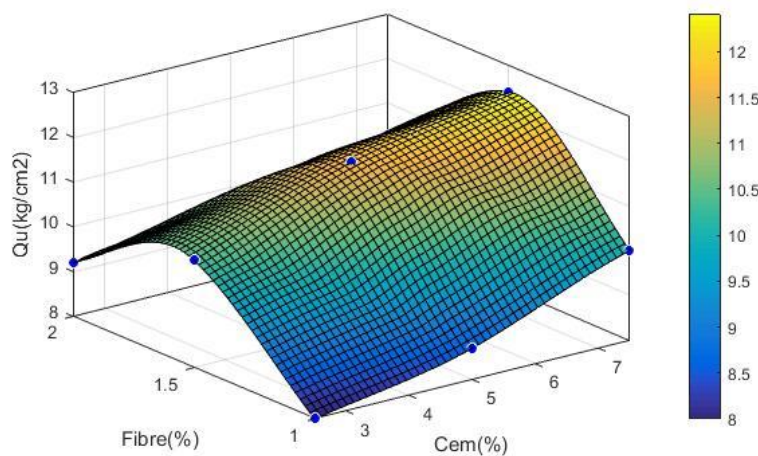


Fig. 6 - Investigation of the simultaneous effect of FN-fibers and cement on the compressive strength of modified sand soil

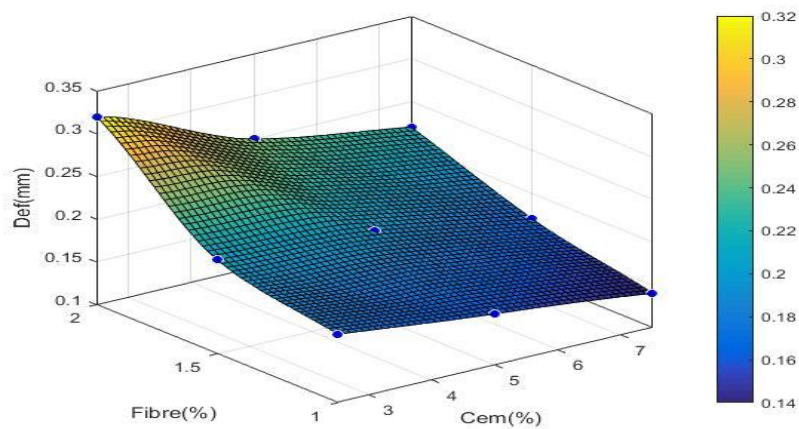


Fig. 7- Investigation of the simultaneous effect of FN-fibers and cement on soil deformation

CBR Test

In order to more proper investigation of efficacy of this type of soil improvement in road construction, CBR test was used. Figure 8 shows the effect of simultaneous mixture of cement and FN-fiber on the CBR value and as can be see, in fixed FN-fiber content, increasing the cement content, the value of the California bearing ration is increases too. Increasing the FN-FN-fiber content, in fixed content of cement, lead to decrease in California bearing ratio. According the result obtained from previous deformation experiment, this result seems acceptable. Therefore, maximum amount of California bearing ratio same as deformation in previous section is obtained in mixing soil with minimum FN-fiber content and maximum cement content.

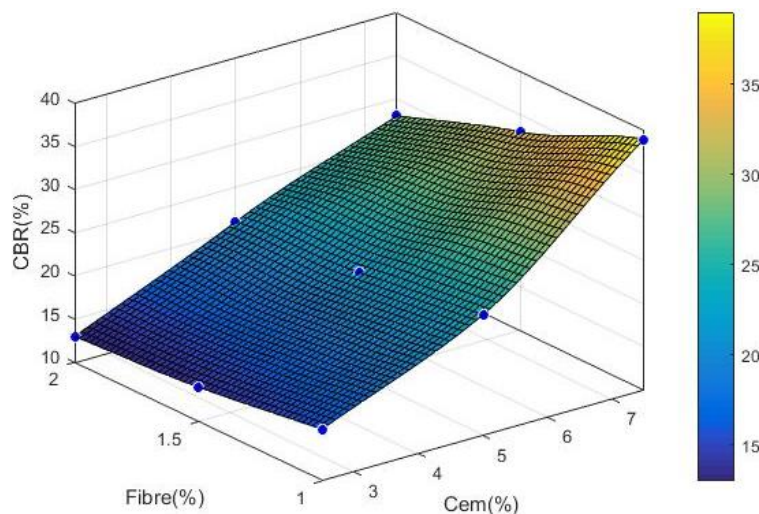


Fig. 8 - Investigation of the simultaneous effect of FN-fibers and cement on CBR

Figure 9 shows the changes of soil elasticity module in simultaneous mixing of cement and FN-fiber. Some researchers in their researches sought to find the relation between California bearing ratio and modulus of elasticity [19]. In all available relation, the California bearing ratio and elasticity modulus have direct proportion. Therefore, by increasing the cement ratio, the elasticity modulus of soil increases too and the maximum value of elasticity modulus in soil mixed with maximum cement content and minimum FN-fiber content is achieved.

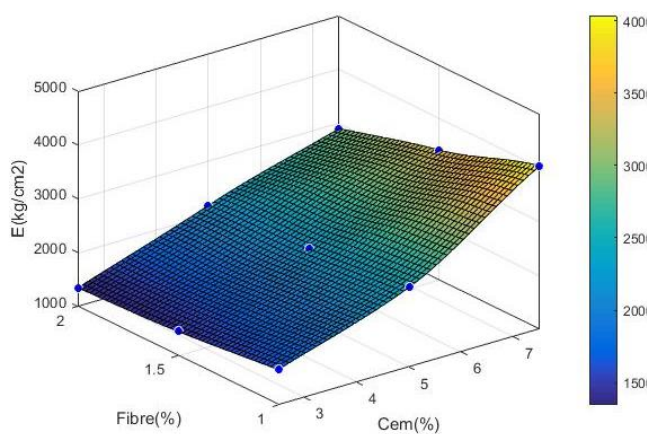


Fig. 9 - Investigation of the simultaneous effect of FN-fibers and cement on elasticity modulus

Freezing-Thawing Cycle

Another parameter investigated in the present study, is the strength loss due to applying freezing-thawing cycle. Results are shown in Figure 10. The standard for carrying out the experiment is ASTM D-560. According to that freezing-thawing cycle in sand subgrade, specifically in desert areas is limited and small, the few cycle numbers are selected for the present study. As can be seen, increasing the number of freezing-thawing cycles, will increase the strength loss. Such that, up to 25 percent of strength of stabilized layer will reduce. Past research has shown similar results, with the use of the freeze-thaw cycle significantly reducing soil stability. [20]. Gazavi and Rostaie, (2010) showed that increasing the number of freezing-thawing cycle, results in decrease of compressive strength of soil and stabilized soil up to 20-25 percent [21].

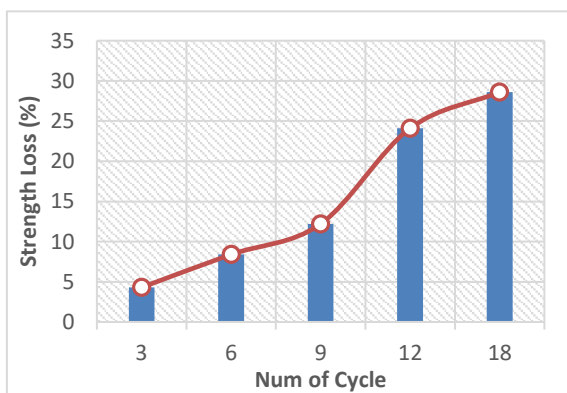


Fig. 10 - The effect of number of freezing-thawing cycle on the amount of strength loss

CONCLUSION

With aim of increasing the durability and the strength of sand bed and improving the pavement, cement and FN-fiber were used in different content. In order to investigate the effect of this type of improvement on the performance of sand layer in the road pavement, compressive strength, deformability and California bearing ratio were measured and finally, the results were used in software analysis. The obtained results are as follows.

1. Adding cement and FN-fiber to soil, improved the compressive strength of soil. In fixed FN-fiber content, by increasing the cement content, compressive strength was increased up to 25 percent. In fixed cement content, increasing the FN-fiber content up to an optimum value, increased the compressive strength, and by further increase compressive strength decrease.
2. In fixed cement content, by increasing the FN-fiber content, deformation in the failure moment increases and in fixed FN-fiber content, by increasing the cement content, deformation reduces, and in other words, the presence of FN-fiber results in the ductile behaviour of the stabilized layer.
3. Minimum FN-fiber ratio and maximum cement content, results in maximum California bearing ratio and elasticity modulus. Compare with Primary pure soil, in this case the California Bearing Ratio and elasticity modulus tripled.
4. Applying freezing-thawing cycle, reduced the soil strength and by increasing the number of cycles the rate of this reduction of strength increases. So that, the initial resistance of the sample is reduced up to 25%.

ACKNOWLEDGEMENTS

This research was supported by Research Deputy of Yazd University under "Pajohanah Contract" No. 98/p/2187 dated 11/4/2019. It is also thanked by "Forta" Sirjan Company for providing fibers.

REFERENCES

- [1] Zhang W, Guo A, Lin C. Effects of Cyclic Freeze and Thaw on Engineering Properties of Compacted Loess and Lime-Stabilized Loess. *Journal of Materials in Civil Engineering*. 2019;31(9):04019205.
- [2] Xu X, Li Q, Lai Y, Pang W, Zhang R. Effect of moisture content on mechanical and damage behavior of frozen loess under triaxial condition along with different confining pressures. *Cold regions science and technology*. 2019; 157:110-118.
- [3] Khabiri, M. M. (2010). The effect of stabilized subbase containing waste construction materials on reduction of pavement rutting depth. *Electronic Journal of Geotechnical Engineering*, 15, 1211-1219.
- [4] Saberian, M. and Khabiri, M.M., 2017. Experimental and numerical study of the effects of coal on pavement performance in mine haul road. *Geotechnical and Geological Engineering*, 35(5), pp.2467-2478.
- [5] Saberian, M., & Khabiri, M. M. (2018). Effect of oil pollution on function of sandy soils in protected deserts and investigation of their improvement guidelines (case study: Kalmand area, Iran). *Environmental geochemistry and health*, 40(1), 243-254.
- [6] Jamshidi Chenari R, Fatahi B, Ghorbani A, Alamoti MN. Evaluation of strength properties of cement stabilized sand mixed with EPS beads and fly ash. *Geomechanics and Engineering*. 2018;14(6):533-544.
- [7] Jiang Y.N., Chen S. , (2019), Study on the formation mechanism of bonding layer around pile body in soft clay, *The civil engineering journal* ,3-2019. 386-397. DOI 10.14311/CEJ.2019.03.0031
- [8] Si Ho L, Nakarai K, Ogawa Y, Sasaki T, Morioka M. Effect of internal water content on carbonation progress in cement-treated sand and effect of carbonation on compressive strength. *Cement and Concrete Composites*. 2018;85:9-21.
- [9] Liu K, Wang Y, Jiang NJ, Wang A, Sun D, Chen X. Effect of aluminate content in cement on the long-term sulfate resistance of cement stabilized sand. *Marine Georesources & Geotechnology*. 2019; 1-10.
- [10] Rajeswari JS, Sarkar R, Roy N, Bharti SD. Bearing capacity of circular footing supported on coir fiber-reinforced soil. *International Journal of Geotechnical Engineering*. 2019;13(3):218-26.
- [11] Janalizadeh Choobbasti A, Kutanaei SS, Ghadakpour M. Shear behavior of fiber-reinforced sand composite. *Arabian Journal of Geosciences*. 2019; 12(5):157.
- [12] Sotomayor JM, Casagrande MD. The performance of a sand reinforced with coconut fibers through plate load tests on a true scale physical model. *Soils and Rocks*. 2018;41(3):361-8.
- [13] Malidarreh N, Shooshpasha I, Mirhosseini S, Dehestani M. Effects of reinforcement on mechanical behaviour of cement treated sand using direct shear and triaxial tests. *International Journal of Geotechnical Engineering*. 2018;12(5): 491-499.
- [14] Albusoda BS, Salem L, Salem K. Stabilization of dune sand by using cement kiln dust (CKD). *Journal of Earth Sciences and Geotechnical Engineering*. 2012; 2(1):131-143.
- [15] Ateş A. Mechanical properties of sandy soils reinforced with cement and randomly distributed glass fibers (GRC). *Composites Part B: Engineering*. 2016; 96: 295-304.
- [16] Umesha, T. S., Dinesh, S. V., & Sivapullaiah, P. V. (2009). Control of dispersivity of soil using lime and cement. *International journal of geology*, 3(1), 8-16.
- [17] Gowthaman S, Nakashima K, Kawasaki S. A state-of-the-art review on soil reinforcement technology using natural plant fiber materials: past findings, present trends and future directions. *Materials*. 2018; 11(4):553.
- [18] Mali S, Singh B. Strength behaviour of cohesive soils reinforced with fibers. *International Journal of Civil Engineering Research*. 2014; 5(4):353-360.
- [19] Putri EE, Rao N, Mannan M. Evaluation of modulus of elasticity and modulus of subgrade reaction of soils using CBR test. *Journal of Civil Engineering Research*. 2012;2(1):34-40.
- [20] Li J, Wang F, Yi F, Wu F, Liu J, Lin Z. Effect of Freeze-Thaw Cycles on Triaxial Strength Property Damage to Cement Improved Aeolian Sand (CIAS). *Materials*. 2019;12(17):2801.
- [21] Ghazavi M, Roustaie M. The influence of freeze-thaw cycles on the unconfined compressive strength of fiber-reinforced clay. *Cold regions science and technology*. 2010; 61(2-3):125-131.

STABILITY ANALYSIS OF A ROCKY SLOPE CONSIDERING EXCAVATION UNLOADING EFFECT

Chuan Zhao^{1,*}, Linlin Jiang², Xiaopeng Li¹ and Simin Luo¹

1. Sichuan Academy of Water Conservancy, Pastoral Circuit No.7 in Qingyang District, Chengdu, China; zhaochuanvip@163.com
2. Renai College, Tianjin University, Tuanbo new city boxue Garden in Tianjin, China

ABSTRACT

The rock mass encountered in actual geotechnical engineering usually undergoes long-term diogenesis and geological tectonic action, and also subjected to repeated actions of loading and unloading repeatedly. This paper aims to study the influence of excavation unloading on the stability of a rocky slope, and the slope excavation process of Jinping Grade I Hydroelectric Station was selected as a case, and the 2D finite element software PLAXIS was used to evaluate the effect for the slope stability of without considering unloading and considering unloading, including stress, safety factor, plastic deformation zone and slip surface of the slope. The results show that the slope excavation unloading has a significant influence on the stress, stability safety factor, plastic deformation zone and slip surface, the stability of slope with considering unloading is far less than without considering unloading significantly. Therefore, the numerical method used to simulate the excavation of rocky slopes should consider the effect of unloading fully to service the engineering design and ensure the safety of engineering construction.

KEY WORDS

Jinping Grade I Hydroelectric Station, Unloading effect, Slope stability, Finite element

INTRODUCTION

Most of the existed rock masses are damaged and undergone various functions and contain a large number of jointed fissures. When the natural rock mass excavated, the unloading process is the further release process of the residual stress, which could cause the internal stress state of the rock mass to change. Reasonable evaluation of the extent and depth of rocky slope excavation unloading damage could guide engineering design and ensure project safety, and this has become a key technical issue in hydropower project construction.

Haqilong proposed the concept of unloading rock mechanics 23 years ago, and the basic theory has been accepted by many scholars (HA Qiuling and LI Jianlin 1996; HA Qiuling 2001). In recent years, many experts and scholars have carried out a lot research on the unloading depth of rock excavation. Such as, Zhao Xiaoyan analyzed the distribution range and variation characteristics of the slope excavation relaxation zone in a centrifugal model test, and proposed using the displacement as the criterion to determine the width of unloading zone (Zhao Xiaoyan et al. 2005). The excavation process of a typical rocky slope was used to study the maximum principal stress increment and the mechanical characteristics and distribution law of the plastic deformation zone, and proposed to adopt the variation of the maximum principal stress component as the criterion for the excavation unloading and relaxation zone(Wang Hao and Liao Xiaopin



2007). Based on the qualitative analysis of the unloading relaxation process and mechanism of rocky slope excavation, Feng Xuemin advised using the ultimate tensile strain of rock mass as the criterion for unloading relaxation (Feng Xuemin et al. 2009). According to the basic idea of statistical rock mechanics, Wu Faquan proposed to determine the depth of unloading damage by the magnitude of unloading strain (Wu Faquan et al. 2009).

At present, with the construction of a large number of infrastructures in the world, involving water conservancy, transportation and civil buildings, such as hydropower slope excavation, tunnel construction and foundation pit excavation, all involved a large number of rock mass excavation, inaccurately assess the extent and size of the unloading of rock masses may result in serious safety incidents. Moreover, the analysis of slope rock excavation using unloading rock mechanics theory is mainly based on qualitative analysis, and there is little research on quantitative analysis of rock mass unloading effects. Therefore, in this paper, the slope excavation of Jinping Grade I Hydroelectric Station in China is taken as a study case to analyze the influence of excavation unloading on the stability of slope rock mass quantitatively.

MATERIALS AND METHODS

A large number of engineering practices and theoretical studies have shown that the unloading action is equivalent to apply a reverse tensile stress in rock mass under initial stress (LI Jianlin 2003; DENG Huafeng et al. 2009). Therefore, in the process of numerical analysis, the stress state before unloading of the rock mass can be regarded as the initial stress state, and the unloading stress can be regarded as a kind of tensile stress on the rock mass. The maximum value is $\sigma_0 + R_i$ ($\sigma_0 + R_i$ is called equivalent tensile strength of rock mass). In this way, the unloading calculation can be divided into two steps: superposition the unloading stress $\Delta\sigma$ and the pre-unloading stress σ , as shown in the Figure1:

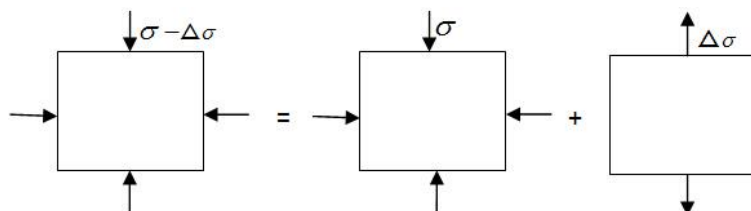


Fig. 1 - Schematic diagram of unloading stress

The specific calculation process is as follows:

Firstly, the stress field σ_0 and the displacement field u_0 of the rock mass under the initial stress; then the stress field $\sigma_{\Delta i}$ and the displacement field $u_{\Delta i}$ of the rock mass under the unloading stress $\Delta\sigma$ are calculated; finally, by superposing the stress fields, the stress field σ_i and the displacement field u_i with the unloading amount $\Delta\sigma$ can be obtained.

$$\sigma_i = \sigma_0 + \sigma_{\Delta i} \quad (1)$$

$$u_i = u_{\Delta i} \quad (2)$$

When calculating the i -th unloading, the stress field $\sigma_{\Delta i}$ of rock mass should be solved first when the i -th unloading $\Delta\sigma_i$; later, the stress field σ_{i-1} and the displacement field u_{i-1} of the $i-1$ th time are superimposed, and the stress field σ_i and the displacement field u_i at the i -th unloading are calculated.

$$\sigma_i = \sigma_{i-1} + \sigma_{\Delta i} \quad (3)$$

$$u_i = u_{i-1} + u_{\Delta i} \quad (4)$$

In the slope engineering, under the action of mass excavation and unloading of the rock mass, the stress relaxation and even tensile stress will occur within the influence range, the mechanical conditions of the structural plane in rock mass will change substantially, the quality of rock mass will deteriorate rapidly, and its mechanical parameters will drop sharply. It is indicated that the unloading rock mass mechanics is sensitive to anisotropic and tensile strength of rock mass R_t . At present, the division of relaxation zone by excavation unloading in rock mass is mainly calculated by the unloading percentage. The formula is:

$$\text{Unloading percentage} = \frac{\Delta\sigma}{\sigma_0 + R_t} \times 100\% \quad (5)$$

Where the $\Delta\sigma$ is the amount of change in stress before and after unloading. σ_0 is the initial stress before excavation. R_t is the tensile strength of rock mass.

Some different unloading areas are divided according to the degree of unloading percentage, and the deformation modulus of rock mass in different influence areas is reduced appropriately. Based on relevant information, the reduction percentage is shown in the table 1(Yi Qinglin et al. 2009; Yi Changping et al. 2005; Li Jianlin and Yuan Daxiang 2001).

Tab. - 1 Reduction percentage of deformation modulus of slope rock unloading

Unloading percentage/%	Percentage decrease in deformation modulus/%
<30	<10
30~50	10~30
50~80	30~50
80~100	50~80

MODEL AND PARAMETERS

We have selected the slope excavation of cable platform of Jinping Grade I Hydroelectric Station in China as the study case. Lamprophyre veins at the cable platform pass obliquely from the back edge of the slope and buried deep, the f_5 、 f_8 faults pass through the leading edge of the lower elevation of the cable platform, the f_{42-9} fault develops deeper inside the f_5 , shown in Figure2.

The study range of finite element model: 400m in the horizontal direction and 350m in the vertical direction, the material model is the Mohr-Coulomb elastoplastic model. The slope of the simulated cable platform is excavated at the slope ratio of 1:0.5, and the excavation is carried out in 5 levels. Each level of excavation is 30m height and set a 3m width road, the total excavation height is 150m. In the calculating process, it is necessary to consider the self-weight stress, but ignore the tectonic stress for the initial stress field. We follow the two-dimensional plane strain assumption, and the influence of groundwater is unconsidered due to the groundwater level is deeply buried. And the finite element mesh model of slope and boundary of the slope is shown in Figure 3.



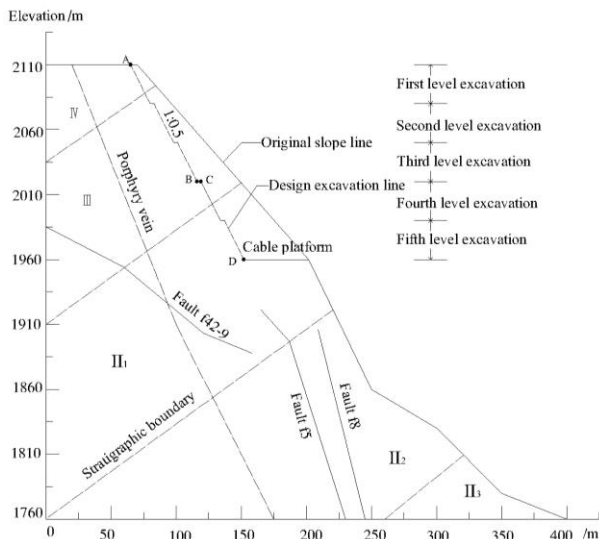
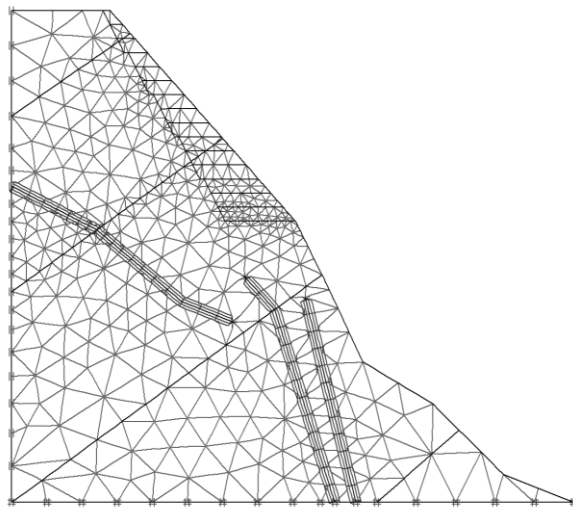


Fig.2 - Sketch diagram of slope excavation for cable crane platform of Jinping I Hydropower Station Fig.3 - Finite element mesh model and boundary of the slope

In the process of finite element calculation, whether the rock mass strength parameters are accurate it has a great influence on the result. Studies have shown that strength of rock mass mechanical parameters in all areas of the unloading rock mass have a decreasing trend, and tend to be stable finally (LI Jianlin 2003). Slope excavation will reduce the rock mass stiffness and strength, such as the elastic modulus, cohesion and internal friction angle and tensile strength decreases, but Poisson's ratio will increase. Based on the unloading rock mass mechanics, the unloading range is obtained by the percentage of unloading amount, and the mechanical parameters of rock mass are obtained by combining and zoning.

The strength parameters of rock mass after excavation are reduced according to the percentage of excavation unloading. In this paper, the reduction is based on the percentage of unloading Table 1. After calculation, the unloading percentage of the rock mass near the excavation is more than 80%, so the original strength parameters of the rock mass are reduced, in this paper, such as the elastic modulus is reduced by about 25%, and other parameters such as cohesion are reduced by about 40%. Thus, the key parameters used are shown in Table 2. Furthermore, the alternative thickness of rock mass material is determined by the increment of shear strain. The thickness of the first three excavation step is 15m, the fourth excavation is 24m and the fifth excavation is 18m. After each excavation, immediately replace the rock mass material caused by this excavation with the reduced rock mass parameters, and conduct stability analysis, then carry out the next excavation, and then replace the rock mass parameters affected by this excavation stage. After each excavation stage, the stability of rock mass is analyzed with smaller strength parameters, so the stability of rock mass in each stage is reduced, and the sliding fracture surface is also distributed along the replacement depth of rock mass material.



Tab. .2 - Mechanical parameters of rock mass

Geological material	Elastic Modulus /GPa	Poisson's ratio	Density /kg/m ³	Cohesion /MPa	Internal friction angle/°	Tensile strength/MPa
Type IV rock mass	2.0	0.33	2700	0.6	30	1.01
Type III rock mass	3.2	0.30	2700	1.0	35	1.15
Type II ₁ rock mass	4.7	0.25	2700	2.2	42	1.3
Type II ₂ rock mass	10.0	0.23	2700	2.8	50	1.3
Type II ₃ rock mass	6.0	0.23	2700	2.0	40	1.3
Fault f ₄₂₋₉	0.6	0.34	2400	0.1	23	0.3
Fault f ₅	0.8	0.35	2400	0.2	23	0.5
Fault f ₈	0.8	0.35	2400	0.2	23	0.5
Unloading rock mass1	1.5	0.40	2300	0.22	15	0.84
Unloading rock mass2	2.4	0.39	2500	0.35	17.5	0.97
Unloading rock mass3	3.53	0.37	2700	0.65	20	1.07

Note: The unloading rock mass parameters only consider three rock masses involved in excavation, and the other rock mass parameters keep unchanged.

This excavated simulation takes the following two calculation terms into account:

Calculation term 1: Without considering of unloading effect. The effect of unloading on rock mass is not considered in the whole calculation process, and the initial mechanical parameters of rock mass are used to calculate.

Calculation term 2: Considering unloading effect. Adopting the analytical method which can reflect the nonlinear characteristics of unloading rock mass, the mechanical parameters of unloading rock mass are dynamically selected according to different excavation levels, so that the numerical calculation is basically consistent with the actual stress of rock mass.

RESULTS AND DISCUSSIONS

Stress analysis

In order to analyze the effect of excavation unloading on stress distribution of rocky slope, the major principal stresses of each monitoring point shown in Figure 2 at different excavation steps and results are listed in Table 3, we stipulate the tensile stress is positive and the compressive stress is negative. It can be found that the major principal stress values of each feature point are negative values under natural conditions, which shows that they are under compression. The stress state of each monitoring point changes continuously along with the excavation of the slope under the two calculation terms.

When the unloading effect unconsidered, the compressive stress at points A and C decreases after excavation of the upper rock mass, which is regard as stress relaxation, and the compressive stress at points B and D increases gradually, which appears as stress strengthening. Since points B and D are located at the foot positions of different steep slopes, they are excavated by the upper right side of the rock mass, resulted in stress releasing and unable to counteract the earth pressure from the left side, so it is under compression.

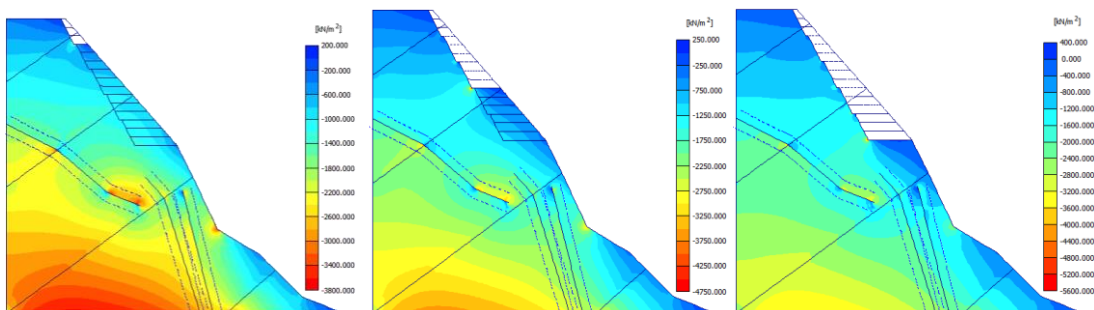


Tab.3 - Main stress of monitoring points in different conditions/MPa

Excavation steps	Calculation terms							
	Regardless of unloading effect				Considering unloading effect			
	A	B	C	D	A	B	C	D
Natural state	-0.26	-2.14	-2.17	-3.01	-0.26	-2.14	-2.17	-3.01
First level	-0.07	-2.03	-2.06	-2.94	-0.03	-2.01	-2.04	-2.91
Second level	-0.07	-1.87	-1.83	-2.78	-0.03	-1.75	-1.72	-2.73
Third level	-0.07	-7.22	-3.09	-2.52	-0.03	-1	-0.98	-2.32
Fourth level	-0.07	-3.9	-0.55	-2.33	-0.04	-0.03	-0.06	-1.88
Fifth level	-0.07	-3.72	-0.52	-7.28	-0.04	0.19	-0.06	-1.46

When considering unloading, the compressive stress of four points is reduced obviously, and appeared relaxation after the excavation completed. The compressive stress value of point D at the foot of slope is particularly different at the two conditions, 7.28 MPa and 1.46 MPa, show all monitoring points appear stress relaxation. In particular, a tensile stress zone will appear near point B, the tensile stress at point B is 0.19 MPa, which could cause adverse effects on the local stability of the slope.

In order to analyze the stress state of rock mass in different excavation stages comprehensively, the average effective stress (σ_m) of rock mass under two calculation terms is shown in Figure 4 and Figure 5 ($\sigma_m = (\sigma_{\max} + \sigma_{\min})/2$), which is the average value of the maximum and minimum stresses on a certain section of a unit, and the maximum principal stress and the minimum principal stress are considered. Figure 4 shows the average effective stress distribution of the rock mass without considering the unloading excavation slope, yet Figure 5 shows the average effective stress distribution of the rock mass with considering the unloading excavation slope. The unit of σ_m is kN/m² (kPa), we also stipulate the tensile stress is positive and the compressive stress is negative.



(a) Excavation 30m (b) Excavation 90m (c) Excavation 150m

Fig. 4 - The average effective stress of rock mass without considering unloading

As shown in Figure 4, when the unloading effect is without considering, the average stress near the excavation changes gradually with the increasing of the excavation depth, the average stress of the lower platform rock mass is small due to the empty surface formed by excavation, indicate that most rock mass are under compression and only a small part under tension, it should be noted that the stress concentration phenomenon exists at the foot of the slope after each step of excavation, which is expressed as compression, and the stress relaxation in the rock mass near



a certain depth of the excavating surface is not obvious, which is inconsistent with reality. It shows that the software can only consider the load release caused by excavation of the upper rock mass, but it cannot evaluate the unloading effect automatically caused by the excavation. Therefore, it is necessary to carry out artificial calculation and evaluate the impact scope of excavation unloading.

As shown in Figure 5 below, when considering the unloading effect, the average stress near the excavation surface changes obviously and the unloading relaxation effect increased gradually with the increasing of the excavation depth, which is manifested that the tensile stress of the rock mass increases within a certain depth of the excavation surface, however, the compressive stress is reduced gradually. In addition, when the excavation depth reaches 90m, the tensile stress of the local rock mass can reach 250kPa, after the excavation of 150m, the tensile stress of the local rock mass can reach 750 kPa and the range of stress relaxation is further expanded, which indicates that the rock mass under tensile near the excavation face is obvious, and could cause a potential local collapse.

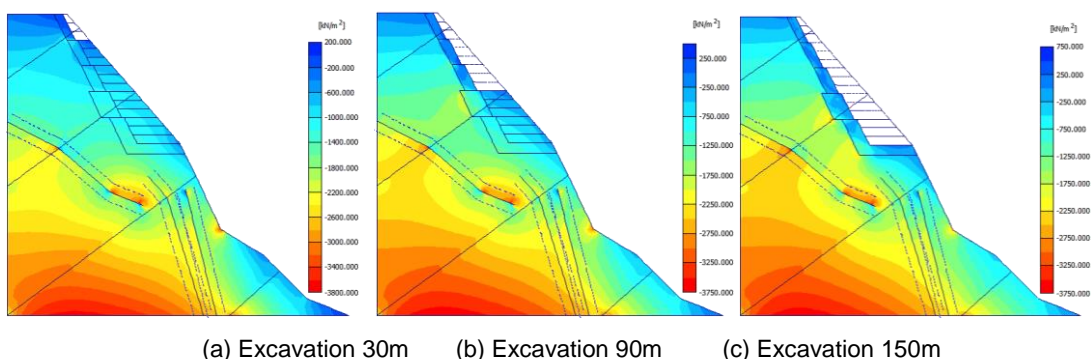


Fig. 5 - The average effective stress of rock mass with considering unloading

The results above illustrate that comparing with the case without considering unloading effect, the numerical simulation analysis of slope excavation with considering unloading effect can evaluate the stress damage of rock mass caused by excavation and determine the influence range of unloading more accurately.

Slope stability safety factors

In addition, the finite element strength reduction method is used to calculate the safety factor of slope stability during the excavation process. The real shear strength of slope rock mass is divided by a reduction factor F to achieve the purpose of strength reduction until the ultimate failure state reached. According to the elastic-plastic finite element calculation results, the critical slip surface of slope is obtained, and the reduction factor F represents the stability safety factor of slope (Zheng Yingren et al. 2002; Li Rongjian et al. 2010; Zhao Chuan and Fu Chenghua 2015). The formulas are as follows:

$$c' = \frac{c}{F} \quad (6)$$

$$\varphi' = \arctan \frac{\tan \varphi}{F} \quad (7)$$

Where c and φ are the real cohesion and internal friction angle of rock mass, c' and φ' are the reduced cohesion and internal friction angle.



Table 4 shows the stability safety factors of excavated slope at different levels under the two calculation terms. The comparative analysis shows that when unloading is without considering, the safety factor changes little along the excavation steps, even tends to increase. It may be inferred that due to the reduction of the slope sliding force and the improvement of the overall stability of the slope after excavation of the upper rock mass. The safety factor is 1.99 after excavation complete, compared with the safety factor of 1.93 under the initial condition, it increases 0.06, which is inconsistent with the phenomenon that the slope stability will reduce due to the actual excavation.

When the unloading action is considered, the rock mass near the slope is affected by excavation, the strength of rock mass decreases obviously, and the safety factor decreases gradually along with the excavation, and reaches the minimum value 1.32 after the fifth excavation. It can be seen that the change law of slope stability safety factor is different under the two conditions, and the slope stability safety factor is smaller when considering unloading than without considering.

According to the results of the Table 4, it is indicated that the results obtained without considering the unloading effect are pretty unreasonable, and it is also very dangerous for the engineering design when ignore the rock mass relaxation effect caused by excavation to use the results directly obtained without considering the unloading effect.

Tab.4 - Safety factors of rocky slope in different excavation levels

Excavation condition	Gravity	Level 1	Level 2	Level 3	Level 4	Level 5
Without considering of unloading effect	1.93	1.93	1.96	1.96	2.00	1.99
Considering unloading effect	1.93	1.77	1.60	1.48	1.40	1.32

Distribution of plastic zone and slip surface

In order to further analyze the plastic deformation zone of the internal rock mass during the excavation of the slope rock mass accurately, Figure 6 and Figure 7 show the plastic deformation zone distribution of the slope in different excavation steps under two conditions (the red point represents the plastic point, and the white point reflects the tensile failure zone). It can be seen from Figure 6 that when the unloading effect unconsidered, the plastic zone distribution range of the slope changes a little along with the increase of the excavation depth, and there is a tendency to decrease. The plastic zones are distributed in the interior of the three faults, mainly appear in fault f_{42-9} , while faults f_5 and f_8 are few relatively. When the excavation reaches 60m and 90m, a few plastic points appear at the foot of the slope formed by excavation. It shows that the rock mass in the structural plane along the strike of the slope is more likely to be destroyed. Because the fault f_{42-9} terminates in a certain depth of the slope and does not penetrate into the slope surface, the overall slope can remain stable at this time, and the safety factor is 1.99.

As shown in Figure 7, when the unloading effect is considered, the plastic zone distribution range of the slope will increase greatly with the increase of the excavation depth, which is mainly reflected in the unloading rock mass surface formed by excavation. In addition, after excavation depth of 150 m, the red plastic zone almost penetrates the unloading rock mass, which has a great impact on the overall stability of the slope, and the plastic failure is most obvious at the foot of excavated slope. It is well consistent with the analysis results of the stability safety factor.

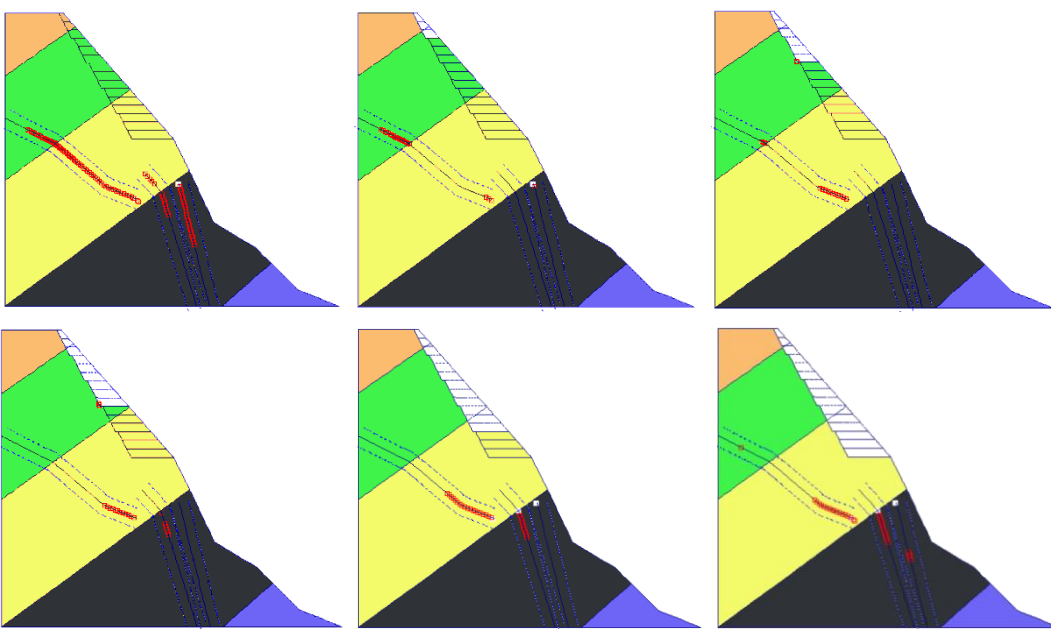


Fig. 6 - The plastic points distribution of rock mass without considering unloading

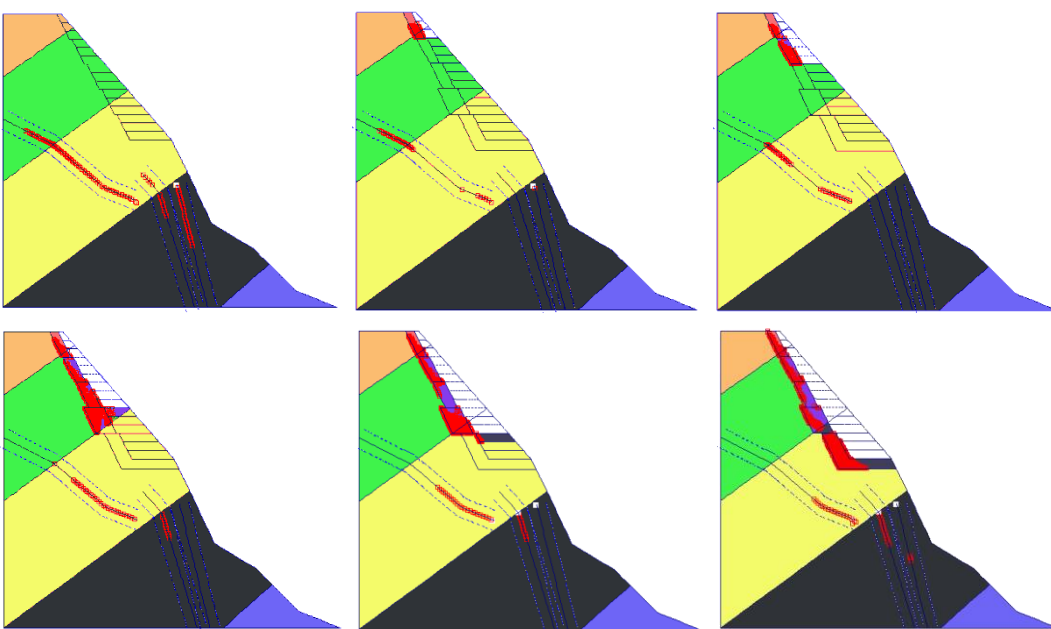


Fig. 7 - The plastic points distribution of rock mass with considering unloading

The above analysis of the plastic zone shows that whether the unloading effect is considered it has a great influence on the results of the plastic failure range of rock mass. When unloading is not considered, the plastic point of slope only exists in the fault, but when unloading effect is considered, the plastic point mainly distributes in the rock mass within a certain depth from the excavated slope surface, and forms a large area of plastic point concentration at the foot of the slope.

When the stability of the slope is solved by the finite element strength reduction method, the slope will gradually slide along the critical slip surface with the increase of the reduction factor. In order to analyze the potential slip surface of the slope under different conditions and different



excavation heights, the position where the slope may be damaged under the limit equilibrium state is obtained. Figure 8 shows the results without considering the unloading, and Figure 9 indicates results considering unloading effect, and the colour gradually changes to red, indicating that the sliding occurred here is very obvious.

As shown in Figure 8, all the critical slip surface of the slope is deep along the fault f_{42-9} . It is indicated that in the process of excavation, if the unloading effect is not considered, when the slope rock mass reaches the ultimate failure, the position of the slip surface obtained in each excavation stage is the same, which is not consistent with the actual situation.

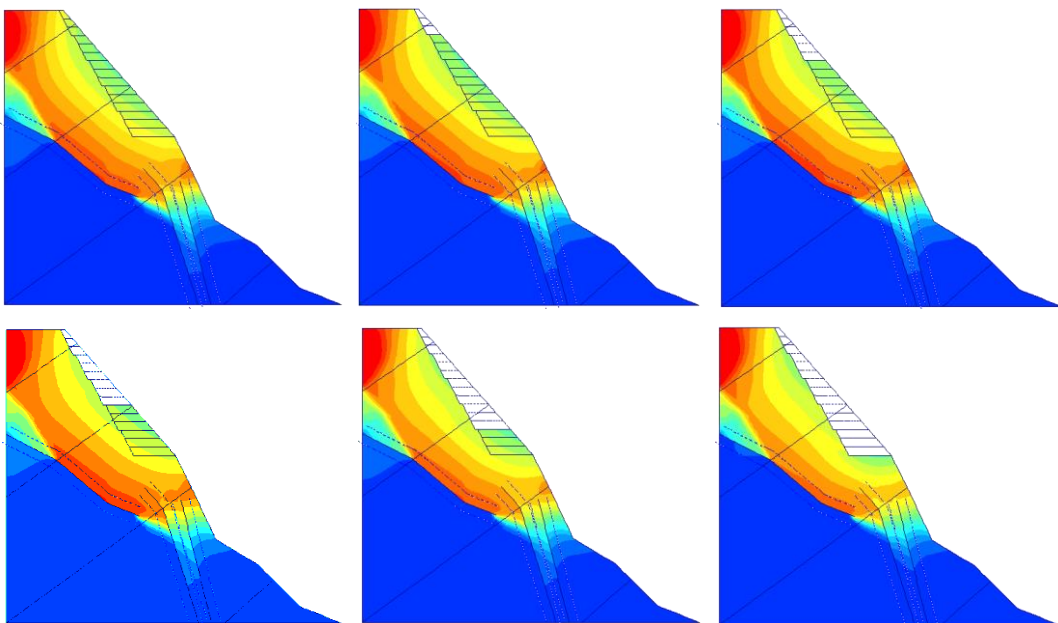


Fig.8 - The slip surface of slope without considering unloading

In order to make a comparative analysis with the above results, the critical slip surfaces with different excavation heights when considering unloading effect are given in Figure 9. The result shows that with the increase of excavation depth, the position of critical slip surface changes gradually, which is very different from that shown in Figure 8 above. Considering the unloading effect, the slip surface is distributed within a certain depth range to form an arc slip shape, and extend downward gradually as the excavation depth increases, the shear foot is formed from the excavation until the excavation is completed. At this time, the volume of potential landslide body is much smaller than that when unloading is not considered, the safety factor of the slope is also smaller. It shows that if the unloading effect of rock mass excavation is reasonably considered, the scope of rock mass damage caused by excavation can be obtained, and the location of possible slope sliding can be determined, which can provide reference for the corresponding reinforcement measures after slope excavation, such as the length and depth of bolt reinforcement in bolting and concreting support, and the size setting of the pre-stress applied.

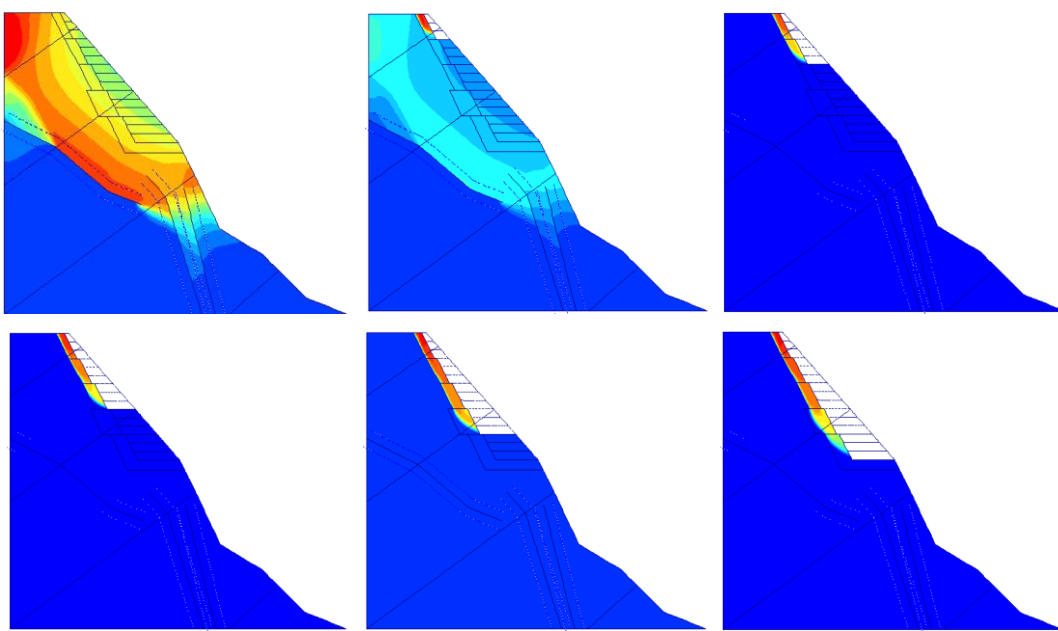


Fig.9 - The slip surface of slope with considering unloading

CONCLUSIONS

In this paper, the excavation process of the high-steep slope of the cable platform of Jinping Grade I Hydroelectric Station is simulated and analyzed by PLAXIS. It is found that whether the unloading effect is considered it has a great influence on the stability analysis along with the slope excavation. When the unloading effect during rock mass excavation is considered, the stress relaxation of slope excavation is more obvious than when the unloading effect is not considered.

Tensile stress will occur in some areas, which is mainly reflected in the internal rock mass stress distribution affected by excavation. With the gradual excavation of the slope, the safety factor of stability does not change much when unloading unconsidered, and ultimately is 1.99. However, the safety factor of the slope decreases gradually with the increasing of excavation depth when unloading effect considered, the safety factor is 1.32 finally after excavation complete. The distribution of plastic zone and critical slip surface is different under the two conditions. When unloading is not considered, the relationship between the scope of slope plastic zone and excavation depth is very small, and mainly concentrated in the interior of three faults, when unloading is considered, the plastic failure zone mainly concentrates in the interior of rock mass near the excavation surface of slope.

There are different critical slip surfaces in the two conditions, and the slope stability is worse when unloading is considered than unconsidered. If the unloading effect is not taken into account, the critical slip surfaces of the slope are the same location along fault f_{42-9} in each excavation stage. However, when the unloading effect considered, the location of the critical slip surface changes gradually with the increasing of the excavation depth, and it is distributed along a certain depth range of the rock mass excavation unloading affected area, formed an arc slip shape, and extending downward gradually.

Therefore, it is suggested strongly that the deterioration of rock mass caused by excavation should be fully considered for numerical simulation in the future, and the whole excavation unloading process need to be simulated reasonably, so as to provide more accurate reference for engineering design and construction.

ACKNOWLEDGMENTS

The research is mainly supported by the basic research funding project of Si Chuan province. The authors thank Prof. Chenghua Fu for her help to improve the paper. Her kind efforts are gratefully acknowledged. The authors also thank all anonymous reviewers for reviewing the manuscripts.

CONFLICTS OF INTEREST

The authors declare that they have no conflicts of interest.

REFERENCES

- [1] HA Qiuling, LI Jianlin (1996) Study on macroscopic mechanical parameters of unloading rock mass on rock slope. Beijing: China Architecture & Building Press.
- [2] HA Qiuling (2001) Simulation analysis for rock mass engineering and rock mass mechanics-The study on anisotropic excavation unloading rock mass mechanics. Soil and Rock Engineering Journal 23(6): 664-668.
- [3] ZHAO Xiaoyan, HU Houtian, PANG Liexin (2005) Study on unloading effect and width of unloading zones in excavating of soil-like material slopes. Chinese Journal of Rock Mechanics and Engineering 24(4): 708-712.
- [4] WANG Hao, LIAO Xiaopin (2007) Research on the mechanical character of relaxing zone of slopes due to excavation. The Chinese Journal of Geological Hazard and Control 18(sup): 5-9.
- [5] FENG Xuemin, CHEN Shenghong, LI Wengang (2009) Research on unloading relaxation criterion of high rocky slope excavation and its engineering application. Rock and Soil Mechanics 30(sup2): 452-456.
- [6] Wu Faquan, Liu Jianyou, Liu Tong (2009) A method for assessment of excavation damaged zone (EDZ) of a rock mass and its application to a dam foundation case. Engineering Geology 104: 254-262.
- [7] LI Jianlin (2003) Unloading rock mass mechanics. Beijing: China Water & Power Press.
- [8] DENG Huafeng, LI Jianlin, YI Qinglin (2009) Research on unloading deformation of soft high slope. Rock and Soil Mechanics 30(6): 1731-1734.
- [9] YI Qinglin, DENG Huafeng, WANG Lehua (2009) Study on unloading deformation of one highway slope. Chinese Journal of Underground Space and Engineering 5(1): 139-143.
- [10] YI Changping, LU Wenbo, XU Hongtao (2005) Study on effects of dynamic unloading on initial. Chinese Journal of Rock Mechanics and Engineering 24(sup1): 4750-4753.
- [11] LI Jianlin, YUAN Daxiang (2001) Basic method for analyzing unloading of rock mass. Journal of China Three Gorges University (Natural Sciences) 23(1):1-6.
- [12] ZHENG Yingren, ZHAO Shangyi, ZHANG Luyu (2002) Slope stability analysis by strength reduction FEM. Engineering Science 4(10): 57-62.
- [13] LI Rongjian, ZHENG Wen, SHAO Shengjun (2010) Comparison analyses on stability of unsaturated soil slopes by strength reduction FEM and slice method. Journal of Northwest A &F University (Natural Science Edition) 38(9): 207-214.
- [14] ZHAO Chuan, FU Chenghua (2015) Stability analysis of slope in a hydropower station with local strength reduction method. Pearl River 18(3): 66-69.

CHANGE IN RESILIENT MODULUS OF BASE LAYERS IN ASPHALT PAVEMENT STRUCTURES OVER TEXAS

Nitish Raj Bastola and Mena Souliman

University of Texas at Tyler, Department of Civil Engineering, Tyler, Texas, USA;
nbastola@patriots.uttyler.edu, msouliman@uttyler.edu

ABSTRACT

The properties of materials change over time and the same case happens for the HMA pavement. The various components of HMA pavement such as surface, base, sub-base, and sub-grade have time related functions. In particular, the base layer which is the immediate layer below the surface, comprising of various materials such as crush aggregates and HMA also have a time related function. Among the numerous properties of the base layers which are dependent with time is its resilient modulus. Therefore, this paper correlates the effect of the change in resilient modulus with time including the various varying conditions such as rutting, thickness of base layer, precipitation, traffic, temperature, IRI index, wheel path length cracked, cracking percentage, crack length, liquid limit, plastic limit, optimum moisture content, and % fine passing below 200 sieve. Each individual factor has different effects over the resilient modulus of the base layer, but their effects are more severe when they act at once in a pavement structure.

KEYWORDS

HMA pavement, Base layer, Resilient modulus

INTRODUCTION

The construction of flexible pavement involves numerous layers such as surface layer, base layer, and sub base layer over the subgrade. The layer below the surface is known as base layer and is directly responsible for the strength of the pavement structure and as well as, in load spreading and stress reduction [1]. At various instances, base layer has been proven to be the most effective layer for the drainage because of the well graded aggregates which act as a flow-path for water. The properties of base layers have a great importance when talking about the performance of pavement. The base layer comprises of aggregates and if the base layer is purely made of aggregate it is known as unbounded base layer but if the aggregates are treated with some kind of treatment agent it will be referred as bounded base. One of the important properties of the base layer, which is directly related to its strength, is its resilient modulus. The property which is directly related to the stiffness of the flexible pavement is its resilient modulus and requires a lot of analysis. Various researches have been performed for knowing the resilient modulus of the base layer in a flexible pavement structure. Those studies were related to the various independent factors affecting the performance of the base layer in a pavement structure, but numerous factors act on the pavement structure which will decrease the resilient modulus of the pavement and in long term the strength of the pavement. Some of the important factors which play a great role in the changing resilient modulus with time are as rutting, thickness of base layer, precipitation, traffic, temperature, IRI index, wheel path length cracked, cracking percentage, crack length, liquid limit, plastic limit, optimum moisture content, and % fine passing below 200 sieves. These factors are analysed independently as well as in the combination for knowing the resilient modulus of the base



layer in a pavement structure and in addition a comparative study of the change in the resilient modulus of base layer with time is presented. These factors may not have direct role with regard to the resilient modulus, but also a simplified model considering the effect of these factors is necessary for understanding the performance of base layer with respect to resilient modulus.

LITERATURE REVIEW

A flexible pavement structure is quite different from other types of monolithic engineering structures and this is due to the presence of a multi-layer system whose properties change when subjected to various external factors over the course of time [1]. These properties are more clearly described when study is done over the material from which it is made. One among those multiple properties is resilient modulus, which is mostly pronounced as modulus. Traffic and environment conditions are more responsible for the complex behaviour of the hot-mix asphalt pavement. Along with traffic and environment, there are numerous factors which play a vital role in the mechanistic design of asphalt pavement.

The resilient modulus also differs from layer to layer, so the modulus at the top of the surface will not be the same in the base and subgrade level. Asphalt surface being the top most layer, its properties can be found easily, but for underlying base layer the same case does not occur. The resilient modulus of the base layer at any time is dependent on the multiple factors including the traffic loading itself.

For this complex nature of pavement, simple method of designs become ineffective, therefore, numerous empirical designs were developed and the observation of pavement performance recorded over various point acts like a strong foundation on the development of this method [2]. The database is provided by various government agencies and one of the noted databases for US and Canada is LTPP (Long Term Pavement Performance) which has a vast database on the hundreds of factor related to pavement [3].

Various researches have been performed for the behaviour of resilient modulus of the base layer in the pavement. All of these researches are focused on the pavement material characteristics at various levels of pavement. Vukobratovic et al. [1] had conducted a research focusing over the influence of material characteristics on pavement design. The performance of pavement had changed a lot when the materials' characteristics were changed. The primary focus over the research was towards the influences of humidity and temperature on the pavement. Moduli were determined at different moistures and temperature level as material properties were variable on the layer system of pavement. The correct choice of the resilient modulus is the most important thing as it is also the representation of layers of pavement structure over time. Knowing the proper material characterization and development of empirical models can also be very much effective on the cost reduction by decreasing the thickness.

Similarly, Ji et al. [4] conducted a study to evaluate the resilient modulus of subgrade and base materials in Indiana and its implementation in Mechanistic Empirical Pavement Design Guide (MEPDG) as MEPDG itself needs the resilient modulus for the characterization of the layer and their structural design. Resilient Modulus values were correlated with the index of soil and other numerous properties like coefficient followed over layer and California Bearing Ratio, etc. Various procedures and their influences can be very much important for the evaluation of resilient modulus.

Wang et al. [5] conducted a study to know the relationship of resilient modulus with respect to fatigue cracking as well as rutting potential and these factors must be included while judging the mechanical properties of the pavement.

Resilient modulus as presented by Mousa et al. [6] is based on mechanistic pavement design methods that utilized various factors affecting the resilient modulus of the base and sub-



grade layer. The factors related to soil index properties, stress state, and moisture content and matric suctions were presented in the study. The study demonstrated that the resilient modulus was greatly influenced by the level of applied stresses and amount of moisture content in the material.

Similarly, the study on the effect on the various factors affecting the resilient modulus is not only limited to unbound materials. The research by Li et al. [7] explained the effect of materials and temperatures on the resilient modulus of asphalt treated base layer.

The various studies presented above demonstrated that the resilient modulus in a base layer is affected by numerous factors. Many researchers have provided various numerical models focusing over some factors but a descriptive analysis considering the multiple effects are not presented. Thus, this paper aims on bridging the base layers taking into the factors with actual conditions of the pavement before its construction and after its construction under some time frames.

OBJECTIVE AND SCOPE

The primary objective of this study is to know the influence of various factors in resilient modulus of the base layer in asphalt pavement and determine the empirical model to calculate resilient modulus with respect to these factors. Similarly, as a secondary objective, various sections of the pavement are analysed to know the resilient modulus of those layers with respect to time.

DATA COLLECTION

As we know, hot mixed asphalt pavements are very much susceptible to various environments and mechanical changes over time, hence, the research focuses over the change in the most important property – resilient modulus - of base layer is needed. There also needs to be a look into various conditions such as rutting, thickness of base layer, precipitation, traffic, temperature, IRI index, wheel path length cracked, cracking percentage, crack length, liquid limit, plastic limit, optimum moisture content and % fine passing below 200 sieves. The data with regards to these parameters was collected from Long Term Pavement Performance Database (LTPP) [3]. LTPP has a vast source of the database from the pavement section of United States and Canada. Among the various sections, numerous pavement sections from Texas were taken as the prime purpose of the research. The data from twenty sections were taken along the entirety of Texas. The Figure 1 below shows the sections taken for the analysis.

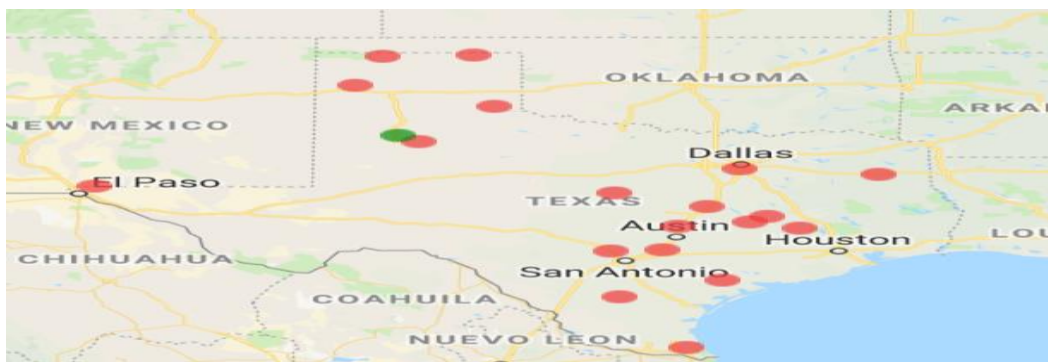


Fig. 1 - Location of sections under study

With the data from these sections, the relation of these numerous parameters was performed using scatter plots, histograms, and regression analysis. These analyses are described clearly on the preceding contents of this paper.

DATA ANALYSIS

With the collected data, basically three forms of analysis were done. They are described below.

Effect of time on the resilient modulus of the base layer of pavement

The resilient modulus of the base layer of pavement structure is found to have a time dependent property. The resilient modulus decreases with respect to time. All of the section possessed the properties of resilient modulus degradation until and unless any kind of reconstruction and rehabilitation activities were performed on the pavement surface. The Figure 2 below shows 20 sections observed over various times with respect to the resilient modulus and year of data taken.

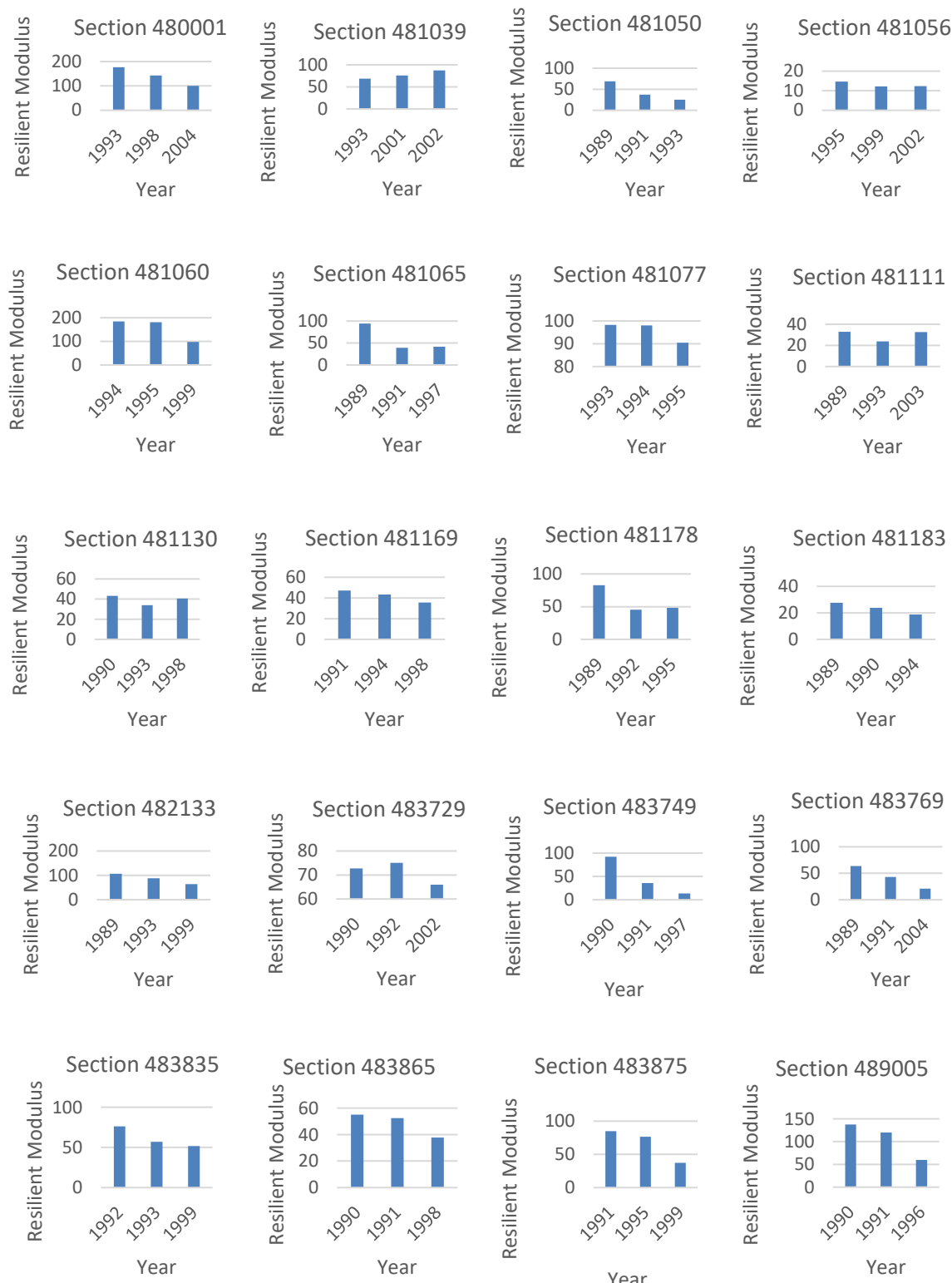


Fig. 2 - Change in resilient modulus (expressed as Ksi) with time

Effect of singular factor on the resilient modulus of base layer of pavement

In this study, thirteen factors were considered in the analysis of the base layer of the pavement structure. These factors are encountered separately to identify the effect on the pavement. Some factors had shown a great influence on the resilient modulus of base layer but some factors impart a lesser effect.

Traffic loading represented as Annual Average Daily Traffic (AADT) has the most significant effect on the resilient modulus of the base layer of the pavement. The value of $R^2 = 0.20$ itself suggests the effect of the AADT on the base layer. Temperature being a surface phenomenon on the HMA pavement has a significant effect on the resilient modulus of the pavement. IRI or International Roughness Index is another factor responsible for the change in the resilient modulus of the pavement. IRI also has a great effect on the resilient modulus of base layer with the value of $R^2 = 0.14$. Rutting, referred as surface depression on the wheel path, has a significant effect on entire HMA pavement but in the resilient modulus of the base layer it has a lesser effect. HMA pavement is mostly characterized by its thickness, but thickness of base layer and precipitation had a small effect in the resilient modulus of the base layer of pavement. Similarly, various cracks measured in the pavement showed that the crack in the surface layer does not give any significant effect on base layers, although cracking percentage showed a better relation with resilient modulus than the wheel path length cracked. Various constructions related parameters are also utilized in this study and their relation with resilient modulus of base layer was identified. Liquid limit (LL), plastic limit (PL), optimum moisture content (OMC), and percentage passing below 200 mm sieve type aggregate are the detrimental properties needed to be considered during the period of construction, but having the low R^2 value suggests that their effects are relatively less when resilient modulus of base layer is considered.

Figure 3 presents the effects of these factors when related to the resilient modulus of the base layer in the pavement structure.

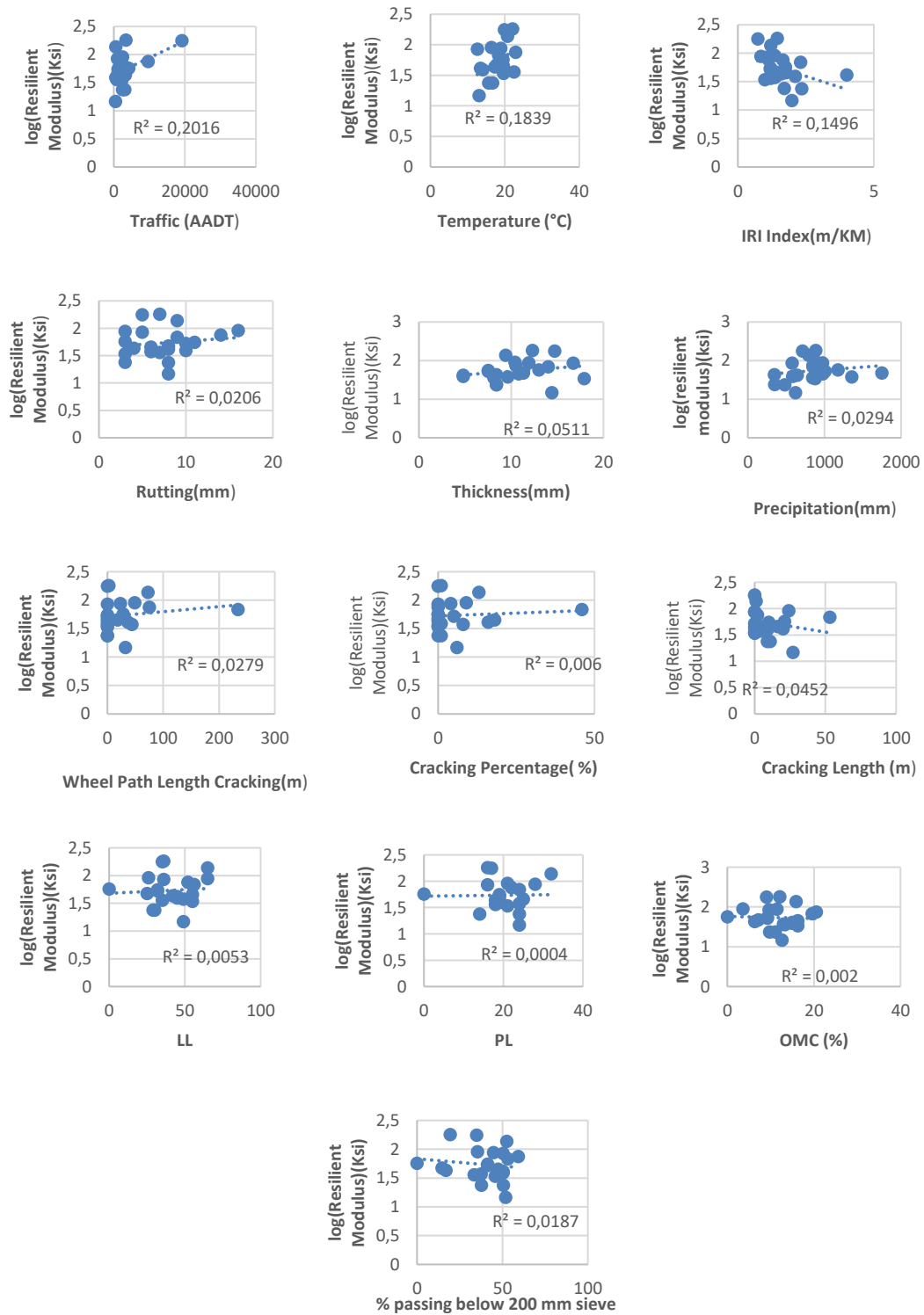


Fig. 3 - Effects of various factors in resilient modulus

Effect of multiple factors on the resilient modulus of base layer of pavement

The study of effect of individual factors on the pavement was performed before, but the pavement is exposed to diverse conditions. For example, precipitation, wheel loading, and cracking of the pavement can occur at the same instant. Structures exposed to this kind of multiple factors do not rely solely on one factor. In this section of the analyses, all the factors are considered so that the actual condition of the pavement is simulated. Multiple regression analysis was applied as a tool to analyse this data. The following Table 1 shows the regression statistics obtained from the multiple regression analyses using excel.

Tab. 1 - Statistics result from multiple regression analysis

	Coefficients	Standard Error	t Stat	P-value
Intercept	1.891E+00	1.04658	1.807	0.108
Rutting	4.354E-02	0.02389	1.823	0.106
Thickness	2.051E-02	0.02767	0.741	0.480
Precipitation	-1.513E-04	0.00023	0.663	0.526
Traffic	2.008E-05	0.00002	1.268	0.240
Temperature	-4.531E-04	0.03569	0.013	0.990
IRI index	-2.922E-02	0.17719	0.165	0.873
WP length cracked	8.748E-04	0.00276	0.317	0.759
Cracking %	2.788E-02	0.01479	1.885	0.096
Crack Length	-2.412E-02	0.01105	2.183	0.061
LL	6.681E-03	0.01046	0.639	0.541
PL	-1.666E-02	0.02144	0.777	0.459
OMC	-2.220E-02	0.02942	0.754	0.472
Passing no. below 200	-5.487E-03	0.00875	0.627	0.548

DEVELOPMENT OF PREDICTION MODEL

With the above multiple regression analyses and statistics value, a model is developed to incorporate all the factors affecting the resilient modulus of the base layer in the hot mixed asphalt pavement structure. The equation is valid for the correlation value as high as 0.70. The equation (A) is the predicted model and the Figure 4 is the regression analysis on the predicted versus measure value.

Log (Resilient Modulus) = 1.891 + 4.354E - 02 * Ruting + 2.051E - 02 * thickness - 1.513E - 04 * Precipitation + 2.008E - 05 * Traffic - 4.531E - 04 * Temperature - 2.922E - 02 * IRI + 8.748E - 04 * WP lengthcracked + 2.788E - 02 * Cracking% - 2.412E - 02 * CrackLength + 6.681E - 03 * LL - 1.666E - 02 * PL - 2.220E - 02 * OMC - 5.487E - 03 * Passing no. below 200

-----(A)



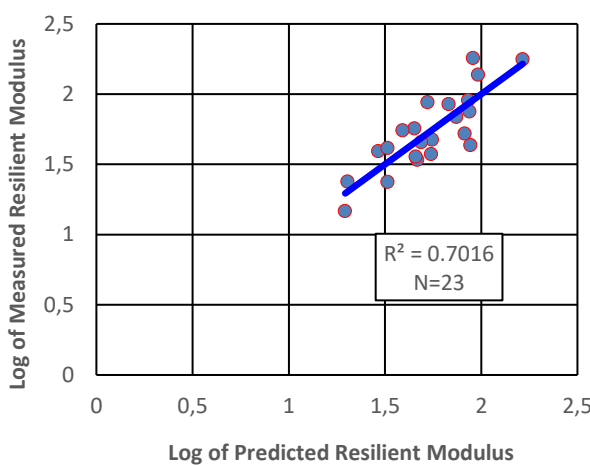


Fig. 4 - Measured VS predicted log of resilient modulus

RESULTS AND CONCLUSION

It is found that HMA pavement is influenced by multiple factors and for actually predicting the resilient modulus of the base layer in HMA pavement, multiple factors are needed to be taken into account. A real pavement structure is acted by numerous distresses, loading, and environment conditions at time and judging a pavement structure with only one factor can be a wrong practice to be followed. The independent factors presented in this study influence the performance of pavement structure. Similarly, a pavement must be rehabilitated and maintained time and again because this will increase overall performance of the pavement, thus, increasing the resilient modulus of the base layer of pavement. Therefore, the model developed in this study utilized all thirteen different factors to predict the resilient modulus of the base layer at that instant, and the model having a coefficient of determination equals to the value of 70 % indicates a good prediction capacity.

RECOMMENDATIONS

The data presented in this study resembles climatic conditions in the state of Texas, and the model also features the conditions resembling those climatic conditions. Therefore, the expansion of the study to the diverse area along with the field verification can be very beneficial.

REFERENCES

- [1] N. Vukobratovic, I. Barisic and S. Dimter , "ANALYSES OF THE INFLUENCE OF MATERIAL CHARACTERISTICS ON PAVEMENT DESIGN," 2017.
- [2] M. Srzen, D. Tibljas, M. Cuculic and M. Vrklijan, "Mechanistic Pavement Design," Via Vita, Croatia, 2011.
- [3] "LTTP Infopave Data Selection and Download," US Department of Transportation, Federal Highway Administration, [Online]. Available: <https://infopave.fhwa.dot.gov>. [Accessed April 2019].
- [4] R. Ji , N. Siddiki , T. Nantung and D. Kim, "Evaluation of Resilient Modulus of Subgrade and Base Materials in Indiana and Its Implementation in MEPDG," *The Scientific World Journal*, 2014.
- [5] H. Wang and M. Li, "Evaluation of Flexible Pavement Performance Due to Variation in Aggregate Base Layer Properties," 2015.

- [6] R. Mousa, A. Gabr, M. G. Arab, A. Azam and S. El-Badaway, "Resilient modulus for unbound granular materials and subgrade soils in Egypt," in *MATEC Web of Conferences* (120), 2017.
- [7] P. Li, L. Juanyau and S. Saboundjian, "Materials and Temperature Effects on the Resilient Response of Asphalt-Treated Alaskan Base Course Materials," *Journals of Materials in Civil Engineering*, vol. 23, no. 2, pp. 161-168, 2011.
- [8] Y. Huang, "Pavement Analysis and Design," vol. 2, 2004.
- [9] R. Terrel and I. Awad , "Resilient Behaviour of Ashpalt Treated Base Course Materials," Washington State Highway Commission, Washington, 1972.

EFFECT OF VEHICLE QUALITY AND SPEED ON THE IMPACT CHARACTERISTICS OF AN OVERPASS BRIDGE PIER

Shijie Wang^{1,2}, Quansheng Sun^{1*} and Jianxi Yang¹

1. Department of Civil Engineering, Northeast Forestry University, Harbin 15004, China; hrbsqs@126.com
2. College of Civil and Architectural Engineering, Heilongjiang Institute of Technology, Harbin 150050, China

ABSTRACT

To study the impact of the mechanical characteristics of heavy trucks on piers under different masses and speeds, a new equivalent simplified model of heavy trucks is proposed in this paper. The reliability of the calculation model is verified by studying the pier of the G1011 Ha-Tong high-speed K302+095 separated overpass, which was subjected to impact by a heavy truck. A finite element model of a heavy truck and a pier is established using the finite element software ABAQUS, and the influence of heavy truck load and impact speed on the impact force and pier stress is analysed. Results show that the peak of impact force increases with the increase in the mass and impact speed of heavy trucks. The high-stress area of the pier is concentrated in the root and the impact position, and an inclined through-crack is formed at 45° with the pier axis. The results also reveal the influence law of the quality of heavy trucks and impact speed on the impact force and stress of the pier and provide a new theoretical basis for the anti-collision design of piers and the limitation of current specifications on the high-speed impact of heavy trucks on piers.

KEYWORDS

Heavy truck load, Impact speed, Pier impact, Finite element analysis, Impact force

INTRODUCTION

Accidents caused by vehicle impacts on piers have increased with the increase in the number of overpass bridges and motor vehicle carrying capacity, thereby not only causing loss of life and property but also threatening the safe operation of bridges. Highway accidents are likely to result in pier collapse due to the large number of heavy vehicles and high speed. Thus, relevant departments, engineers and scholars have conducted research on pier anti-collision of vehicles [1].

At present, local and foreign research on vehicle-pier impact mainly focuses on the impact force and dynamic response of piers, and research methods include experimental research and numerical simulation [2-8]. Popp was the first to test truck impact on a column structure, and a truck impact test was conducted on concrete and steel columns [9]. A simplified vehicle-pier model is typically used in experimental studies because of the high cost of impact test of large vehicles. Zhu Yadi and Lu Wenliang conducted a model impact test of a truck and a pier and found that impact force has a linear relationship with truck speed; in addition, the impact force is related to the diameter and slenderness-to-length ratio of the pier [10]. With the development of a large general finite element software and the progress of engineering simulation technology, numerical simulation has become an important research method for studying vehicle-bridge collisions. El-tawil et al. first established the fine finite element model to perform a numerical simulation analysis of car impact on bridge piers, and research shows that under some special conditions, the



provisions of the 1998 U.S. Bridge Design Code have unsafe characteristics [11]. Agrawal et al. analysed the impact behaviour between a truck and a reinforced concrete pier by means of numerical simulation and proposed a design method based on impact resistance [12]. Lu Wenliang used LS-DYNA to establish the finite element model of vehicle-pier-column collision, and analysed the dynamic response of the pier when the vehicle hit the pier without velocity. The calculation results show that the dynamic response of the pier column is basically proportional to the speed of the vehicle [13]. Xu Linfeng used ANSYS/LS-DYNA finite element analysis software to study the influence of vehicle impact speed and mass on the impact force time history curve [14]. On the basis of the experiment, Liu Shan established the finite element model of the real car impact on the pier with LS-DYNA, and calculated and analysed the impact force and the damage of the concrete pier. The results show that the impact force is proportional to the mass and speed of the vehicle, after the frame pier and the single column pier are hit by the vehicle, the damage position is mainly the root area of the pier (bending failure) and the impact point area (local failure) [15].

The collision of a truck into a bridge pier will cause damage to the bridge, reduce its bearing capacity and seismic resistance and even cause the bridge to collapse. At present, the relevant research is still in its infancy, and no reliable simplified analysis method is available for heavy vehicles impacting bridge piers. Existing specifications can solve the impact problem of small mass and low speed, but they are unsuitable for high-speed impact of heavy vehicles on bridge piers. The influencing factors and related mechanisms of heavy vehicles impacting bridge piers have not been fully studied.

Considering the high-test cost and the mature development of numerical simulation technology, this paper adopts the general finite element software ABAQUS to analyse the influencing factors of heavy trucks impacting bridge piers. On the basis of the Ha-Tong high-speed accident, a new equivalent model of heavy truck is proposed, and a finite element model of a heavy truck impacting a rectangular reinforced concrete pier is established. The reliability of the numerical simulation results is verified. On the basis of the impact course of the truck, the damage characteristics of the pier hit by heavy vehicles are analysed. The effects of the quality and impact speed of the truck on the impact force of the pier and the von Mises stress are revealed. This paper provides a new theoretical basis for the anti-collision design of piers and the limitation of current specifications in the high-speed impact of heavy trucks on piers.

ESTABLISHMENT OF THE FINITE ELEMENT MODEL

Establishment of the finite element model of the pier

Rectangular-reinforced concrete section is adopted for the pier of the G1011 Ha-Tong high-speed K302+095 separated overpass, which is 1200 mm long, 200 mm wide and 4850 mm high. The diameter of the main reinforcement is 25 mm, the diameter of the stirrup is 8 mm and the strength grade of the concrete is C25.

ABAQUS was used to establish the numerical analysis model. The concrete element C3D8R was used for the pier, and the T3D2 truss element was used for the pier rebar. The concrete plastic damage model is adopted, the paper assumes that the initial strain of undamaged concrete is 0 and its material parameters are shown in Table 1. The rebar adopts the ideal elastic-plastic constitutive model, and its material parameters are shown in Table 2. According to the real bridge collision accident case, when the pier is hit by a car, the lateral displacement of the top of the pier causes the support to fall off, whereas the foundation does not change. Thus, the finite element model boundary condition of the pier features consolidation at the bottom of the foundation and a free top area.

Tab. 1 - C25 plastic constitutive parameters of concrete

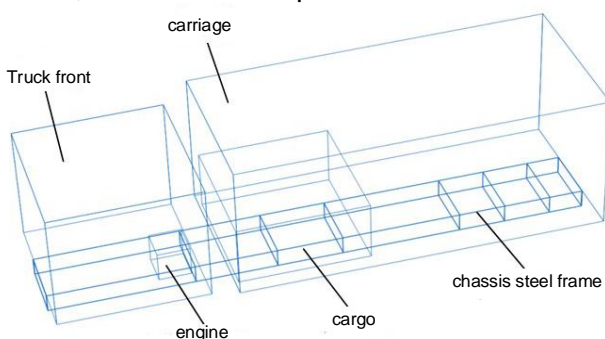
Tensile plasticity									
Stress (MPa)	1.780	1.457	1.113	0.800	0.536	0.359	0.161	0.073	0.040
Strain ($\times 10^{-2}$)	0.00	0.01	0.03	0.05	0.08	0.10	0.20	0.30	0.50
Compression plasticity									
Stress (MPa)	24.019	29.208	31.709	32.358	31.768	30.379	21.907	14.897	2.953
Strain ($\times 10^{-2}$)	0.00	0.04	0.08	0.12	0.16	0.20	0.36	0.50	1.00

Tab. 2 - Constitutive parameters of steel bars

Elastic modulus E (Pa)	Poisson's ratio μ	Yield strength σ_y (Pa)	Density (kg/m ³)
1.9×10^{11}	0.3	2.1×10^8	7800

Establishment of the finite element model of the heavy truck

With a heavy truck as the research object, combined with the advantages of the fine finite element model and the simplified finite element model, this paper, considering the impact effect of a heavy vehicle, proposes the equivalent truck finite element model to mainly simulate the five components that have the greatest influence on pier impact. These five components are the front, carriage, chassis steel frame, engine and cargo; other components of the truck are ignored. The equivalent model of heavy trucks is shown in Figure 1. The S4R shell unit is used for the locomotive and carriage, and the C3D8R solid unit is used for the engine, truck chassis and cargo. Based on heavy vehicle structure, the size of the engine block is determined to be 300 mm×500 mm×700 mm. the size of the truck chassis is determined to be 300 mm×230mm×2500 mm. Q345 steel is used for vehicle models, whose material parameters are shown in Table 3.


Fig. 1 - Equivalent model of heavy truck
Tab. 3 - Constitutive parameters of the Q345 steel

Elastic modulus E (Pa)	Poisson's ratio μ	Yield strength σ_y (Pa)	Density (kg/m ³)
2.06×10^{11}	0.3	3.45×10^8	7800

This section should describe in detail the study material, procedures and methods used.



VERIFICATION OF THE FINITE ELEMENT MODEL

Figure 2 shows the damage characteristics of the pier of the G1011 Ha-Tong high-speed K302+095 separated overpass after a 36t heavy truck collided into the pier. The concrete on the pier's failure surface fell down, showing a gap of about 10 cm. The exposed steel bar underwent plastic deformation. The failure surface between the impact point and the pier base presented a diagonal failure form of about 45° with the pier axis. To verify the reliability of the finite element model, Figure 3 shows a von Mises stress cloud diagram of the impact of an equivalent truck model on bridge piers with $m = 36t$ and $v = 80 \text{ km/h}$. Figure 3 shows the position of the impact and the maximum stress of the pier on the base of the pier. The area with large stress is mainly distributed between the base and the impact position, and the failure surface beyond the tensile strength of concrete is about 45° from the pier axis. A comparison between the numerical simulation results and actual collision accidents shows that the damage characteristics of the piers are consistent. This result indicates that collisions between heavy trucks and piers can be well simulated by using the equivalent model of heavy truck.



Fig. 2 - Damage characteristics of the pier of the G1011 Ha-Tong high-speed K302+095 separated overpass

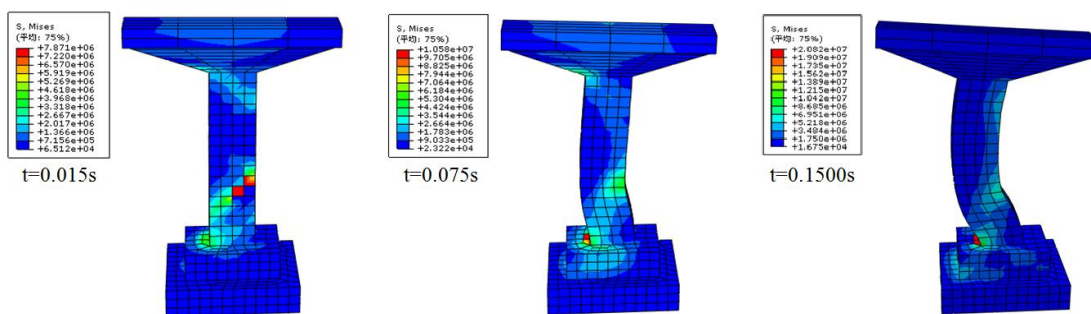


Fig. 3 - Von Mises stress cloud diagram of piers under truck impact

ANALYSIS OF THE RESULTS AND DISCUSSION

Analysis of impact force

Figure 4 presents the time-history curve of the impact force of trucks with a mass of 20 t at different impact speeds on the basis of the velocity 60–120 km/h driving range of cars as indicated by the provisions of the expressway. As shown in the figure, the peak impact force in the curve represents the maximum contact force between the anti-collision beam and the pier, the maximum impact force between the engine and the pier, the maximum contact reaction force borne by the cargo in the carriage and the peak impact force generated by the coupling vibration of the cargo and the locomotive in the late stage.



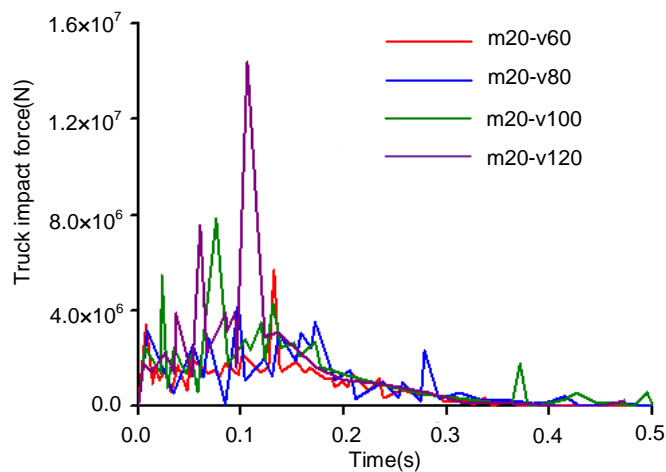


Fig.4 - Time-history curve of truck impact force with a mass of 20t

To clearly show the peak impact force and its corresponding time, Figure 5(a) displays the corresponding time of the peak impact force at different parts of a truck with a mass of 20t at different impact speeds. As shown in the Figure 5(a), the impact process of trucks and piers is different under different impact speeds. In the low-speed impact condition (m20t-v60m/s), only the anti-collision beam and the engine have collision contact, and the cargo has no collision contact. The reason for this situation is that the impact speed of the truck is relatively small, the locomotive consumes a great amount of kinetic energy during the impact process and no hard contact with the cargo occurs to produce the peak impact force. As the impact speed increases (m20t-v80m/s, m20t-v100m/s and m20t-v120m/s), the truck's kinetic energy increases and the cargo makes impact contact in addition to the collision beam and engine. Moreover, the time of collision contact between truck parts is early.

Figure 5(b) shows the impact force peaks at different parts of a truck with a mass of 20t at different impact speeds. At low-speed impact, the peak impact force of the engine is the largest among all the components. With the increase in impact speed, the peak impact force of the cargo increases gradually and gradually exceeds the peak impact force of the engine. In addition, as the impact speed increases, the peak impact force produced by the truck's engine increases when it hits the pier. Under the impact speed of 80 km/h, the variation trend of the peak impact force has different results due to the complexity of the truck's internal structure. Under certain impact speeds, the front and the pier will consume a great amount of energy due to coupling vibration before impact contact.

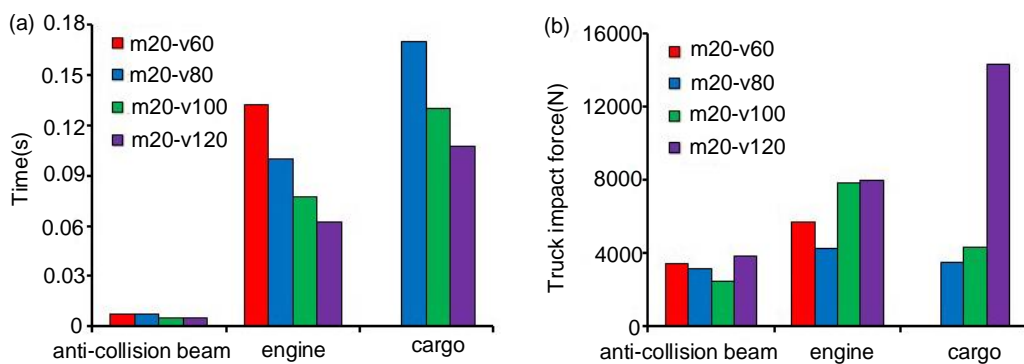


Fig. 5 (a) - Time corresponding to the peak impact force of each part of the truck; (b) Peak impact force of each part of the truck

Figure 6 shows the time–history curves of the impact forces of trucks with different masses at the impact speed of 80 km/h. The mass of the truck was changed by changing the material density of the cargo.

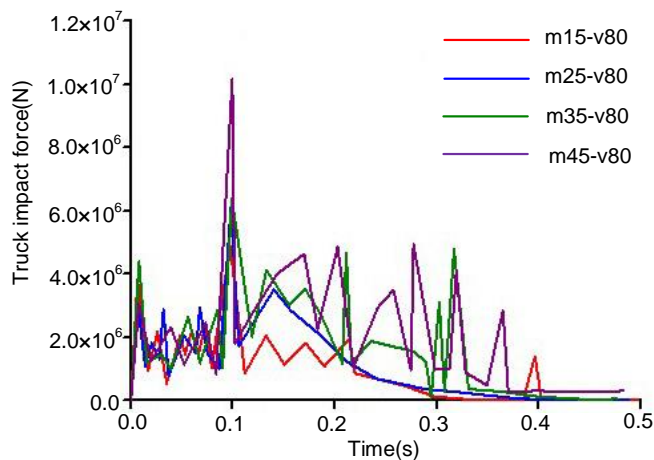


Fig. 6 - Time–history curve of impact force of truck with a speed of 80 km/h

As shown in the Figure 6, the duration of the impact process is approximately 0.4 s. When the truck has a small mass, the impact energy consumption mainly occurs in the front. With the increase in the mass of the cargo, the peak of the impact force increases during collision. This phenomenon is due to the coupling vibration effect of the steel frame of the truck body after the collision between the compressed front and the cargo.

Figure 7 shows the impact force peaks and the corresponding time of different parts of trucks with different masses under impact speed of 80 km/h.

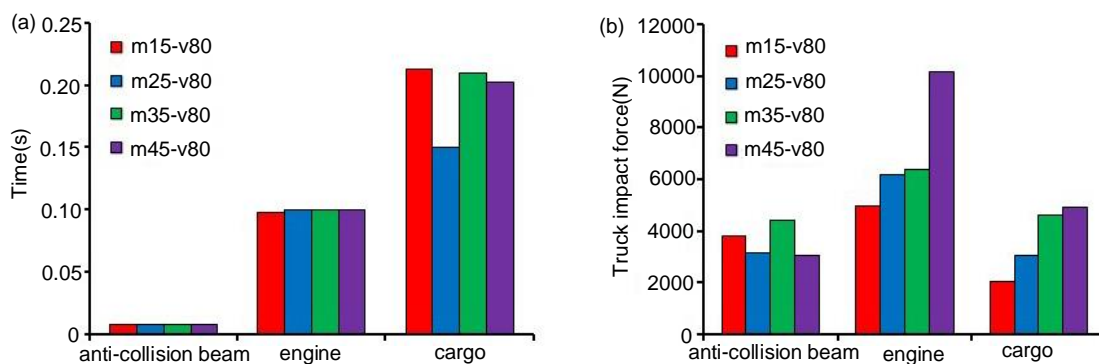


Fig. 7 (a) - Time corresponding to the peak impact force of each part of the truck; (b) peak impact force of each part of the truck

As shown in the Figure 7, under a certain impact speed, the time of peak impact force generated by the collision of anti-collision beams and engines of trucks of different masses remains unchanged. The time of peak impact force due to the impact of the cargo varies with mass. In addition, with the increase in the truck mass, the peak impact force increases, and the maximum peak impact force is generated by the impact with the engine.

Stress analysis

The stress response of each part is an important basis for judging the damage degree of the pier and its anti-collision design when it is hit by vehicles. Figure 8 shows the von Mises stress distribution cloud diagram of the pier hit by a truck with a mass of 20 t under different impact speeds at the moment of impact force peak of all components. As shown in the Figure 8(a)~(d), when the collision peak of the anti-collision beam of the truck occurs, the von Mises stress distribution of the piers extends to the top and bottom at a 45° angle along the front contact surface. This result indicates that when the anti-collision beam of the truck contacts the piers, local damage and cracks will occur in the concrete. During continuous compression deformation of the anti-collision beam, front shell and chassis steel frame, the stress at the top of the pier column decreases and that at the bottom of the pier column increases. The maximum stress occurs at the back of the pier's impact point, the junction of the pier and the foundation. When the engine begins to undergo impact contact, the stress is mainly concentrated near the impact point of the truck chassis and the base of the bridge pier. At this time, the impact point and the base of the bridge pier are seriously damaged. As the impact proceeds, the von Mises stress distribution of the piers does not change significantly at the cargo impact stage. However, with the increase in the truck impact speed, the deformation of the piers increases. In addition, the impact position of the piers and the high stress distribution area of the pier base increase, forming a 45° through-crack to promote the development of cracks. In addition, the Figure 8 shows that the high-stress area is concentrated at the collision position and the base of the pier.

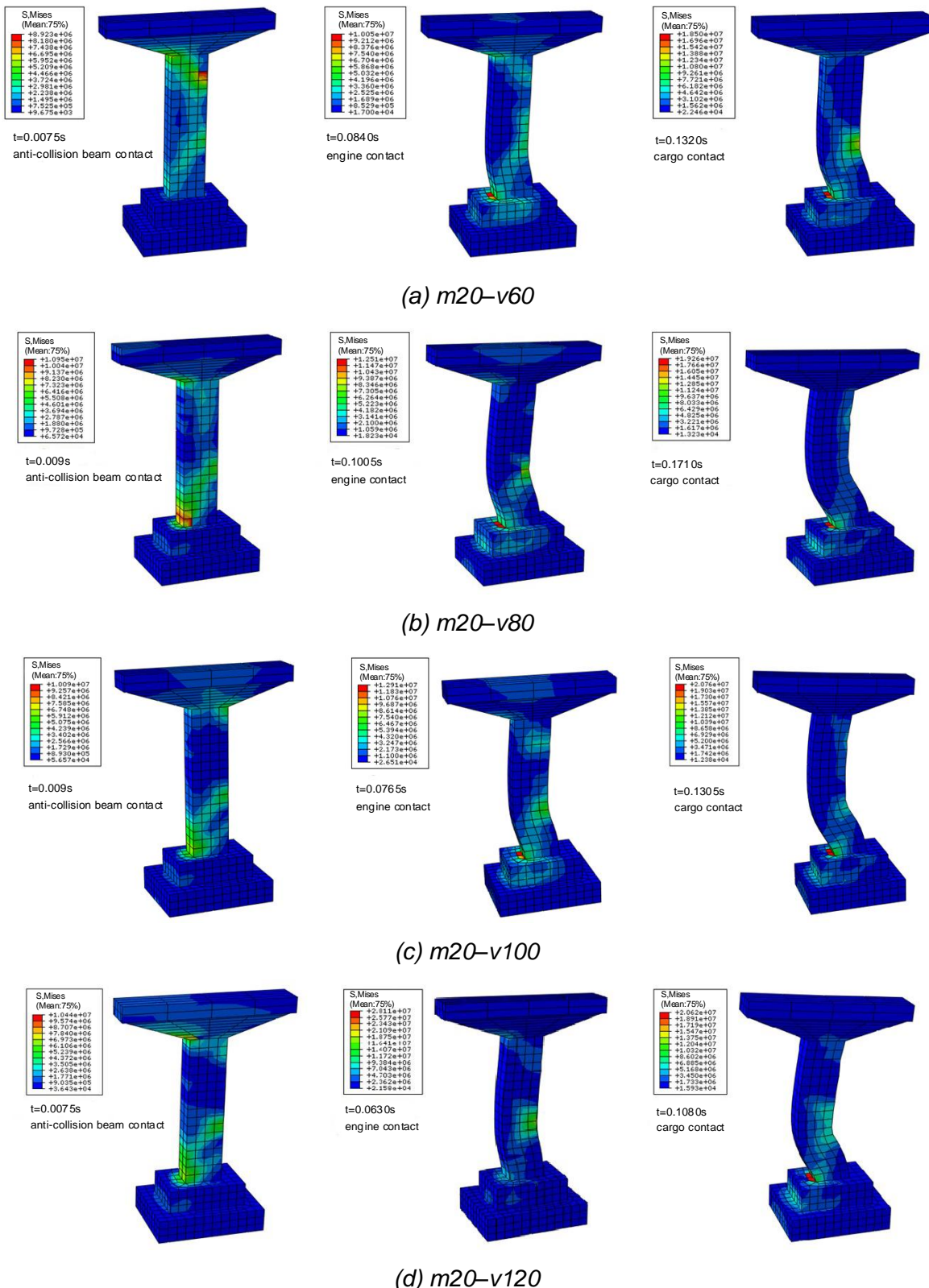


Fig. 8 - Von Mises stress cloud diagram of piers under different impact speeds

Figure 9 shows the von Mises equivalent stress time–history curve of a truck with a mass of 20t at different impact speeds. As shown in the Figure 9, the stress of the truck increases rapidly at the beginning of contact with the pier and then decreases after reaching a peak value as a result of the collision between the anti-collision beam of the truck and the pier. With the compression deformation of the front, the stress continues to increase and reaches the maximum value of the impact process. As the energy dissipates, the stress decreases and remains at a low level. In addition, the Figure 9 shows no obvious change in the maximum von Mises stress with the increase in the truck impact speed, but the time point at which the maximum stress is produced is different. Moreover, the maximum von Mises stress on the impact position of the pier is higher than that on the base of the pier.

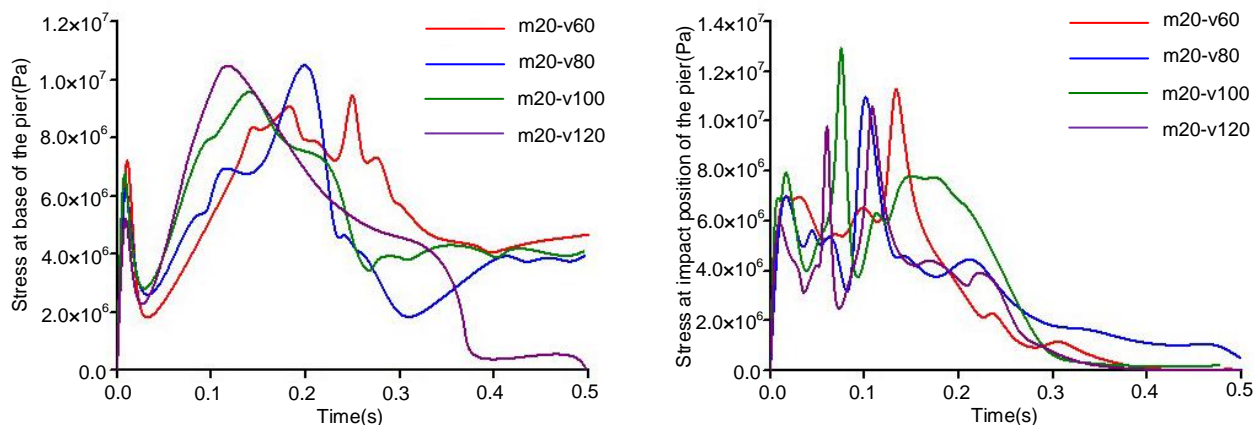


Fig. 9 - Time–history curves of the von Mises stress of impact position and the base of the pier at different impact speeds

Figure 10 shows the peak impact force moment of each part of the trucks with different masses at the impact speed of 80 km/h and the von Mises stress distribution of the pier. As shown in the Figure 10(a)~(d), when the anti-collision beam initially impacts the pier, the pier column does not deform. However, the impact of the pier generates stress, which then spreads to both ends to form a strip stress area, and the strip has a 45° angle with the axis of the column. With the compression process of impact, the engine will collide with the bridge, and the pier will show deformation characteristics. The maximum von Mises stress distribution will be located around the impact position and the base of the pier. When the cargo collides with the bridge, the pier deforms further. In addition, the high-stress areas of the impact position and the base of the pier expand and become a whole, forming through-cracks.

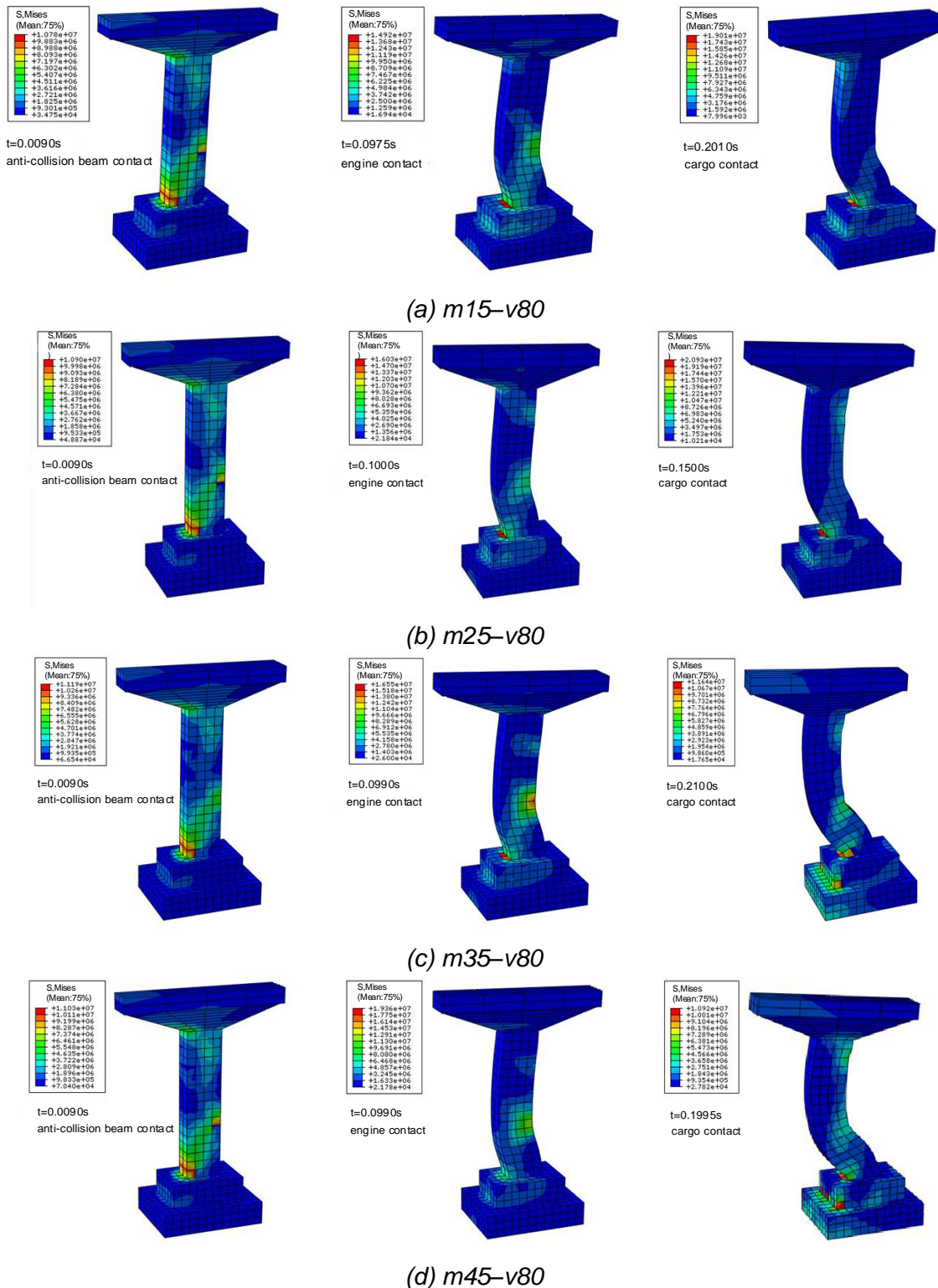


Fig. 10 - Von Mises stress cloud image of the piers impacted by trucks with different masses

Figure 11 shows the time–history curves of the von Mises equivalent stress at the impact position and base of piers with different masses of trucks at the impact speed of 80 km/h. As shown in the Figure 11, the stress increases rapidly at the initial moment when the truck and the



pier experience impact and then decreases after reaching the peak, forming a triangular pulse as a result of the collision of anti-collision beams and piers. With the compression deformation of the front, the stress at the base of the piers increases and reaches the maximum during the impact process. The stress at the pier's impact point remains at a high level and reaches the maximum stress value during the impact process after the shock. As the energy dissipates, the stress begins to decrease and eventually remains at a low level. In addition, with the increase in the truck mass, the maximum von Mises stress at the pier base does not change significantly because the deformation at the base of the pier causes the material to reach its strength limit, the stress of the pier is released after failure.

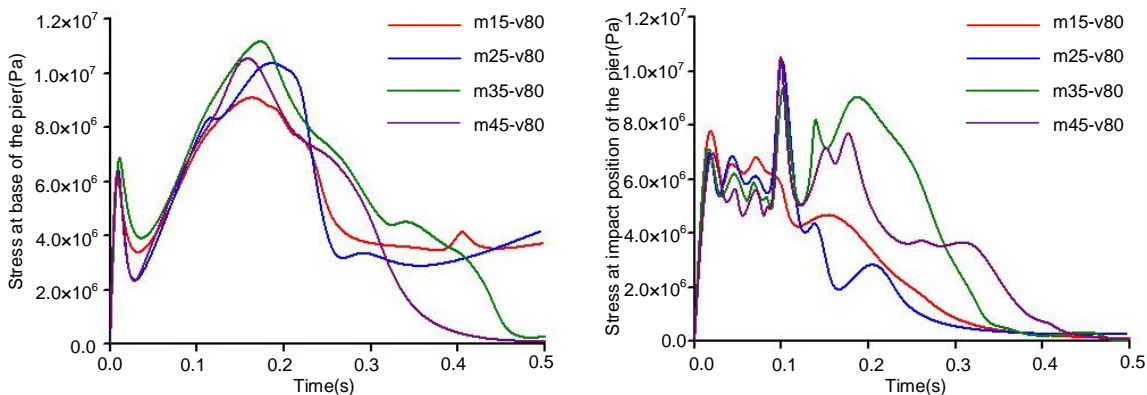


Fig. 11 - Von Mises stress time-history curves of the impact of trucks with different masses on the base and the impact point of the piers

CONCLUSION

In this paper, an equivalent truck finite element model is developed on the basis of the numerical simulation method to analyse the collision between heavy trucks and piers. This model combines the advantages of the fine finite element model and the simplified finite element model and considers the impact effect of heavy vehicles. The results show that with the increase in mass and impact speed, the kinetic energy of the truck and the peak impact force increase. The von Mises stress at the base and impact position of the piers is large. In addition, with the increase in truck mass and impact speed, the deformation of the pier increases and the stress areas are connected as a whole, thereby forming an oblique through-crack with a 45° angle to the axis of the pier column.

In sum, the equivalent truck finite element model is developed, taking the main structural components of trucks into account. In addition, the effects of truck mass and impact speed on the impact force and piers von Mises stress are analysed, thereby providing a new theoretical basis for the limitations of high-speed impact of heavy trucks on piers in anti-collision design and code.

REFERENCES

- [1] Chen Lin., 2015. Research on Bridge Piers Against Vehicle Impact. Hunan University, 2015
- [2] Tsang H, Lam N T K. ,2008. Collapse of Reinforced Concrete Column by Vehicle Impact. Computer-Aided Civil and Infrastructure Engineering, vol. 23: 427-436
- [3] Thilakarathna H M I, Thambiratnam D P, Dhanasekar M et al., 2010. Numerical Simulation of Axially Loaded Concrete Columns under Transverse Impact and Vulnerability Assessment. International Journal of Impact Engineering, vol. 37(11): 1100-1112



- [4] Ferrer B, Ivorra S, Segovia E et al., 2010. Tridimensional Modelization of the Impact of a Vehicle against a Metallic Parking Column at a Low Speed[J]. Engineering Structures, vol. 32(8): 1986-1992
- [5] Buth C E, Brackin M S, Williams W F et al., 2011. Collision Loads on Bridge Piers: Phase 2. Report of Guidelines for Designing Bridge Piers and Abutments for Vehicle Collisions. Texas: Texas Transportation Institute Proving Ground:1-87.
- [6] Sharma H, Hurlebaus S, Gardoni P., 2012. Performance-Based Response Evaluation of Reinforced Concrete Columns Subject to Vehicle Impact. International Journal of Impact Engineering, vol. 43: 52-62
- [7] Joshi A S, Gupta L M., 2012 A Simulation Study on Quantifying Damage in Bridge Piers Subjected to Vehicle Collisions. International Journal of Advanced Structural Engineering (IJASE), vol. 4(1): 1-13.
- [8] Gomez N, Alipour A., 2014. Study of Circular Reinforced Concrete Bridge Piers Subjected to Vehicular Collisions. Structures Congress 2014, Boston, 577-587.
- [9] Popp C., 1961. Der Querstoß beim Anprall von Kraftfahrzeugen auf Stützen und Rahmenstiele von Straßenunterführungen. Köln: Stahlbau-Verlag
- [10] Zhu Yadi, Lu wenliang., 2013. Model tests for collision force between a vehicle and piers, Journal of Vibration and Shock, vol. 32(21): 182-185.
- [11] El-Tawil S, Severino E, Fonseca P., 2005. Vehicle Collision with Bridge Piers. Journal of Bridge Engineering, vol. 10(3): 345-353.
- [12] Agrawal A K, Liu G, Alampalli S., 2013. Effects of Truck Impacts on Bridge Piers. Advanced Materials Research, vol. 639-640: 13-25.
- [13] Lu Wenliang, Li Xiaolong, Peng Boyang, et al., 2012. Analysis of collision dynamic response of vehicle Pier and column Model. Railway Engineering, No.3:12-13+95
- [14] Xu Linfeng., 2014. Research on impact force and strain of bridge pier caused by vehicle collision, dissertation for the degree of master(Beijing Jiaotong University):25-90
- [15] Liu Shan., 2017. Research on impact force of reinforced concrete pier impacted by vehicle, dissertation for the degree of master(Northern University of Technology):9-68

EXPERIMENTAL STUDY ON THE SEISMIC DAMAGE OF AEOLIAN SAND CONCRETE COLUMNS WITH DIFFERENT REINFORCEMENTS

Yaohong Wang, Xiaoyan Ma, Qing Han, Qi Chu and Zeping Zhang

Inner Mongolia University of Technology, School of Civil Engineering, Hohhot, Inner Mongolia, China; wyh@imut.edu.cn, 20171800217@imut.edu.cn,
19880000016@imut.edu.cn, 20171100260@imut.edu.cn, 20171800225@imut.edu.cn

ABSTRACT

Aeolian sand is a kind of natural material with abundant reserves and a low price. Many scholars have conducted extensive studies on the engineering applications of aeolian sand. This paper addresses the seismic damage behaviour of aeolian sand concrete columns to promote the application of aeolian sand in frame structures. A total of 5 aeolian sand concrete column specimens with different reinforcements were studied using cyclic loading tests. The failure modes, stiffness degradation, bearing capacity, hysteresis peculiarity, ductility, and energy consumption of the specimens were analysed and compared. Then, applicable damage models of the specimens were proposed. The study results prove that the seismic damage behaviour of the specimens increases with the increase of longitudinal reinforcement percentage and with the transverse steel ratio when the replacement percentage of aeolian sand is constant. Additionally, the damage model which is revised in this paper agrees well with the test results. It can be used to assess the degree of damage to the aeolian sand concrete columns.

KEYWORDS

Aeolian sand, Seismic damage behaviour, Longitudinal reinforcement percentage, Transverse steel ratio

INTRODUCTION

With the worldwide development of infrastructure construction, increasing quantities of engineering sand have been exploited from rivers and mountains to meet the needs of concrete production. The mass application of ordinary engineering sand will cause vast economic costs and environmental damage. Meanwhile, the ecosystems of arid and semi-arid regions are seriously threatened by desertification where the trigger is aeolian sand. Given these circumstances, many scholars have conducted studies on concrete that uses aeolian sand to promote the harmonious coexistence of man and nature. W. Dong et al [1] studied the incorporation of aeolian sand can improve the compressive strength and tensile strength of concrete, especially for the early strength of concrete. H. F. Liu et al [2] analysed the effects of a series of mix-ratio parameters on the compressive strengths and splitting tensile strengths of aeolian-sand concrete. These mix-ratio parameters included replacement percentages of aeolian sand, coal ash content, sand ratio and water-to-binder ratio. It can be concluded that with an increase in the replacement percentage of aeolian sand and the coal ash, the strength of concrete first increased and then decreased. When the replacement percentage of aeolian sand was 20%, the strength of aeolian sand concrete reached a maximum. H. X. Yuan [3] studied the bonding properties between aeolian-sand concrete and steel bars. The results showed that the bonding properties are largely consistent with those of



ordinary reinforced concrete in 4 aspects, including concrete strength grades, anchorage lengths of steel bars, diameters of steel bars and thicknesses of protective layers. It can be demonstrated that the formula which is used to calculate adhesive property between concrete and steel bars for ordinary reinforced concrete can be applied to aeolian-sand concrete. G. Q. Wang et al [4] studied the seismic behaviour of 2 specimens which included an ordinary sand concrete column and a aeolian-sand concrete column using a cyclic loading test. The results showed that the seismic damage behaviour of aeolian sand concrete columns is superior to that of ordinary sand concrete columns. H. P. Yin et al [5] carried out a low-cycle repeated load test with an ordinary concrete column and 4 fully recycled concrete columns. The test results manifested that the bearing capacity, stiffness and energy consumption of the columns improved on increasing in the reinforcement percentage of recycled aggregate. Y. Q. Zhang et al [6] conducted experimental research on 5 short recycled concrete columns with different transverse steel ratios. The test and analysis results indicated that the ductility, bearing capacity and energy consumption of the short recycled concrete columns improved with increasing of the transverse steel ratio. However, when the transverse steel ratio exceeded a certain limit, the extent of improvement of the above behaviours was limited.

At present, domestic and foreign scholars have made quite achievements in the application of desert sand in concrete. However, most of the research work focuses on the study of the mechanical properties of desert sand concrete. Only a few scholars have conducted experimental research on the performance of desert sand concrete specimens. Based on existing results, this paper studies the seismic damage to aeolian sand concrete columns with different reinforcement configurations. Cyclic loading tests and damage analyses for 5 concrete column specimens were used to achieve the study objectives. The failure modes, stiffness degradation, bearing capacity, hysteresis peculiarity, ductility, and energy consumption of the specimens were analysed and compared. Then, an applicable damage model of the specimens was proposed.

TEST PROGRAM

Details of specimen

The specimens include 5 columns with the same geometric dimensions, shear span ratios and axial compression ratios. The specimens are designated ASC1, ASC2, ASC3, ASC4 and ASC5. The replacement percentage of aeolian sand for all specimens is 20%. The calculated height of each specimen is 875 mm, and the section dimensions of each column are 250 mm x 250 mm. The characteristics of the columns are displayed in Table 1. Details of aeolian sand concrete columns are displayed in Figure 1.

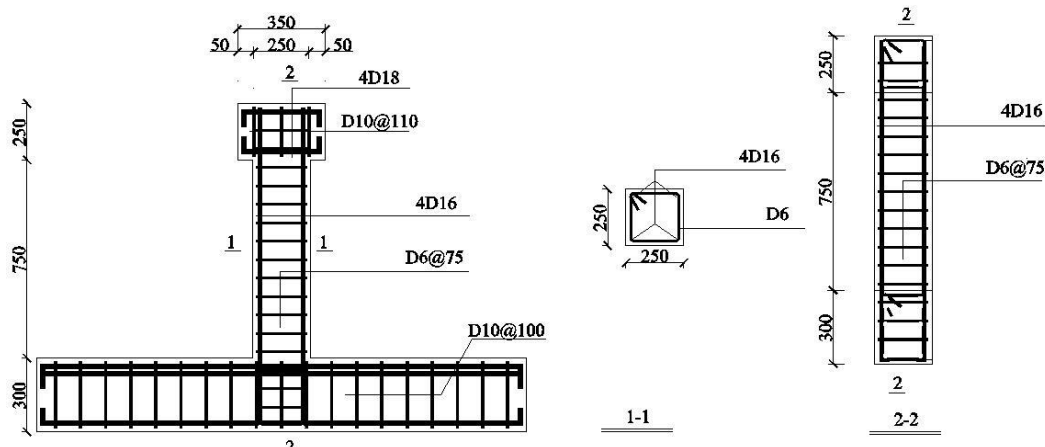
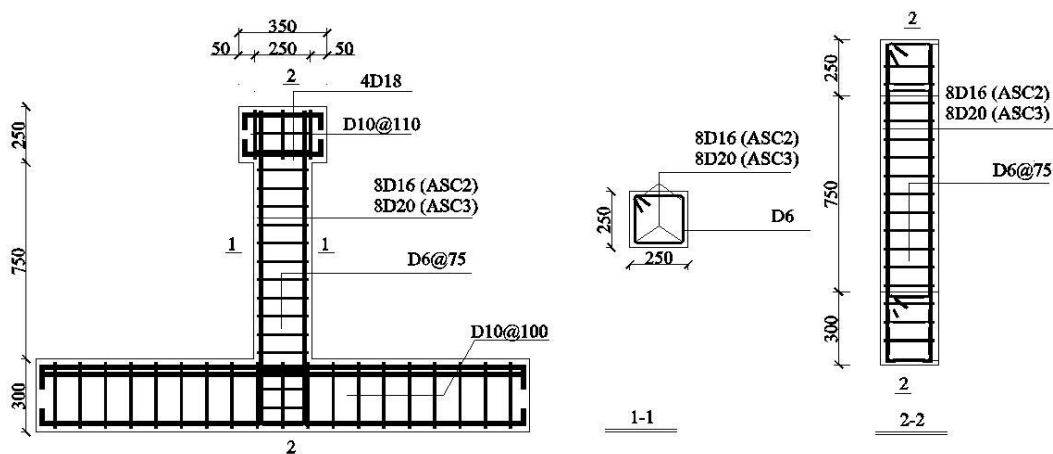
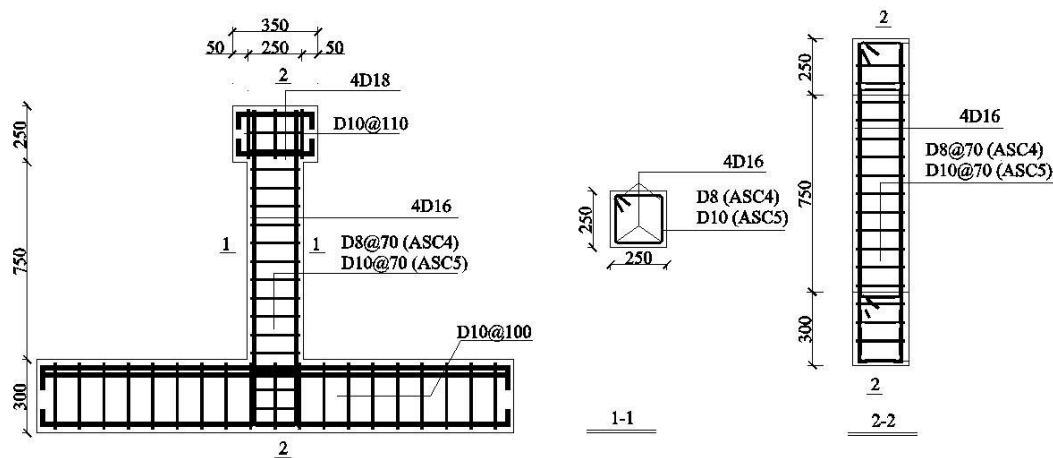


Fig. 1 – Details of aeolian sand concrete columns (a) ASC1





(b) ASC2, ASC3



(c) ASC4, ASC5

Fig. 1 – Details of aeolian sand concrete columns

Tab. 1 - Characteristics of the columns

Specimen number	ASC1	ASC2	ASC3	ASC4	ASC5
Axial compression ratio	0.2	0.2	0.2	0.2	0.2
Shear span ratio	3.5	3.5	3.5	3.5	3.5
Longitudinal reinforcement percentage	1.20%	2.30%	3.50%	1.20%	1.20%
Transverse steel ratio	0.60%	0.60%	0.60%	1.00%	1.40%

Material properties

The concrete of 5 columns is the same group. The types of material sand mix ratio of concrete are displayed in Table 2 below. The cubic compressive strength can be measured through using a compression machine, which is displayed in Table 3. A tensile tester can measure the yield strength and ultimate strength, which is displayed in Table 4.



Tab. 2 - Types of materials and mix ratio of concrete

Types of materials	Water	Stone	Ordinary sand	Aeolian sand	Coal ash	Cement	Water reducer
Weight (kg·m ⁻³)	205	1266.36	393.98	98.49	43.62	389.28	3.27

Tab. 3 - Mechanical properties of concrete

Specimen	f _{cu,t} /MPa
ASC1	38.3
ASC2	40.7
ASC3	36.2
ASC4	35.6
ASC5	37.1

Tab. 4 - Mechanical proprieties of steel materials

Types of reinforcement	Yield stress (MPa)	Ultimate stress (MPa)
Steel bar D6	412.5	542.6
Steel bar D8	426.4	533.7
Steel bar D10	439.5	562.1
Steel bar D16	403.1	534.7
Steel bar D20	432.8	541.4

Test set-up

The cyclic loading tests were conducted at the Key Laboratory of Civil Engineering Structure and Mechanics at the Inner Mongolia University of Technology, China. The test devices are displayed in Figure 2. The height of the horizontal loading center away from the bottom of columns is 875 mm.

After the vertical pressure was applied to the vertical jack, the axial compression ratio was maintained constantly throughout the test. A horizontal low-cycle reciprocating load was applied by manipulating the pushing and stretching of the horizontal jack. In the tests, the load control method was used first. When the skeleton curve shows a significant inflection point, it is considered to enter the yield stage. Then, the displacement control method was used. The displacement of each step was integer multiples of the yield displacement. The loading continued until the bearing capacity of the specimens dropped to 85% of the peak load. In total, there were 3 electronic displacement gauges deployed in the test. They were used to measure the displacement of the specimens.



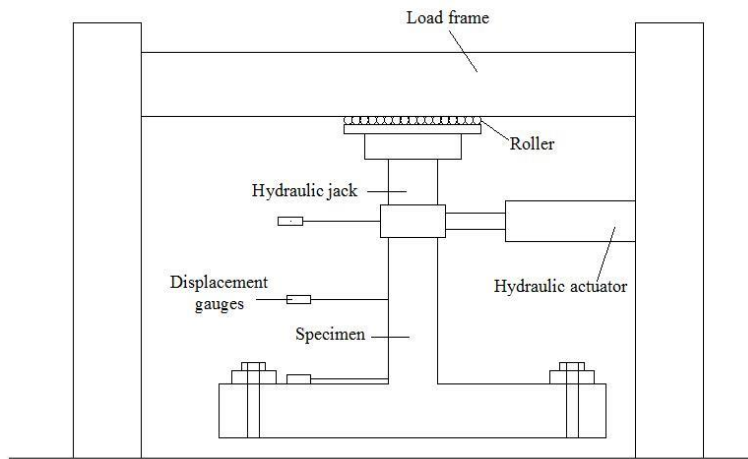


Fig. 2 – Test devices

RESULTS AND DISCUSSION

Destructive form of specimens

Specimen ASC1

As the load reached 21.8kN in the forward direction of the fourth cycle, a few horizontal cracks formed on the bottom of the column. The widths of these cracks were all approximately 1.5 mm. In the negative direction, 2 cracks formed in the middle and lower parts of the specimen. As the load reached 56.8kN, a wider crack with an angle of approximately 45° appeared approximately 300mm from the bottom of the column. The existing cracks were gradually widened. As the force reached 79.5kN, a large crack with an angle of approximately 60° formed at the bottom of the specimen, with slight spalling of the concrete. The width of this crack was approximately 5.6 mm. After this, more cracks quickly developed and intersected each other. When the specimen was broken, the concrete on the bottom of the column was crushed and peeled off over a large area. Concurrently, the stirrup and the longitudinal reinforcements were exposed and seriously buckled.

Specimen ASC2

The first cracks formed in the middle and lower parts of the column. As the positive force reached 32.8kN, a few new cracks with lengths ranging from 56 mm to 93 mm formed at the bottom of the column. When the positive force reached 83.7kN, many oblique cracks formed in the middle and lower parts of the column and were inclined downward by 30°. In the following negative direction, these oblique cracks rapidly developed and intersected each other. As the force reached 124.3kN, the existing cracks continued to expand, accompanied by the sound of cracking concrete. As the loading force was 144kN, the concrete on both sides of the bottom of the column started to peel off. As the column was destroyed, the concrete at the bottom was completely crushed. It can be observed that the stirrup and longitudinal reinforcements were exposed and yielded.

Specimen ASC3

As the force reached 68.6kN, a few new cracks with lengths ranging from 32 mm to 54 mm formed at the bottom of the column. As the force reached 138.5kN, a few new cracks with lengths ranging from 71 mm to 87 mm formed in the middle of the column. As the force increased, the cracks gradually expanded and developed. As the loading reached 153.8kN, there were a few new oblique cracks whose length was approximately 72 mm to 95 mm that formed in the middle and upper parts of the column. The development form of the existing cracks changed from length extension to width extension. The concrete in the plastic hinge area began to show signs of

loosening. When the specimen was broken, the concrete of the root segment was completely crushed and peeled off over a large area. The exposed longitudinal steel bar and stirrup were stretched and bent.

Specimen ASC4

As the load reached 43.2kN, the earliest cracks with a maximum length of 68 mm, which located in the lower part of the column. When the force was 95.8kN, there were many cracks in the middle and lower parts and almost extended obliquely down 60°. Some cracks on the right side of the root segment extended to the left with a slight peeling of the concrete. The cracks on the left side of the root segment were inclined downward 30° along the foundation beam. As the load was 147.8kN, the cracks in the middle and lower parts continued to develop. Some cracks showed a lightning shape. Subsequently, more cracks quickly developed and intersected each other. When the specimen was broken, the concrete on both sides of the root segment was crushed and peeled off. The longitudinal bar was exposed on the right side and was clearly bent. Additionally, the stirrup of the root segment was exposed and had yielded.

Specimen ASC5

As the load reached 48.4kN in the negative direction, the 5 earliest cracks formed in the lower parts of the column. The cracks developed rapidly and were distributed horizontally. As the load was 138.5kN, some cracks in the lower part showed a lightning shape and penetrated each other. On the right side, a crack of 56 mm in length extended from the root segment of the specimen to the middle and lower parts of the specimen and followed an angle of approximately 60°. As the peak load was 158.3kN, the largest crack in the root segment of the specimen widened to 4.2 mm. Concurrently, the concrete of the root segment began to partially peel off. When the specimen was broken, the concrete of the root segment was completely crushed and peeled off over large areas. The results indicated that the stirrup and longitudinal reinforcement were exposed and had seriously buckled.

The destructive forms of the specimens are displayed in Figure 3. The details of damage when the specimens were broken are displayed in Figure 4. During the tests, the failure processes of the specimens were recorded in detail. When the specimens were under the same load, the degree of damage decreased with an increase in the longitudinal reinforcement percentage and in the transverse steel ratio.



(a)ASC1

(b)ASC2

(c)ASC3

(d)ASC4

(e)ASC5

Fig. 3 – The destructive form of the specimens



(a)ASC1

(b)ASC2

(c)ASC3

(d)ASC4

(e)ASC5

Fig. 4 – Details of damage when the specimens were broken

Skeleton and hysteresis curves of specimens

The hysteresis and skeleton curves for the 5 specimens are shown in Figures 5 and 6. The figures show that the specimens are basically in an elastic stage at the beginning of each test. The hysteresis curves rise along an approximately straight line during this period. With the continuous increase in force value and displacement, the hysteresis curves change flexibly. The residual strain increases continuously. Additionally, the stiffness gradually degenerates. After the specimens yielded, the horizontal displacements rise significantly faster than the horizontal loads. After the force reaches its peak load, the bearing capacity declines with the number of load augmentations. In general, for the specimens whose reinforcements have been strengthened, the bearing capacity decreases more slowly, and the hysteresis curves are relatively fuller. This indicates that they have stronger energy dissipation capacities.

From a comparison of the hysteresis curves and skeleton curves of specimens ASC1 to ASC3, we observe some rules, which are mentioned next. Due to the earlier cracking of concrete, specimen ASC1 shows a more obvious pinching phenomenon, which leads to a significantly lower energy consumption and poorer hysteresis performance of the specimen compared to others 4 specimens. The maximum loads of the columns gradually increase with the increase of longitudinal reinforcement percentages and transverse steel ratios. The reinforcement using longitudinal reinforcement can assist the specimens in withstanding axial pressures and in reducing creep deformation and cross-sectional dimension. Thus, this reinforcement can effectively enhance the bearing capacity of aeolian sand concrete specimens to increase the longitudinal reinforcement percentage.

From the comparison of the hysteresis and skeleton curves of specimens ASC1, ASC4 and ASC5, we can present some rules as follows. Specimens ASC4 and ASC5, with smaller stirrup spacing, show relatively gentle transitions in the skeleton curves. The bearing capacity of these 2 specimens declines more slowly than that of specimen ASC1. In other words, the maximum load per loading cycle of specimens gradually rises with the increases in the transverse steel ratio and with a decrease in stirrup spacing. This increase is because the stirrup can effectively prevent the development of oblique cracks and enhance the synergistic work between the concrete and the steel bars. Thus, this is an effective method to enhance the bearing capacity of aeolian sand concrete specimens by increasing the transverse steel ratio.

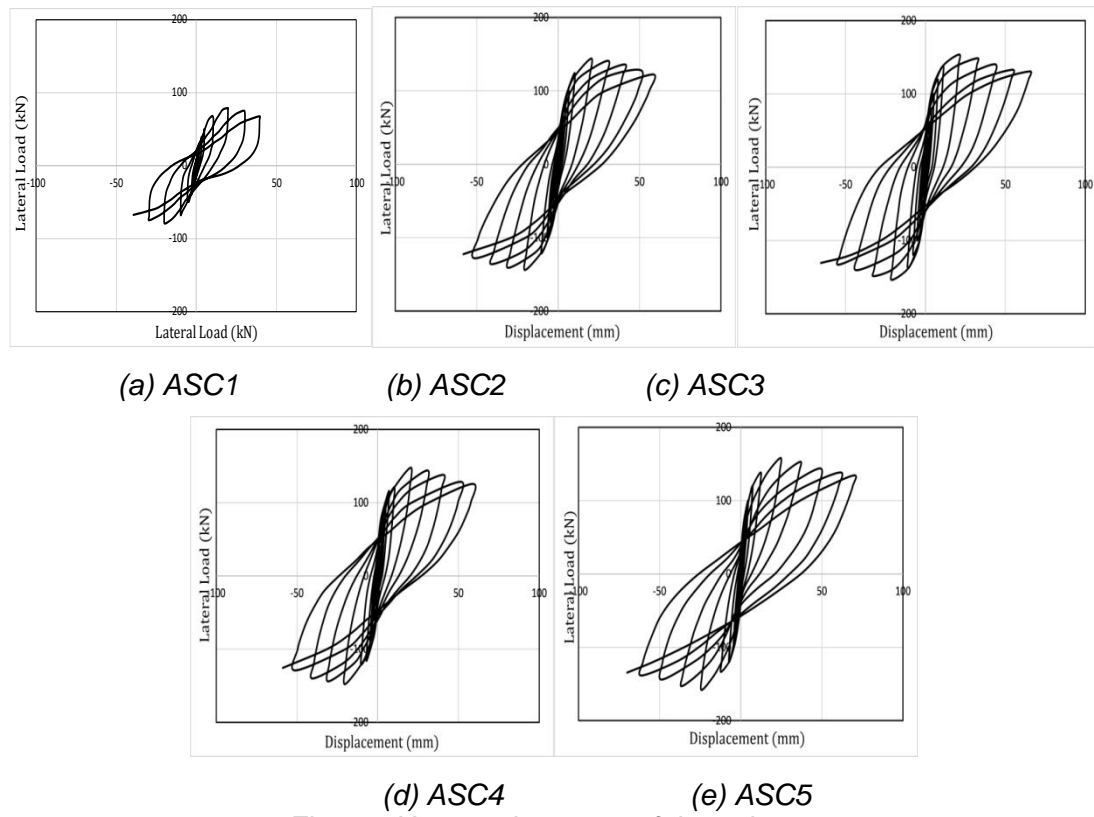


Fig. 5 – Hysteresis curves of the columns

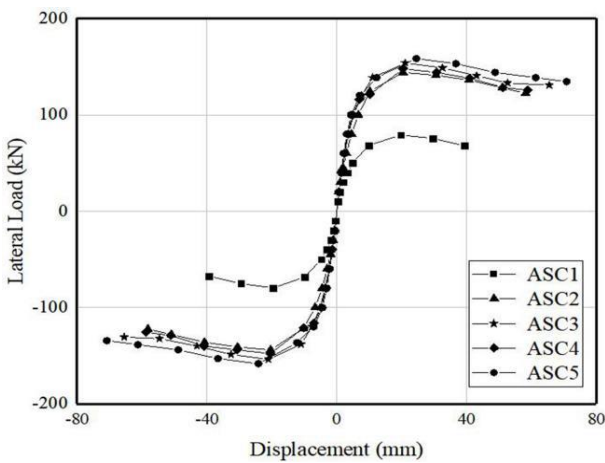


Fig. 6 – Skeleton curves of the columns

Feature points and ductility of columns

The feature points of specimens measured are shown in Table 5. In Table 5, F_{cr} is the cracking load and Δ_{cr} is the cracking displacement. F_y is the load at the time of yielding of the specimen and Δ_y is the yield displacement. F_{max} is the maximum horizontal load and Δ_{max} is the displacement. When loading is lower than 85% of the peak load, the specimen declared failed. At this point, Δ_u is the displacement displacement and F_u is the load when the specimen is failed.

Tab. 5 - Loading capacity of columns

Specimen	Original cracking		Yielding		Ultimate stage		Failure stage	
	F _{cr} (kN)	Δ _{cr} (mm)	F _y (kN)	Δ _y (mm)	F _{max} (kN)	Δ _{max} (mm)	F _u (kN)	Δ _u (mm)
ASC1	21.8	0.98	68.31	9.85	79.65	19.7	67.7	39.5
ASC2	32.8	1.84	124.3	10.19	144	20.38	122.4	58.2
ASC3	35.4	2.01	138.2	11.02	153.8	21.08	130.73	65.48
ASC4	43.2	1.96	121.2	10.23	147.8	20.46	125.6	58.83
ASC5	48.4	2.08	133.5	12.26	158.3	24.53	134.5	70.86

The displacement ductility coefficients of columns measured are shown in Table 6. The formula for calculating the ductility coefficient is Δ_u/Δ_y . There are many methods used by scholars to judge the yield of specimens. The energy equivalent method [7] was used in this paper.

Tab. 6 - Ductility coefficients of columns

Specimen	Ductility coefficient	Relative value of the ductility coefficient
ASC1	4.01	1
ASC2	5.71	1.42
ASC3	5.94	1.48
ASC4	5.75	1.43
ASC5	5.78	1.44

From Tables 5 and 6, we can draw the following conclusions:

The ductility coefficient of specimen ASC1 is the smallest of all specimens. It indicates that the aeolian sand concrete column specimens have relatively better ductility.

Compared with ASC1, specimens ASC2 and ASC3 have an increase in bearing capacity of 80.79% and 93.09%, respectively. The ductility coefficients of the 3 specimens increased approximately linearly as the increase in the longitudinal reinforcement percentage.

Compared with ASC1, specimens ASC4 and ASC5, with greater transverse steel ratios and smaller stirrup spacing, have higher ultimate deformations and bearing capacities. This is mainly because the strengthening of the edge constraint of the specimen increases the frictional bite force of the crack surfaces. This effect can resist the slip failure of oblique shear planes and delay the development of concrete cracks. This effect is conducive to allow the full expression of the plastic deformation ability of various materials.

In all, strengthening the longitudinal reinforcement percentage and the transverse steel ratio can markedly improve the ductility and bearing capacity of aeolian sand concrete specimens. We can further consider enhancing the replacement percentage of aeolian sand for economic reasons without sacrificing seismic damage behaviour of the specimens.

Energy dissipation

The amounts of energy consumption while the loading process is indicated by the area of the hysteresis loop. Thus, the accumulation of the area of every hysteresis loop area indicates the



total energy consumption of the specimen. The experiment results of the cumulative energy consumption of the specimens are displayed in Figure 7 and Table 7. By comparing of the energy consumption of specimens ASC1 to ASC5, we can specify some rules as follows. The energy consumption of specimen ASC1 is the smallest of all specimens. The maximum energy consumption can reach almost 5.0 times that of the ASC1. The energy consumption of specimen ASC3 increased by 27.2% over that of the ASC2. The energy consumption of specimen ASC5 is increased by 7.3% that over of the ASC4. We conclude that the energy consumption of the columns strongly increases as an increase in the longitudinal reinforcement percentage and with increases in the transverse steel ratio. In other words, the aeolian sand concrete column specimens with enhanced reinforcement can absorb more seismic energy. These columns show a better energy-consuming effect, and this is helpful for avoiding the collapse of aeolian-sand concrete structures in large earthquakes.

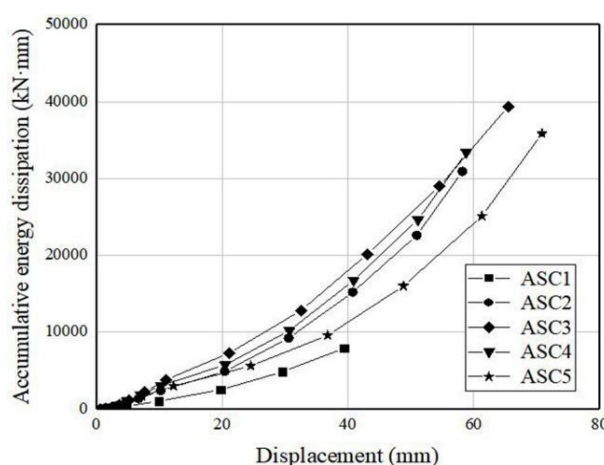


Fig. 7 –Accumulative energy consumption of columns

Tab. 7 - Cumulative energy consumption of the columns

Specimen	Cumulative energy consumption (kN·mm)	Cumulative energy consumption ratio
ASC1	7,918.930	1
ASC2	30,929.808	3.91
ASC3	39,357.441	4.94
ASC4	33,401.500	4.22
ASC5	35,833.941	4.53

Stiffness degradation

The stiffness degradation can fully reflect the damage process of specimens from cracking to plastic deformation. The stiffness can be calculated according to the following formula [8].

$$k_{x,i} = \frac{|+F_{x,i}| + |-F_{x,i}|}{|+X_{x,i}| + |-X_{x,i}|} \quad (1)$$

Where $+F_{x,i}$ is the maximum point in the forward direction of i-th loading cycle, $-F_{x,i}$ is the maximum point in the negative direction of i-th loading cycle, $+X_{x,i}$ is the displacement of i-th cycle

maximum point in the forward direction, and $-X_{x,i}$ is the i -th cycle maximum point displacement in the negative direction. As the horizontal displacement increases, the stiffness of each specimen is significantly reduced. After the specimens had cracked, the maximum point load value and maximum point displacement for every cycle were got through the test result. Then, the secant stiffness of each loading cycle was calculated. The calculation results are displayed in Table 8. The stiffness degradation curves of columns are displayed in Figure 8.

Tab. 8 - Stiffness of the columns

ASC1		ASC2		ASC3		ASC4		ASC5	
$k_{x,i}$	n								
25.35	1	29.85	1	30.3	1	30.07	1	29.4	1
20.4	0.8	27.27	0.91	27.21	0.9	27.4	0.91	28.1	0.96
16.44	0.65	23.31	0.78	24.79	0.82	25.1	0.83	26.43	0.9
12.36	0.49	20.13	0.67	22.21	0.73	23.12	0.77	25	0.85
10.34	0.41	17.7	0.59	19.38	0.64	20.66	0.69	22.52	0.77
6.93	0.27	14.99	0.5	15.52	0.51	16.57	0.55	16.59	0.56
4.03	0.16	12.06	0.4	12.55	0.41	11.85	0.39	11.09	0.38
2.55	0.1	7.07	0.24	7.3	0.24	7.22	0.24	6.5	0.22
1.72	0.07	4.61	0.15	4.57	0.15	4.69	0.16	4.17	0.14
—	—	3.34	0.11	3.26	0.11	3.4	0.11	2.95	0.1
—	—	2.51	0.08	2.43	0.08	2.52	0.08	2.26	0.08
—	—	2.1	0.07	2	0.07	2.13	0.07	1.9	0.06

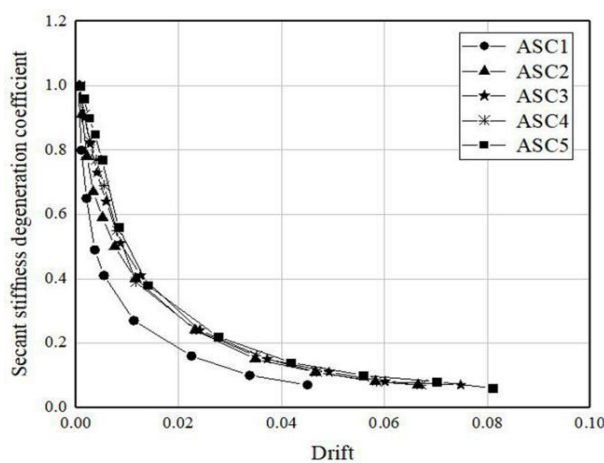


Fig. 8 –Stiffness degradation curves of columns

From the comparison of the stiffness degradation of specimens ASC1 to ASC3, we observe that the stiffness degradation speed of column ASC1 is the highest. At the initial stage of testing, concrete can contribute much to the specimen stiffness. After a specimen has cracked, the concrete in the tension zone is withdrawn from work. Then, the contribution of the longitudinal reinforcement in the tension zone to the stiffness of the specimens increases. Thus, both the initial and cracking stiffness values of the specimens are improved with an increase in the longitudinal reinforcement percentage.

From comparisons of the stiffness degradations of specimens ASC1, ASC4 and ASC5, we observed that specimens ASC4 and ASC5 have the slowest stiffness degradations during loading



the test. This is because the stirrups provide an effective lateral constraint for the specimens. The stiffness degradation of the columns is naturally improved. Therefore, that can effectively improve the stiffness degradation of the columns through increasing the transverse steel ratios.

DAMAGE MODEL

The study of the seismic damage behaviour of structures needs to involve an analysis of the damage evolution process. The damage model can measurably describe the extent of damage to structures. There are many kinds of damage assessment models, most of which have their own advantages and disadvantages. In this paper, the single-parameter damage model based on deformation and the two-parameter damage model based on deformation and energy are used to analyse the entire process of seismic damage evolution of the specimens.

Fajfar damage model-single parameter

The Fajfar model [9] uses elastic-plastic deformation to reflect the degree of damage. This model considers that the damage is caused by maximum elastoplastic deformation of the structure or of a member. The expression is:

$$D_1 = \frac{X_m - X_y}{X_u - X_y} \quad (2)$$

In Equation (2), X_m and X_y are the maximum elastoplastic deformation and yield deformation of the structure or component under cyclic loading, respectively and X_u is the limit deformation of the structure or component under cycle loading. Although this model does not consider fatigue effects, its expression is simple and easy to apply. The Fajfar model assumes that the specimen is in an elastic phase before yielding and that its damage is negligible. As the cyclic displacement increases, the damage index, D , gradually increases in a linear manner. When the bearing capacity of specimen drops to 85% of the maximum load capacity, the limit displacement reaches X_u , and the damage index, D , of the specimen reaches a value of 1.0. The specimen is defined as broken at this time. The calculation results of the specimens, which use Equation (2), are shown in Table 9.

Niu Ditao and Ren Lijie damage model two-parameter

The existing study results show that the damage to a structure under earthquake motion is not only related to the maximum deformation but is also related to the cumulative damage. Therefore, it is difficult to reflect the low-cycle fatigue effect on a structure if we only use the maximum displacement to evaluate structural damage. This practice has shown that it is more reasonable to use the two-parameter model to evaluate the seismic damage behaviour of specimens. Niu Ditao and Ren Lijie [10] proposed a damage assessment model. It is based upon deformation and energy consumption through actual seismic damage calculation and analysis. The expression is:

$$D_2 = \frac{X_m}{X_u} + \alpha \left(\frac{E_h}{E_u} \right)^\beta \quad (3)$$

In Equation (3), X_u is the limit displacement of the specimen under cycle loading and X_m and E_h are the maximum displacement and cumulative energy consumption of the column under cyclic loading, respectively. α and β are combination coefficients, reflecting the effects of deformation and energy dissipation, respectively. Niu et al. analysed the degree of damage to an actual structure in an earthquake damage investigation, and determined that $\alpha = 0.1387$ and $\beta = 0.0814$. This model uses X_m/X_u and E_h/E_u to represent the degree of damage caused by deformation and by energy consumption, respectively. This model considers the nonlinear problem and the relationship between deformation and energy. Bringing the original values of α and β into this paper, we find that the degree of damage to specimens is larger than the actual situation in



tests. Therefore, the combination coefficient in Equation (3) was revised in this paper to be consistent with test results through statistical fitting methods. The revised expression is as follows:

$$D_2 = \frac{X_m}{X_u} + 0.067 \left(\frac{E_h}{E_u} \right)^{0.65} \quad (4)$$

The calculation results of the specimens, which use Equation (4), are shown in Table 9.

Tab. 9 - Calculation results for D1 and D2

Specimen	ρ_w	ρ_s	X_m/mm	$E_h/(\text{kN}\cdot\text{mm})$	D ₁	D ₂
ASC1	0.6%	1.2%	19.70	2,498.98	0.33	0.53
			29.55	4,848.72	0.67	0.80
			39.40	7,918.93	1.00	1.00
ASC2	0.6%	2.3%	20.38	4,897.46	0.21	0.37
			30.57	9,235.81	0.42	0.56
			40.76	15,210.01	0.64	0.74
			50.95	22,607.41	0.85	0.93
			61.14	30,929.81	1.00	1.00
ASC3	0.6%	3.5%	21.08	7,286.12	0.18	0.35
			32.56	12,844.41	0.40	0.53
			43.08	20,172.46	0.59	0.70
			54.60	29,022.16	0.80	0.89
			66.12	39,357.44	1.00	1.01
ASC4	1.0%	1.2%	20.46	5,753.49	0.21	0.37
			30.69	10,235.09	0.42	0.55
			40.92	16,767.49	0.63	0.74
			51.15	24,641.74	0.84	0.92
			61.38	33,401.50	1.00	1.04
ASC5	1.4%	1.2%	24.53	5,615.69	0.21	0.37
			36.78	9,593.69	0.42	0.55
			48.82	16,011.89	0.63	0.74
			61.30	25,106.52	0.85	0.93
			73.56	35,833.94	1.00	1.05



In Table 9, ρ_w is the transverse steel ratio. ρ_s is the longitudinal reinforcement percentage. X_m is the maximum displacement during cyclic loading. E_h is the cumulative energy dissipation during cyclic loading. D_1 is the calculation result of equation (2). D_2 is the calculation result of equation (4).

Table 9 shows that D_1 is less than D_2 . The latter value is more consistent with the test process of the specimens used. We conclude that the two-parameter damage model, as revised in the article, is consistent with the actual situation. It is feasible to use this model to analyse the entire damage process of aeolian sand concrete column specimens.

CONCLUSIONS

This paper studies the seismic damage behaviour of aeolian-sand concrete columns. A total of 5 aeolian sand concrete column specimens with different reinforcement configurations were studied on the basis of cyclic loading tests. Then, an applicable damage model of the specimens was proposed. The conclusion is as below:

- (1) When under the same load, the degree of damage to aeolian sand concrete column specimens decrease with increasing of the longitudinal reinforcement percentage and transverse steel ratio.
- (2) Increasing the longitudinal reinforcement percentages and transverse steel ratios can effectively improve the stiffness degradation, bearing capacity, ductility and energy consumption of aeolian sand concrete column specimens.
- (3) From the test and analysis results, we conclude that increasing the replacement percentage of aeolian sand while increasing the longitudinal reinforcement percentages and transverse steel ratios, results in no sacrifice in the seismic damage behaviour of the specimens.
- (4) The two-parameter damage model, which is revised in the article, can be used to analyse the entire damage process of aeolian sand concrete column specimens.

ACKNOWLEDGEMENT

This paper is subsidized by the National Natural Science Foundation of China (51868059).

REFERENCES

- [1] W. Dong, et al. 2018. Effect of aeolian sand and fly ash content on mechanical properties of concrete. Bulletin of Silicate, 37(7), 237-242.
- [2] H. F. Liu, J. R. Ma, J. Fu, et al. 2015. Study on mechanical properties of desert sand concrete. Concrete (9), 80-83. (in Chinese).
- [3] H. X. Yuan. 2018. Study on Bonding Performance between Sand Concrete and HRB400 Reinforcing Bar[D]. Xinjiang University, 2018.(Doctoral dissertation in Chinese).
- [4] G. Q. Wang, Z. Q. Li , S. Yang, et al. 2018. Experimental study on seismic behavior of desert sand concrete frame columns under cyclic loading. Concrete (6).(in Chinese).
- [5] H. P. Yin. 2010. Experimental study on seismic behavior of recycled concrete columns with different reinforcement ratios. Earthquake Disaster Prevention Technology, 5(1), 99-107.(in Chinese).
- [6] Y. Q. Zhang. 2011. Experimental study on seismic behavior of short concrete columns with different hoop ratios. Building Structure (s1), 272-276.(in Chinese).
- [7] J. G. Nie , L. Zhu, et al. 2013. Experimental study on seismic behavior of steel plate shear wall. Journal of Building Structures, 34(1), 61-69.

- [8] JGJ 101-96. 1997. Specifying of Testing Methods for Earthquake Resistant Building, China Architecture & Building Press, Beijing, China.(in Chinese)
- [9] Fajfar, P. . 2010. Equivalent ductility factors, taking into account low-cycle fatigue. Earthquake Engineering & Structural Dynamics, 21(10), 837-848.
- [10] D. T. Niu, L. J. Ren. 1996. Improved two-parameter seismic damage model for reinforced concrete structures. Earthquake Engineering and Engineering Vibration (4), 44-54. (in Chinese).

ENVIRONMENTAL LEAKAGE POLLUTIONS EVALUATIONS IN URBAN WATER DISTRIBUTION NETWORK USING UNACCOUNTED WATER PRINCIPLES (SHOKUHIEH INDUSTRIAL TOWN IN IRAN)

Siamak Boudaghpoor¹ and Saeideh Sabooteh²

1. Environmental Engineering branch, Civil Engineering Department, K.N.Toosi Technical University, Tehran, Iran, email: bodaghpoor@kntu.ac.ir
2. Department of Civil Engineering, South Tehran Branch, Islamic Azad University, Tehran, Iran

ABSTRACT

Consideration of non-revenue water in urban water distribution networks is of special importance in planning urban water distribution network and in water consumption. Water loss, especially in the distribution networks, forms a large part of the unaccounted for water (UFW). Considering the serious crisis in water resources, and taking into account the existing limitations of supplying hygienic drinking water, increasing attempts must be made at reducing the volume of water loss. The present study evaluated the environmental effects of pollution leakage from broken pipes into the water distribution network in the Shokuhieh. General principles and concepts of UFW, apparent loss was reviewed. Based on these concepts, probable pipe break points, and the resulting contaminants entering the network were considered. A software model of the water distribution network in the study area was then used to investigate qualitative and quantitative results related to intrusion of contaminants into the water distribution network and diffusion of pollutants into the network. Results of the present study and physicochemical tests performed on water revealed that BOD and COD concentrations increased from 5-10 to 10-20 mg/L and the coliform count rose from zero to 20 MPN as a result of pipe breaks in the distribution network.

KEYWORDS

Unaccounted for water, Diffusion of contaminants, Pipe breakpoints, Contamination load, the Shokuhieh Industrial Town, Environmental effects

INTRODUCTION

Urban water supply networks serve various functions the most important of which are supplying drinking water for the urban population and providing the water required for sanitary facilities such as bathrooms, toilets, etc., small and large factories and various workshops, irrigation of green spaces, street washing, public lavatories, and for the fire-department when fires break out. Urban water supply networks must be able to carry out the mentioned duties and meet the named needs, and other similar ones well, both qualitatively in accordance with present standards. It must be possible to supply the required water even under the worst temporal and spatial conditions and also under emergency conditions. The volume of UFW is



mainly used as a criterion for the efficiency of water supply systems. According to the World Bank, efficient water supply systems have UFW values of less than 15 percent. In the developing countries, 15 to 20 percent are the usual values for UFW. Water loss in water distribution networks in England, based on the characteristics, structure, and special factors governing each water distribution network, varies from 8 to 33% of the total volume of water entering these networks while the corresponding figures are 16% for the United States less than 10% for Singapore and 50 to 60% in the developing countries. In Iran, the value of UFW ranges from 20 to 50%, and it was 31.2% in 2001. Based on results obtained from study areas, the average level of UFW in Iran was 40.6% from 1997 to early 2000s, and was caused by physical and non-physical losses of 54 and 45%, respectively.

A review on unaccounted water

According to the definition by the World Bank, UFW is the difference between the net volume of water entering the network and the volume of consumed water. It must be mentioned that the concept of non-revenue water (NRW), which was introduced by the IWA, has been used as a substitute for UFW since the year 2000. In the present study the following definition relation has been used:

$$\text{UFW}_{\text{total}} = V_{\text{in}} - V_{\text{out}} \quad (1)$$

Where $\text{UFW}_{\text{total}}$ is the total UFW in an urban area, V_{in} is the measured volume of water entering the network and V_{out} known as the volume of output water measured during the same specified period. The volume of consumed water is measured by consumer gauges and output meters in the area, whether billed to consumers or not, and it specifically does not include factors such as pipe burst, illegal connections, leakage and reservoir overflow, network cleaning, broken-down meters, etc. In the above definition, leakage created after the customers gauge is not included as UFW because, if the meters are of high accuracy and sensitivity, the volume of internal leakage is calculated as a part of the customer water consumption and billed to the customer. However, if the water gauges are of low accuracy, the leakage is not included as UFW and is evaluated as gauge inaccuracy.

Relationship between pressure loss and leakage

It is known that water pressure and leakage are related in urban water supply systems. Limited field research has been done and not much experience has been gained in this regard in Iran. Theoretically, discharge through an orifice with fixed dimensions corresponds to the square root of water pressure; i.e.

$$Q = KP^{0.5} \quad (2)$$

A series of experiments has demonstrated that this relationship does not apply to the effects of water pressure on leakage in urban water distribution networks. It can be predicted that a logical pressure distribution pattern has high values at night, low values in the morning and evening, and intermediate values before noon and in the afternoon. Sometimes, pressure diagrams may not exhibit the expected changes due to errors in data and in reading manometers and because of water flow from faucets on the boundaries of the separated area and/or at locations of house connections to water transmission lines. Therefore, fluctuations in water consumption in the area along the way do not considerably affect the pressure diagrams.

Characteristics of the study area

The study area is the Shokuhieh Industrial Town in Qom province. Shokuhieh Industrial Town is located 12 kilometers of the city of Qom. Its population is 63 in 21 families and it has 1057 industrial units.



Fig. 1 – Shokuhieh industrial town's location

Besides Table 1 lists the information on pipe material, length, and diameter in the transmission lines.

Tab. 1 - Length (km) and diameter of pipes (mm) and pipe material in the transmission lines

Diameter (mm)	200	350	600
Pipe material			
Asbestos (km)	10	2	5
Steel (km)	-	-	3

The present research was based on available geographical and demographic information and other information obtained from the various departments of the Qom Water and Wastewater Company including the Company's customer service department and the departments of financial affairs, water production and utilization, and maintenance of facilities and of transmission lines. The collected statistics were confirmed and the required information was completed (Table 2). Operational measures such as meter installation at sites of water resources, network pressure assessment, gauge accuracy test using the in-situ test method, measurement of leakage at facilities and in the network using the volumetric method are taken to determine the UFW components.

The total length of the network and of the water transmission lines is 225 kilometres and the water supply is provided by seven wells in alluvial calcareous soil. A one-hectare area of the network with a length of 2046 meters was selected for the present study. Information concerning customers, accidents, and network pressure and water quality was collected, customer consumption pattern was estimated, and information concerning public and services-related water consumption was obtained to perform the analysis.

Tab. 2 - General characteristics of the study area together with lengths of the surveyed pipes

Item	Address	Pipe length (m)
1	The distance between the Moshtagh and Bahrami Streets	120
2	The distance between the Bahrami and Golzarmanesh Streets	175
3	The distance between the Golzarmanesh and Shaghayegh Streets	140
4	The distance between the Shaghayegh and Shahid Khosropour Streets	250
5	The distance between the Shahid Khosropour and Imam Khomeini Streets	230
6	The distance between the Imam Khomeini and Vahid Streets	270
7	The distance between the Vahid and Sangsar Streets	110
8	The distance between the Sangsar and Sanat Streets	180
9	The distance between the Sanat and Enghelab Streets	240
10	The distance between the Enghelab and Bahrami Streets	331
11	Total	2046

RESEARCH PROCESS

Following steps have been done and the performed analysis of the information are presented below :

- As started above, a part of the area covered by the water distribution network was selected as the pilot area for the research.
- Survey operations and leak detection were carried out by dividing the pilot area into smaller parts and through using leak detection equipment.
- Data obtained from the survey including pipe diameters and material, soil type on which the pipes were laid, water pressure inside the pipes, etc. was entered into the software system and the required information was extracted.
- After studying and comparing the software and theoretical results related to the way contamination infiltrated through the pipe breaks, the expected results were obtained.
- Physico-chemical tests were performed on water samples before and after the locations of pipe breaks and the related results were extracted.
-

Analysis of information regarding accidents

Table 3 presents information related to leak detection and accidents based on analyses performed in the pilot area. Moreover, information concerning the survey of the pilot area was studied and modelled together with the output of the LOOP software, and the results were presented.

Tab. 3 - List of locations where leaks were detected together with the lengths of the pipes

Item	Address of the location of the leaks	Pipe length (meters)	Number of leaks
1	Distance between the Moshtagh and Bahrami Streets	120	5
2	Distance between the Bahrami and Golzarmanesh Streets	175	3
3	Distance between the Golzarmanesh and Shaghayegh Streets	140	2
4	Distance between the Shaghayegh and Shahid Khosropour Streets	250	6
5	Distance between the Shahid Khosropour and Imam Khomeini Streets	230	5
6	Distance between the Imam Khomeini and Vahid Streets	270	8
7	Distance between the Vahid and Sangsar Streets	110	5
8	Distance between the Sangsar and Sanat Streets	180	8
9	Distance between the Sanat and Enghelab Streets	240	3
10	Distance between the Enghelab and Bahrami Streets	331	10
11	Total	2046	55

Figures 2, 3, 4 and 5 indicate accidents in the mentioned water supply network based on obtained information. As shown in these figures, the majority of accidents happened at connection sites followed by those that occurred inside the network, while a negligible percentage was caused by other factors.

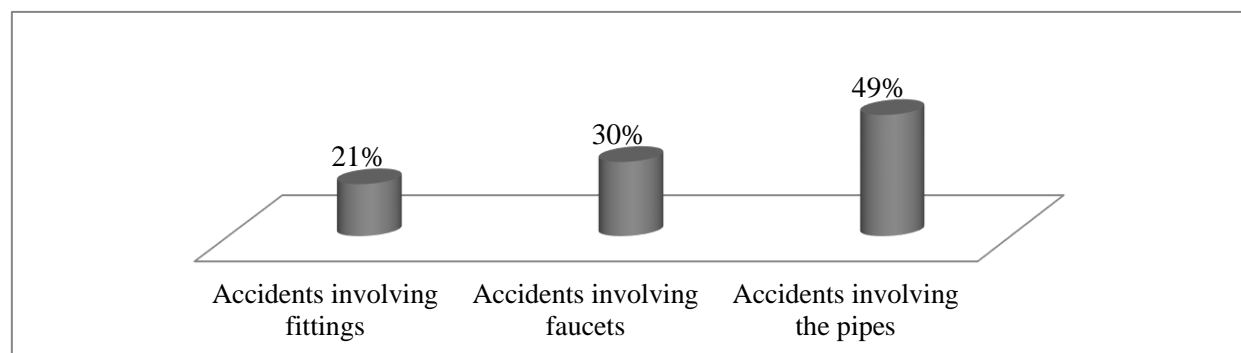


Fig. 2 – Various equipment responsible for accidents that happened in the water supply network

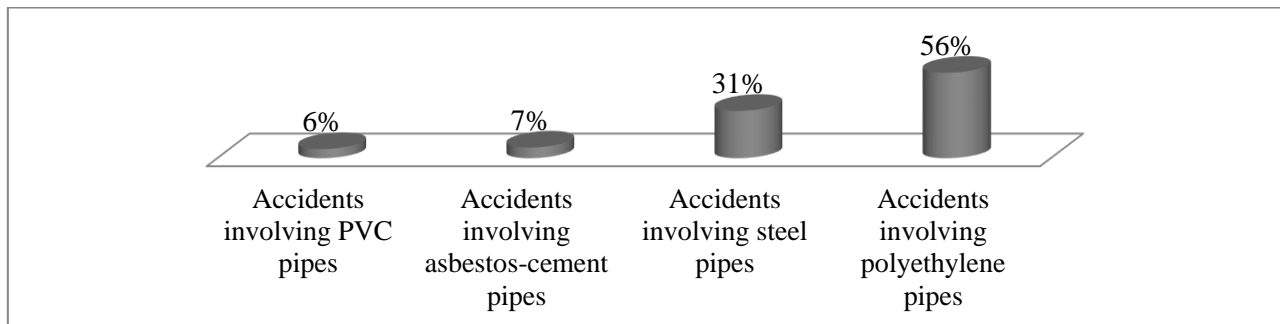


Fig. 3 – Various types of pipes involved in accidents in the water supply network

Moreover, accidents involving connection sites were mainly caused by breaks and rupture. Study of the reasons for these accidents revealed that they were mainly due to external loads. Of course, low quality of the pipes was one of the main causes of accidents that happened at connection sites.

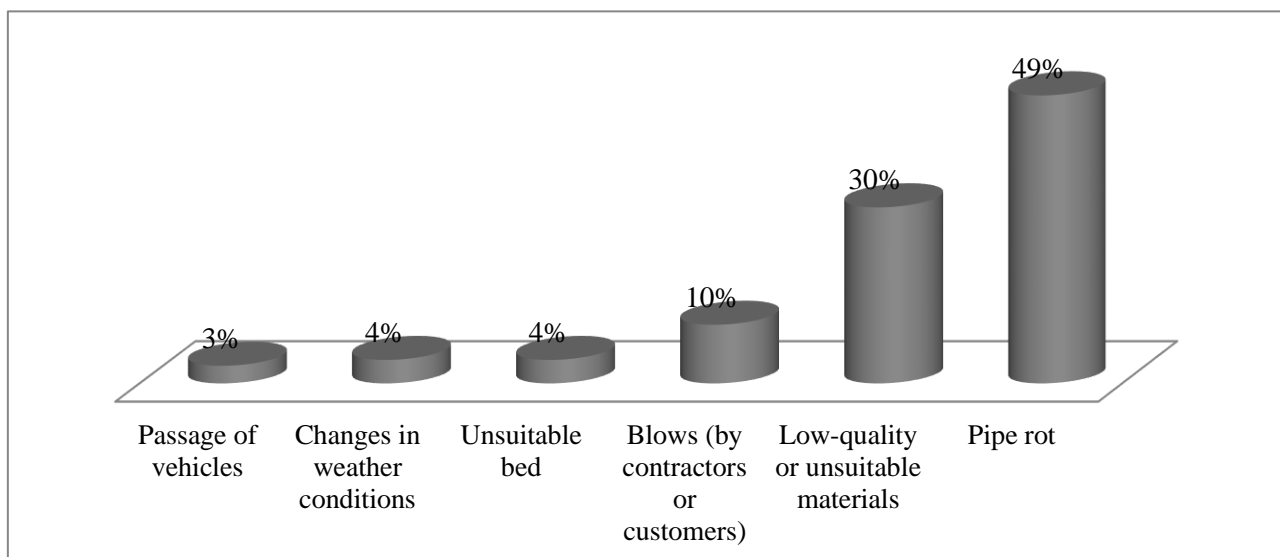


Fig. 4 – Various reasons for accidents that happened in the water distribution network

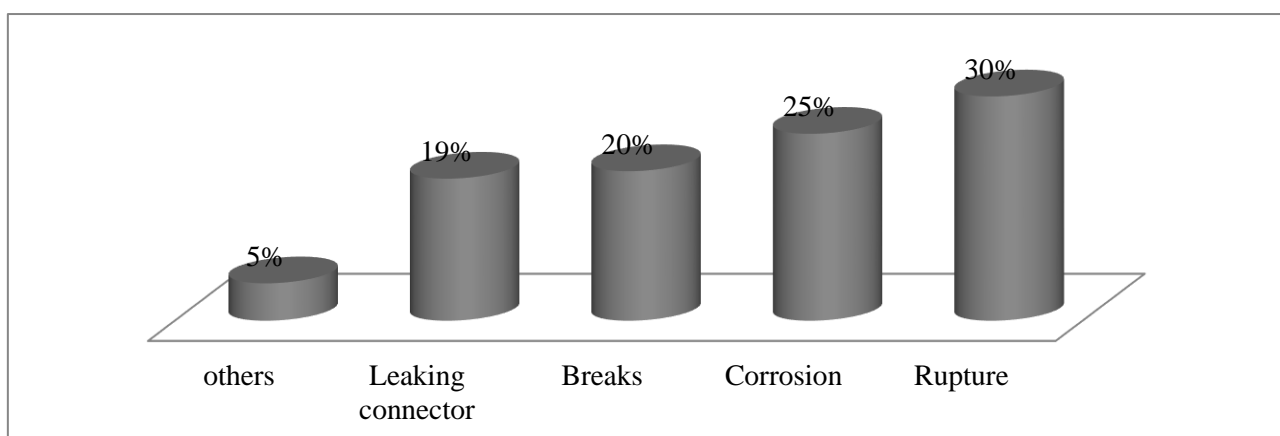


Fig. 5 – The various accidents that happened in the water distribution network

RESULTS AND DISCUSSIONS

Output results were studied by placing the information in Table 3 including pipe diameters and routes and division of the network in the various nodes. The output results included the following:

- Pressure surges followed by breaks were created at some places in the studied area due to the unsuitable design.
- Pressure drop occurred at locations with invisible leak and resulted in generation of negative pressure.
- Suction was created where negative pressure or negative flow existed. Consequently, contamination infiltrated into the pipes from the surrounding area and affected the customers.
- After physical and chemical tests were performed on the water samples, the final results of these breaks and the resultant contamination infiltration were determined.

Effects of pollution diffusion due to pipe breaks

After pipe breaks, while the operational teams are solving the problem and/or when there are invisible leaks, contamination present in the soil infiltrates into the water distribution network through the broken pipes. This pollution can include various types of viral and microbial infections including fecal and non-fecal coliforms. The present research showed that pipe breaks and the consequent leakage were unavoidable due to the lack of pressure management in the water distribution network, aged and rusted components in the water distribution network, and incorrect pipe laying likely unsuitable fill, material, and equipment used in filling, unsuitable frost depth, low-quality pipes, sediments in water pipes followed by their clogging and generation of additional pressure in other places, non-compliance with determined traffic load. Moreover, because of unsuitable design of networks in some places including improper design of fittings and knees, and lack of attention to regulations for designing and implementing urban water distribution networks including uniform pressure distribution and prevention of pressure drop in some areas, longitudinal supports along pipe routes. When pipe breaks happened and pressure drop known as a negative pressure occurred, suction was created in the broken segment of the pipe. This suction influenced infiltration and spread of contaminants.

Furthermore, since integrated urban wastewater systems have not entered into the operational phases in most Iranian cities, especially in Tehran, and traditional wastewater disposal using absorbing wells is used, this type of waste disposal continuously contaminates soil with organic and mineral matter mostly nitrogen and phosphorous present in the wastewater. In addition, if standard wastewater methods are not employed, the wastewater also includes fecal and non-fecal coliforms that cause digestive and intestinal problems. It should be mentioned that, depending on soil texture and topographic conditions in the soil in the absorbing wells can be saturated after some time and cannot be able to absorb salts, bacteria, etc. Therefore, these contaminants can remain in the soil and, after pipe breaks occur, enter the distribution network and are directly introduced into the water consumption cycle.

Since this type of contamination enters the described cycle after preliminary and final water treatment processes are carried out, no measure can be taken to control it. Therefore, the related Water and Wastewater Companies must study the different areas covered by them to determine the total UFW and its components. This process was carried out thoroughly in the present research. The mentioned companies can then use the methods described in the present research to investigate how the leakage and pipe breaks occurred in areas where they were likely to happen and to take the necessary remedial measures.

In addition, after the pipe break was fixed by the operational team, several random water samples were taken from various faucets that were closest to the point of pipe break at a distance of one meter from it in the control area. Random samples from the area were taken for the duration of one month and the parameters of interest in the physicochemical analysis of the water, including $(BOD)_5$, (COD), TDS, heavy metals, and fecal coliforms, were measured in Tables 4 and 5.

Tab. 4 - Results of physicochemical analysis of water samples taken at spots one meter before the point the pipe break happened (after disinfection and sterilization)

Item	Test	Average measurement	Number of measurements	
1	Biological oxygen demand ($BOD)_5$	5 ppm	20	Standard level
2	Chemical oxygen demand (COD)	10 ppm	20	Standard level
3	Total dissolved solids (TDS)	450ppm	20	Higher than the standard level
4	Fecal and non-fecal coliform bacteria	Zero	20	Standard level

Tab. 5 - Results of physicochemical analysis on water samples taken from various faucets one meter from the pipe break in the control area and from spots close to the point of pipe break

Item	Test	Average measurement	Number of measurements	
1	Biological oxygen demand ($BOD)_5$	10 ppm	20	Higher than the standard level
2	Chemical oxygen demand (COD)	20 ppm	20	Higher than the standard level
3	Total dissolved solids (TDS)	780 ppm	20	Higher than the standard level
4	Fecal and non-fecal coliform bacteria	20 MPN	20	Higher than the standard level
5	Heavy metals (lead)	0.05 ppm	20	Higher than the standard level

Results of the tests show that the required water entering the network after preliminary treatment operations, which include infiltration, sedimentation, and use of chemicals, satisfied the necessary standards and could be used as drinking water. However, it seems that in various parts of the network where visible and invisible pipe breaks had happened and had caused water loss in the network, existing soil contaminants infiltrated into the network and caused problems for customers. According to present study Figure 6 shows the diffusion of various pollutions in water distribution network in Shokuhieh industrial town.



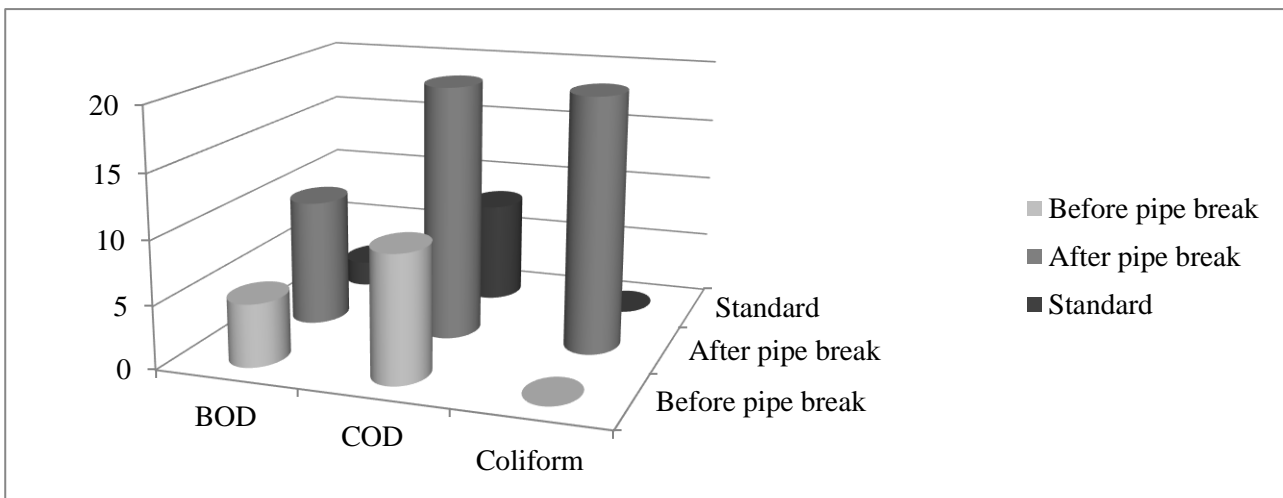


Fig. 6 - Diagram of pollution diffusion in the water distribution network

CONCLUSIONS

According to present study following results have been achieved:

- The guidelines offered in the present research should be used for pressure management and for prevention of intolerable pressure build up that causes pipe breaks.
- In the areas where conventional wastewater disposal method with adsorbing wells is still used, infiltration of wastewater from the lower lays and scour below the pipelines because of using low quality material and due to non-compliance with regulations related to pipe laying caused the maximum number of pipe breaks in the distribution mains that were often located within an 80-meter diameter from the wastewater well.
- Within a distance of one meter from the point where a pipe break happened in the study area, it was unfortunately observed that the wastewater main pipe passed from the vicinity of an old well. The pipe break was fixed within 48 hours. Moreover, a sample of the soil near the pipe break was personally and secretly taken by the author and transferred to the soil laboratory where physicochemical tests were performed to determine its phosphorous, nitrogen, free chlorine, and bacteria contents. It was found that the soil was saturated with these contaminants and these salts could be used as agricultural fertilizers.
- Tests were also carried out to determine fecal coliform count, and results showed it was far greater than the standard one and reached about 20 MPN, while it should be zero in drinking water. In the long-term, these bacteria cause digestive and intestinal problems.
- Furthermore, as mentioned before, it was observed that at some locations where pipe breaks happened, because the pipes were aged and their installation regulations were not followed, fake fittings and flanges had been used. The alloys used in these fittings also contained heavy metals that dissolve in water over time and enter the bodies of the customers.

REFERENCES

- [1] Beiges, F. (1999). "Pathology of the urban water distribution networks". *Journal of Water and Environment*, 78(37), 17-25.
- [2] Bernardes, E.S., and Hanna, M.D. (2009). "A theoretical review of flexibility, agility and responsiveness in the operations management literature toward a conceptual definition of customer responsiveness". *International Journal of Operations and Production Management*, 29, 30-53.
- [3] Brown, R.R., Keath, N., and Wong, T.H.F. (2009). "Urban water management in cities: historical, current and future regimes". *Water Science and Technology*, 59(5), 847-855.

- [4] Cettner, A., Ashley, R., Hedström, A., and Viklander, M. (2014). "Assessing receptivity for change in urban stormwater management and contexts for action". *Journal of Environmental Management*, 146, 29-41.
- [5] Dunn, G., Brown, R.R., Bos, J.J., and Bakker, K. (2016). "Standing on the shoulders of the giants: understanding changes in urban water practices through the lens of complexity sciences". *Urban Water Journal*, 14(7), 758-767.
- [6] Koste, L.L., and Malhotra, M.K. (1999). "A theoretical framework for analyzing the dimensions of manufacturing flexibility". *Journal of Operations Management*, 18(1), 75-93.
- [7] Pathirana, A., Radhakrishnan, M., Quan, N.H., and Zevenbergen, C. (2017). "Managing urban water systems with significant adaptation deficits—unified framework for secondary cities: part I—conceptual framework". *Climate Change*, 1-14.
- [8] Poustie, M.S., Frantzeskaki, N., and Brown, R.R. (2016). "A transition scenario for leapfrogging to a sustainable urban water future in Port Vila, Vanuatu". *Technological Forecasting and Social Change*, 105, 129-139.
- [9] Rogers, C.D., Lombardi, D.R., Leach, J.M., and Cooper, R. (2012). "The urban futures methodology applied to urban regeneration". *Proceedings of ICE Engineering Sustainability*, 165(1), 5-20.
- [10] Spiller, M., Vreeburg, J.H.G., Leusbroek, I., and Zeeman, G. (2015). "Flexible design in water and wastewater engineering—definitions, literature and decision guide". *Journal of Environmental Management*, 149, 271-281

FIELD LOADING-TEST BASED SHM SYSTEM SAFETY STANDARD DETERMINATION

Jiaping Yu^{1,2}, Chunwei Li¹, Quansheng Sun¹

1. Northeast Forestry University, Department of Civil Engineering, 26 Hexing road, Harbin, PR China; lichunwei@nefu.edu.cn, hrbsqs@126.com.
2. Beijing Jiaotong University, School of Civil Engineering, 3 Shangyuancun road, Beijing, PR China; Jiapinguo@bjtu.edu.cn.

ABSTRACT

Structural health monitoring (SHM) allows for real-time structural response monitoring and online data acquisition of bridge structures. This data reflects the operational and environmental conditions of the bridge, which is important in identification of possible anomalous changes. In order to effortlessly determine the safety condition of the bridge directly through the transferred data without data analysis, a five-level safety standard system will be established for real-time safety warning in this paper. The threshold of each safety levels will be determined through field loading tests results on an external prestressing rehabilitated continuous rigid frame bridge, of which permanent structural health monitoring system was instrumented. After overall evaluation, we come to the conclusion that the rehabilitation is successful and that the bridge is under safe operating condition. A novel, simplified safety standard thresholding technique is proposed based on static loading test results as well as ultimate limit state of the bridge. This technique is simple yet very practical in daily bridge monitoring.

KEYWORDS

Structural health monitoring, Continuous rigid frame bridge, field loading test, Bridge rehabilitation, External prestressing, Safety standard thresholding

INTRODUCTION

Structural health monitoring (SHM), an extension of traditional non-destructive testing (NDE) method for civil structures, which implement permanent sensors into structural components and monitors structural response continuously. SHM are becoming an indispensable systems of modern long-span bridges [1-3]. The monitored data provides information, scientific basis and performance status for bridge structural design, construction, daily maintenance, as well as decision making. While most health monitoring systems are installed on newly constructed bridges, rehabilitated bridges are rarely being monitored, not to mention external prestressing strengthened continuous



rigid frame bridges. The difference in structural responses of the bridge before and after the rehabilitation needs to be considered in SHM.

An incorrect evaluation of bridge behaviours may result in not only on financial losses but also on the safety of traffic and pedestrians. Dynamic responses and modal analysis have been extensively studied in order to extract structural information from the monitored data [4]. However, damage detection models currently used have their limitations and shortcomings in the real-world [5]. In this context, bridge field testing has become a powerful mean of obtaining quantifiable information, complementary to the numerical analysis and monitored data, for the assessment of structural behaviour and identification of its actual operating condition [6]. Static loading tests are routine protocol in the final stages of a bridge construction acceptance check [7]. In this paper, a combination of readily available static field loading test results, and finite element simulation will be investigated in the evaluation of a rehabilitated continuous rigid frame bridge. Furthermore, a novel, simplified safety standard thresholding technique is proposed based on static loading test results as well as ultimate limit state of the bridge.

BACKGROUND

The rehabilitated highway bridge located in the northeast region of China, a total length of 549.36m, and a total width of 24.5m. Span arrangement is 75m+3x130m+75m. North to south travel direction from Xing Mountain to Province boarder was of interest in this study, which is 12m in width with 2 traffic lanes.

The bridge was first opened to traffic in 2006. However, after as little as 6 years of operation, the bridge showed signs of deterioration and decreased bearing capacity. During routine inspection in years 2012, 2013 and 2015, cracks were observed on the top slab, web and bottom slab, more severe on the exterior surfaces than the interior. Length, width and number of cracks were growing as time progresses. The width of some longitudinal cracks on the box girder exceeds limit value in the Chinese design code [8].



Fig. 1 – General view of the rehabilitated highway bridge

External prestressing strands were anchored on the inner surface of the box girder, 8 external tendons (Figure 2a) for each span. Steel plates of grade Q235C steel [9] were pasted on the interior surface of the girder on the top, bottom, web plate surfaces (Figure 2b) and on the exterior bottom

surface (Figure 2c). Sizes of the steel plates are 60mm wide and 6mm thick, length depends on the height of the web, 150mm plate spacing on the inside and 200mm on the outside.



Fig. 2 – Strengthening of the highway bridge: a) external prestressing, b) steel plates inside the girder, c) steel plates outside the girder.

METHODS

Finite element modelling

Finite element modelling of the entire bridge structure used Midas/Civil finite element software. A total of 300 elements and 325 nodes, of which the bridge deck consists of 154 elements and 155 nodes, piers consist of 146 elements and 170 nodes. Piers and bridge deck are rigidly connected. Bridge abutments were vertically supported. Calculations were made based on Chinese code JTGD62-2004 “Code for design of highway reinforced concrete and prestressed concrete bridges and culverts” [8]. Structural concretes are cast in-situ. 61 construction stages were used in order to simulate cantilever on-site concrete casting and other major rehabilitation stages. Finite Element model is shown in Figure 3 and Figure 4.

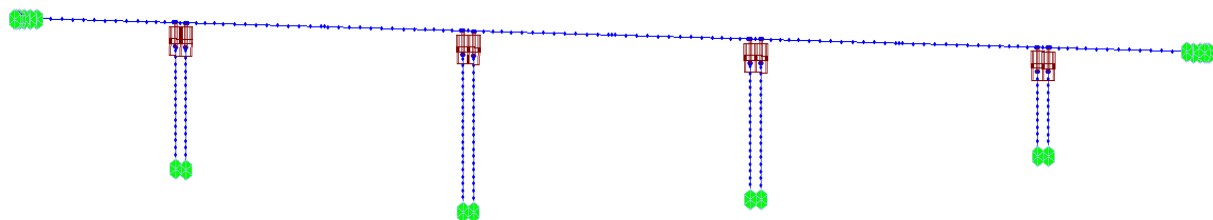


Fig. 3 – MIDAS Discrete element model

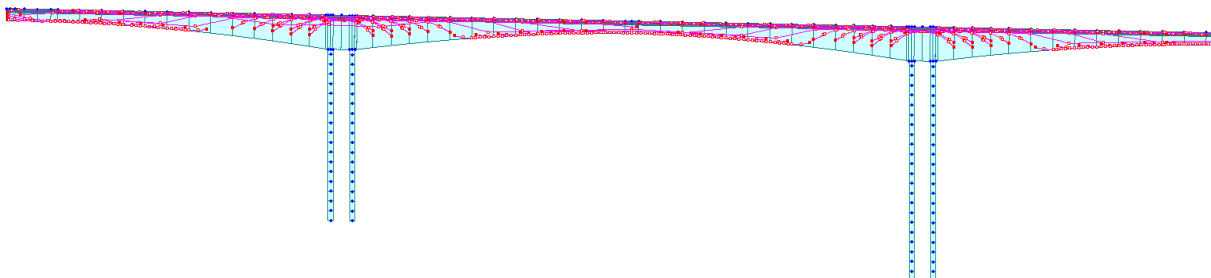


Fig. 4 – MIDAS External prestressing tendon model

Load combinations

Total of four load combinations were used to simulate serviceability limit state and ultimate limit state. Load combinations details are shown in Table 1.

Tab. 1. - Load combinations

No.	Load	Phase	Load Combination Description
Basic Combination :			
1	cLCB1	Ultimate	1.2 (cD) +1.2 (cTS) +1.0 (cCR) +1.0 (cSH) +1.4M+1.12TPG
Standard Combination :			
2	cLCB2	Serviceability	1.0 (cD) +1.0 (cTP) +1.0 (cTS) +1.0 (cCR) +1.0 (cSH) +1.0M+1.0TPG
Short term Combination :			
3	cLCB3	Serviceability	1.0 (cD) +1.0 (cTP) +1.0 (cTS) +1.0 (cCR) +1.0 (cSH) +0.7M+0.8TPG
Long Term Combination :			
4	cLCB4	Serviceability	1.0 (cD) +1.0 (cTP) +1.0 (cTS) +1.0 (cCR) +1.0 (cSH) +0.4M+0.8TPG

Note: cD is dead load, cTP is first stretching, cTS is second stretching, cCR is second creep, cSH is second shrinkage, M is live load, TPG is temperature load. Compressive stress adopts positive value, whereas, flexural stress adopts negative value.

Key sections

In order to accurately simulate deflection and stress of the girder under all working conditions, key sections are selected for model calculation and analysis: at bridge abutment, on top of piers, quarter span, half span, three quarter span positions, total of 21 key sections. Direction of travel is from Xing Mountain to the province boarder. Since the bridge is globally symmetrical structure, only 11 key sections will be analysed in numerical simulation model. They are 1/4, 1/2, 3/4 of the first 2 spans, 1/4, 1/2 of span 3, abutment, and pier 1 and pier 2 midline sections.

SHM instrumentation

Based on the characteristics of the rehabilitated bridge, damage sensitive parameter such as bridge deck curvature and structural mechanics behaviours are the main objectives of this instrumentation design.

The SHM system consists of two major components, the DA system and sensors. The DA system includes a centralized data acquisition module, general data acquisition module, solar power, sim card and signal emitter, and the sensor network includes strain gauges, pressure cells, and tiltmeters. These sensors are responsible for the measurements of strain, deflection and tension of the external tendons.

Overall set-up of the three different types of sensors, strain gauges, pressure cells, and tiltmeters, are shown in Figure 5, a total of 14 sensors were instrumented.

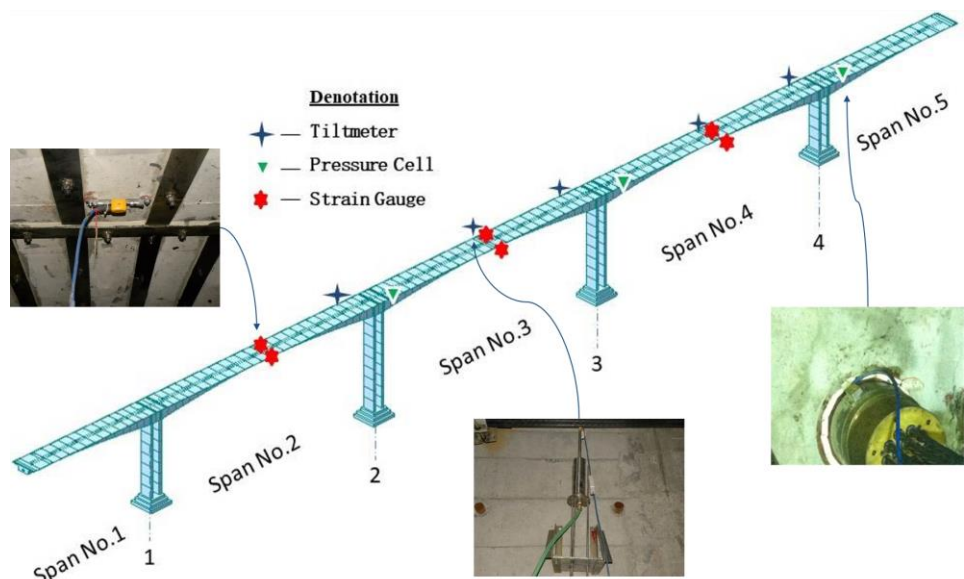


Fig. 5 – Illustration of overall sensor locations

Static loading test

The rehabilitated 5 span continuous rigid frame bridge, spans 75m+3×130m+75m, was designed for a live load of 360 kN (according to Chinese design code JTG D62-2004[8], which is similar to AASHTO HS15 loading in the American bridge design code[10]). Static loading tests were performed to obtain structural behaviour of the bridge before and after strengthening as shown in Figure 6. The main objectives of the static loading test were to test the following:

1. Strain near a support bearing;
2. Maximum strain of end and middle spans;
3. Maximum deflection of end and middle spans.



Fig. 6 – Illustration of a) eccentric static loading tests performed before rehabilitation, and b) centric static loading tests performed (b) after rehabilitation

Total of 16 3-axle trucks were used for static loading test, 8 in loading tests before strengthening and 8 after. Average weight of the trucks is 368.4kN.

Total of 14 loading conditions. Centric and eccentric loading tests were each performed on span 1~5 midspan and on pier 3 and 4 locations. Maximum bending moment at each cross-section was measured before and after strengthening. Loading trucks positions were carefully arranged so that they simulate Grade-I load level as specified in the Chinese design code [8].

RESULTS

Numerical simulation

Based on Chinese code JTG D62-2004[8], upper plate and lower plate normal stress and principle compressive stress are calculated under standard combination. Principle tensile stresses are calculated under short term combination, also, long term growth factor $\eta_{\theta}=1.475$ is considered. At the same time, deflection value minus the influence of dead weight was calculated for all the key sections. Results are shown in Table 2.

Tab. 2. - Structural behaviours of the box birder beam

Key section Location	Stress/MPa					Deflection/ mm
	Upper Plate Compressive Stress	Lower Plate Compressive Stress	Principle compressive stress	Principle tensile stress		
Abutment	0.38	4.28	4.28	-0.26		0
1/4 Span 1	6.95	8.36	8.49	-0.09		-19.59
1/2 Span 1	5.34	10.09	10.68	-0.52		-23.27
3/4 Span 1	4.53	9.47	9.58	-0.21		-14.06
Pier 1 Midline	6.07	10.27	10.29	-0.57		-0.65
1/4 Span 2	6.31	9.04	11.22	-0.97		-61.24
1/2 Span 2	11.39	2.98	11.43	-0.08		-75.61
3/4 Span 2	6.36	9.77	11.62	-0.87		-41.74
Pier 2 Midline	5.61	10.89	11.06	-0.10		-1.37
1/4 Span 3	5.81	9.58	11.15	-1.07		-42.13
1/2 Span 3	10.92	4.32	10.97	-0.08		-59.05

Based on Table 2 and Figures 7~9, all cross-sections are under compressive state. Maximum cross-sectional upperbound compressive stress of each span occurred near mid-spans. Maximum cross-sectional lowerbound compressive stress occurred within quarter-span to pier. Maximum tensile stress of each span occurred near quarter or three quarter cross-sections.

Key section midspan upperbound and lowerbound maximum compressive stresses are 11.39MPa and 10.89MPa, respectively. Lower than threshold value of $0.5f_{ck} = 16.2\text{MPa}$, which is the requirement for type A structural components indicated in the code of JTGD62-2004. Maximum midspan key section principle compressive stress is 11.62MPa, which is lower than $0.6f_{ck} = 19.44\text{Mpa}$ that indicated in the JTGD62-2004 code. Maximum tensile stress appeared near quarter span is -1.07Mpa, which is also less than $0.5f_{tk} = 1.33\text{Mpa}$ that indicated in the JTGD62-2004 code.

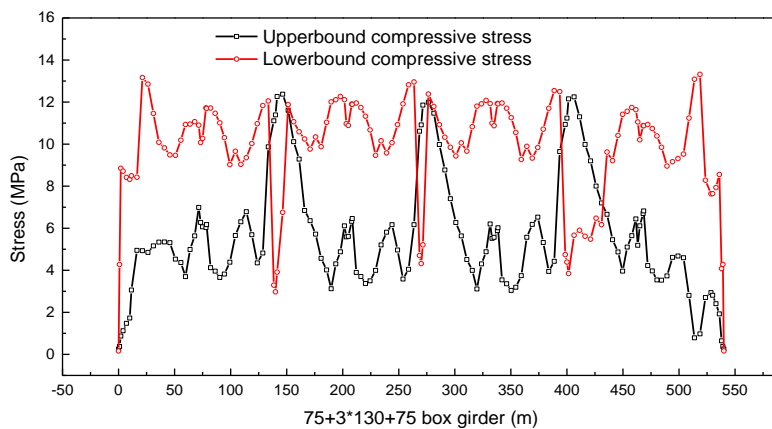


Fig. 7 – Upperbound and lower bound compressive stress

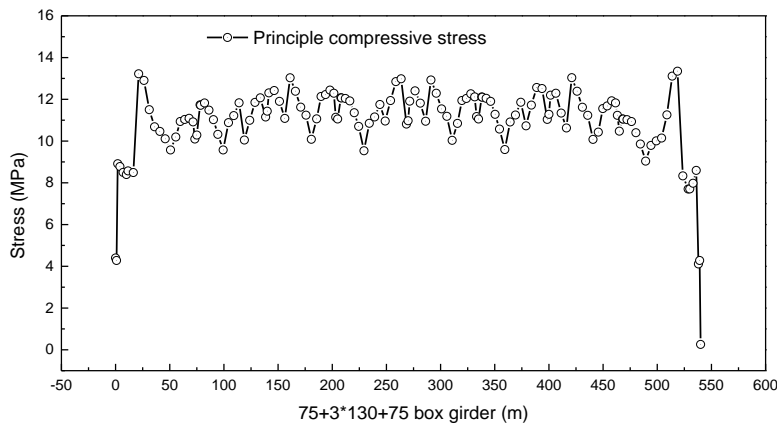


Fig. 8 – Box girder principle compressive stress

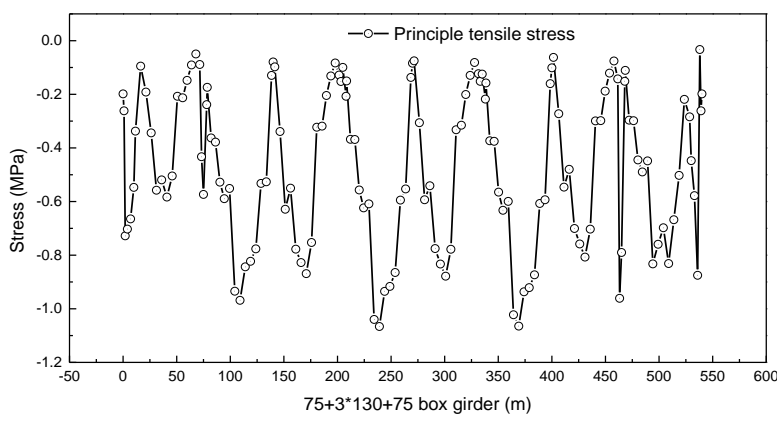


Fig. 9 – Box girder principle tensile stress

Midspan area of side spans and end spans are closing sections during concrete casting. Therefore, half span deflection value is the maximum deflection value of the key sections. For end spans, maximum deflection value is 19.59mm, smaller than threshold deflection value $L/600=125\text{mm}$ that indicated in the code. For side span and midspans, maximum deflection values are 75.61mm, 59.05mm, which are smaller than $L/600=216.7\text{mm}$ indicated in the code. Therefore,



the rehabilitated bridge complies with the Grade-I load design requirements specified in the JTGD62-2004 code, which also indicated that the strengthening technique was a success.

Deflection under static loading

Deflection value reflects the overall toughness of the structure, a key control parameter in load testing. Deflection measurement point was placed at theoretically maximum bending moment. Deflection measurement points 1, 2 and 3 were at the top plate of the girders as shown in Figure 10.

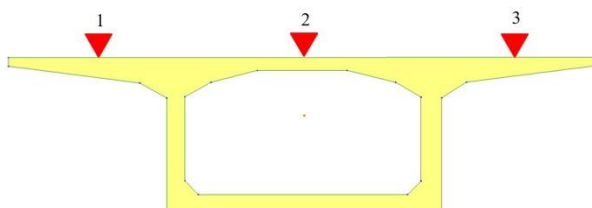


Fig. 10 – Cross-section view of deflection measurement locations

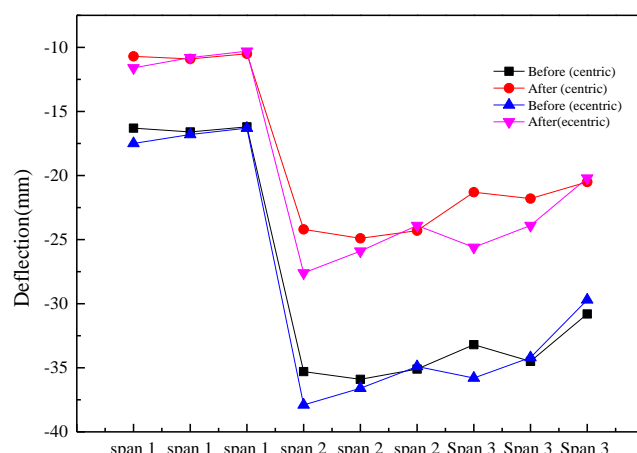
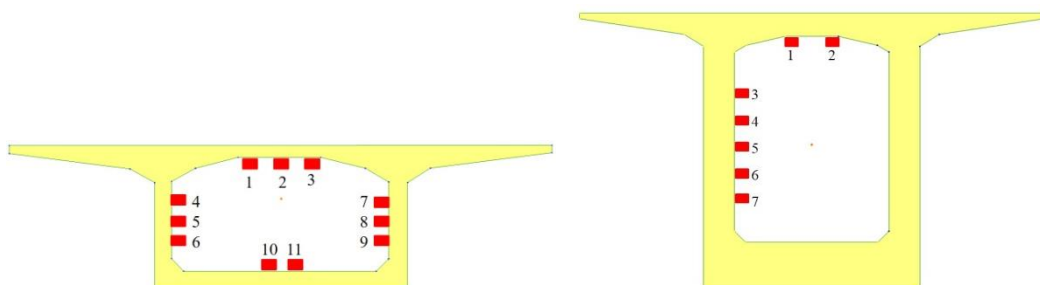


Fig. 11 – Measured vertical displacement curve

Measured vertical displacement results before and after strengthening are shown in Figure 11. Measured deflection values are all smaller than that of before rehabilitation. The maximum displacement after the strengthening decreased to 27.6mm, compared to 37.9mm before strengthening, which is a 27% improvement. For span No. 1, the bearing capacity has increased by 18.2%; for span No.2, the bearing capacity has increased by 17.5%; for span No.3, the bearing capacity increased by 19.7%. This shows that external prestressing can significantly improve the performance of the structure. However, due to prestress loss caused by construction, the actual improvement is less than theoretical calculated improvement value.

Strain under static loading

Due to difference in structural mechanics of midspan and sections near the piers, strain measurement points of the midspan cross-section is shown in the Figure 12(a) and strain measurement points of pier top is shown in Figure 12(b) below.



(a) Midspan strain gauges

(b) Pier top strain gauges

Fig. 12 – Strain measurement locations during load tests

Strain data under static loading tests results are compared with the static loading test results carried out before the rehabilitation, results for span 1~3 are shown in Figure 13 and for pier 2 are shown in Figure 14.

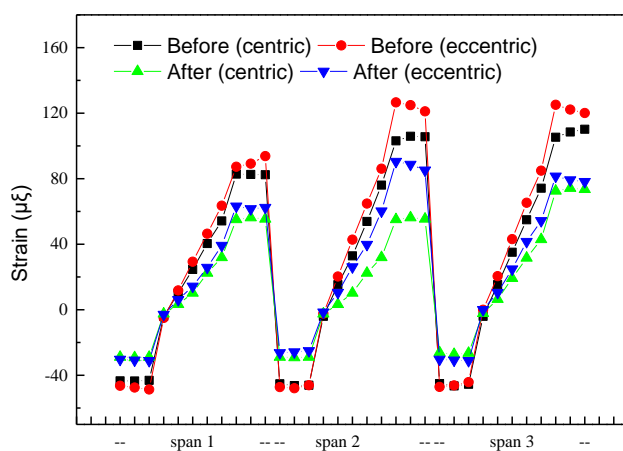


Fig. 13 – Measured strain data under static loading tests

Span 1 measured strain values of each load cases all showed improvement after strengthening. Strain verification coefficient is between 0.66 and 0.75, which indicated stiffness improvement of the structure. On average, load carrying capacity and verification coefficient increased by 28% and 27%, respectively. For span No.2, the strain verification coefficient is between 0.57 and 0.79. The load carrying capacity increased by 26% on average and the verification coefficient increased by 27% on average. For span No. 3, verification coefficient is between 0.57 and 0.76. Midspan centric loading showed an average increase of 27% on strain, verification coefficient showed an average increase of 27%. Eccentric loading improved by an average of 23%, the verification coefficient on average increased 24%.

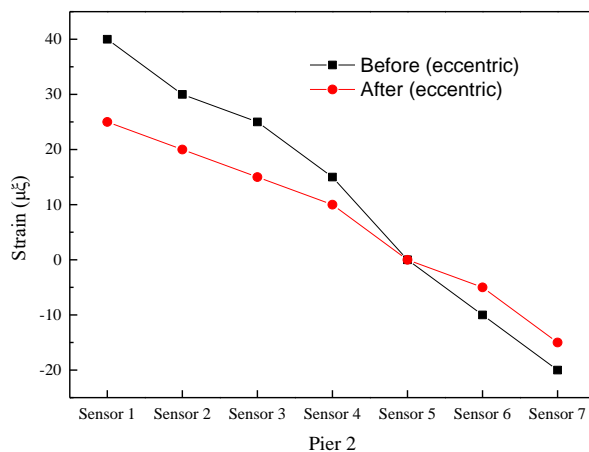


Fig. 14 – Measured strain data under static loading tests

At pier 2, bearing capacity increased by 15%, and verification coefficient increased by 18%.

After strengthening the deteriorated bridge, the measured strain values under static loading tests at each span are all less than the values before strengthening. The bridge structure showed significant improvement entirely on stiffness as well as bearing capacity. Therefore, the external prestress reinforcement method not only can effectively improve the structural behaviour of the bridge but also able to enhance the strength and safety reserve of the bridge at the same time.

Thresholding of safety standards

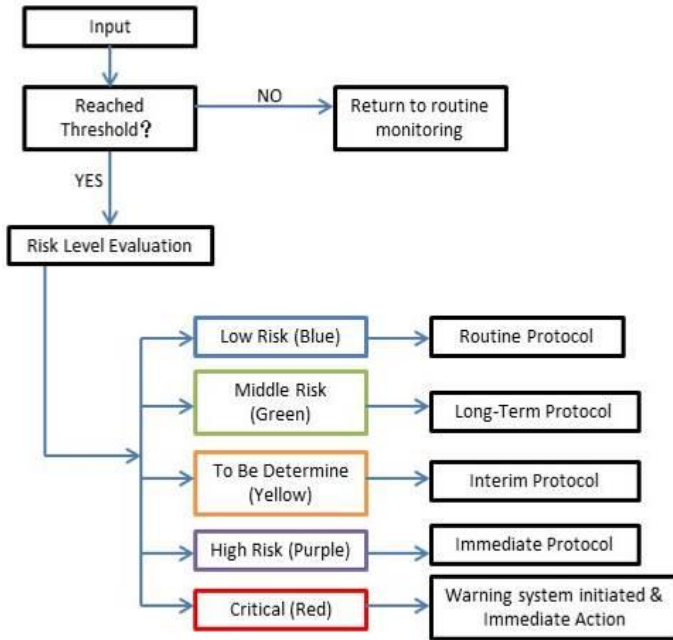


Fig. 15 – Flowchart of threshold safety standard

Safety standard for bridges utilize relevant information, analyses the safety of the structure, set grounds for further management and decision making [11]. For the numerous amount of data

archived, a preliminary determination of the state of data is developed. As shown in Figure 15, warning alert of different colour will be triggered if the transferred data was evaluated to be over the safety value. Instead of using characteristic value of an action, quasi-permanent value of a variable action, as well as representative value of an action, a new method of safety thresholding based on experimental static loading test is proposed.

After data input, i.e. received by the user end, an automatic evaluation will determine if the data reached safety threshold. If the answer is no, then the data will be archived without any warning alert. This indicates that the bridge structure is under stable and safe operation. If the data indeed reached threshold level, a classification of the risk level will begin. Moreover, each risk level has its associated action protocol.

At low risk, with the colour blue, will initiate routine protocol. This means that the bridge structure is under safe operation that no over-limit response detected. But maybe further attention is needed. A scheduled inspection team will be sent on-site to visually check for anomalies. Repair would most likely be unnecessary.

At middle risk with a green colour, the bridge structure is still under safe and stable operation. If visual inspection cannot detect any anomalies, technical equipment will be used to evaluate the condition. Note that in this level, over-limit response will not detect either and no reduction of bearing capacity has occurred. However, small repairs may be needed in this risk level.

At to be determine risk level, the bridge structure may experience heavy load trucks that may pose threats to safe and stable performance. The structure probably has more than one small defects and the bearing capacity has been reduced by less than 10%. After on-site inspection and restrictions of traffic, decision has to be made carefully whether to retrofit the structure or to re-open traffic with certain restrictions.

At high risk level, purple colour alert will initiate, immediate shut down of traffic is required to prevent any catastrophe. At the same time, an inspection team will be sent out to evaluate the exact situation. A crack that exceeds the limit is probably present. Rehabilitation plan or entire replacement of the bridge will be put on schedule. Bearing capacity has been reduced by 10~25% of the design value.

At the critical level, with colour red, the bridge is at its critical state and may experience failure at any moment. Close off of the traffic will be mandatory. Bearing capacity has been reduced to 25% of the design value.

A flowchart summary of the warning process and protocol is shown in Figure 15 above.

Before the system can automatically classify safety levels, warning thresholds have to be determined manually. Universal algorithm for warning thresholds determination has not been discovered. There are many obstacles in the development of the algorithm. Each and every single bridge has its own characteristics. Different bridge structural type, different environmental conditions, different material composition and different sizes of the structural components will all result in different warning threshold values.

However, based on the initial readings of the instrumented sensors, calculated or tested threshold can be verified. Through theoretical calculation and static loading tests, warning threshold of different warning levels can be observed. Maximum deflection and strain values of the midspan static load test are shown in Table 3.

Tab. 3. - Maximum static load tests structural response values of midspans

Location.	Maximum Deflection (mm)	Maximum Strain of Top Plate ($\mu\epsilon$)	Maximum Strain of Bottom Plate ($\mu\epsilon$)
Span 1	11	-33	56
Span 2	27	-60	58
Span 3	25	-60	59
Span 4	25	-59	60
Span 5	11	-30	54

Ps: (+) for compressive stress, (-) for tensile stress

Maximum strains of the cross-section on top of the piers are shown in Table 4 below

Tab. 4. - Maximum static load test structural response values of the piers

Location.	Maximum Strain of Top Plate ($\mu\epsilon$)	Maximum Strain of the Web ($\mu\epsilon$)
Pier 3	60	65
Pier 4	55	55

High risk level for deflection of each midspan is the experimental values of the static load tests and the critical value is based on the calculated ultimate limit state. All the other levels are based on 0.95, 0.9 and 0.8 reduction coefficients of the maximum static load test values. Detailed values for each warning level thresholds are shown in Table 5.

Tab. 5 - Deflection values of midspans warning risk levels (Unit: mm)

Colour Location	Blue	Green	Yellow	Purple	Red
Span 1	9.35	9.9	10.5	11.0	23.27
Span 2	22.95	24.3	25.7	27.0	41.74
Span 3	21.25	22.5	23.7	25.0	59.05
Span 4	21.25	22.5	23.7	25.0	41.74
Span 5	9.35	9.9	10.5	11.0	23.27



Strain values of the high risk level are based on maximum static loading test values, and critical risk level strains are based on calculated ultimate limit state. All the other warning levels, similar as deflection warning levels, are also based on 0.95, 0.9 and 0.8 reduction coefficients of the maximum static load test values.

Tab. 6 - Strain of top and bottom plate warning risk levels (unit: $\mu\epsilon$)

Colour Location \	Blue	Green	Yellow	Purple	Red
Span 1 Top	28.05	29.7	31.4	33	39.6
Span 2 Top	51	54	57	60	72
Span 3 Top	51	54	57	60	72
Span 4 Top	50.15	53.1	56	59	70.8
Span 5 Top	25.5	27	28.5	30	36
Span 1 Bottom	47.6	50.4	53.2	56	67.2
Span 2 Bottom	49.3	52.2	55.1	58	69.6
Span 3 Bottom	50.15	53.1	56.05	59	70.8
Span 4 Bottom	51	54	57	60	72
Span 5 Bottom	45.9	48.6	51.3	54	64.8
On top of Pier 3	51	54	57	60	72
On top of Pier 4	46.75	49.5	52.3	55	66
Pier 3 web	55.25	58.5	61.7	65	78
Pier 4 web	46.75	49.5	52.3	55	66

Detailed threshold strain levels of the top plate and bottom plate of the box girder, top plate of the cross-section on top of the piers, and web of the cross-section on top of the piers are shown in Table 6. For external prestressing, they are stretched at 930kN, thus their tension forces are 1953kN in total for each bundle. Warning thresholds for tension forces of each level are shown in Table 13 below.

Tab. 12 - Tension force warning risk levels (unit: kN)

Colour Location \	Blue	Green	Yellow	Purple	Red
Span 3	1953	1774	1685	1597	1419
Span 4	1953	1570	1491	1532	1256
Span 5	1953	1712	1626	1541	1370

After the elimination of outliers, no over-threshold values were observed. Once again, verified that the rehabilitated bridge is operating under normal condition.



CONCLUSION

Due to decreased bearing capacity, symptoms such as cracks and increased midspan deflection, the continuous rigid frame bridge was rehabilitated with external prestressing tendon and steel plate pasting methods. Structural response sensors were deployed during the rehabilitation process for long-term monitoring. Through analysis and evaluation, the following conclusions can be made:

(1) Through the construction of Finite element model for the rehabilitated bridge, theoretical calculation of the serviceability limit state and the ultimate limit state were made. Lowerbound, upperbound compressive stress, principle compressive stress, principle tensile stress as well as deflection were calculated. Maximum deflection was calculated to be 75.61mm at midspan of span 2.

(2) Static and dynamic loading tests were performed before and after bridge rehabilitation, for the purpose of verification as well as the deduction of safety thresholding. Structural responses have shown improvement after the rehabilitation. Maximum deflection has decreased from 37.9mm to 27.6mm.

(3) Instead of using characteristic value of an action, quasi-permanent value of a variable action, as well as representative value of an action, a new method of safety thresholding based on experimental static loading test was proposed: A color-coded five-level safety standard system. The order of highest risk to lowest risk are critical (red) -> high risk (purple) -> to be determine (yellow) -> middle risk (green) -> low risk (green). Threshold values of the bridge safety standard were developed based on static loading test and theoretically calculated ultimate limit state. Maximum ultimate limit state values serve as the critical level threshold, maximum static loading test values serve as the high-risk level threshold, threshold for the rest of the levels uses reduction coefficients 0.95, 0.9 and 0.8 of the maximum static loading test values.

Overall, the bridge is under safe operating condition and the rehabilitation was successful. The proposed simplified safety standard thresholding technique for SHM is sufficient for practical use and application. Hopefully this will provide insights into SHM software development as well as for condition evaluation of other bridge structures.

REFERENCES

- [1] Cross E., Koo K., Brownjohn J., Worden K., 2013. Long-term monitoring and data analysis of the Tamar Bridge. *Mechanical System and Signal Processing*, vol. 35: 16-34
- [2] Gatti M., 2019. Structural health monitoring of an operational bridge: A case study. *Engineering Structures*, vol. 195: 200-209,
- [3] Maria-Giovanna M., Alberto B., Luis F. R., Paulo Amado M., Paulo B. L., 2018. An Overview on Structural Health Monitoring: From the Current State-of-the-Art to New Bio-inspired Sensing Paradigms. *International Journal of Bio-Inspired Computation*, vol. 1, issue 1:1
- [4] Yonghui A., Eleni C., Sung-Han S., Simon L., Bartlomiej B., Jinping O., 2019. Recent progress and future trends on damage identification methods for bridge structures. *Structural Control and Health Monitoring*, vol. 26:e2416



- [5] Moughty J. J., Casas j., 2017. A State of the Art Review of Modal-Based Damage Detection in Bridges: Development, Challenges, and Solutions. *Applied Sciences*, vol. 7, no. 5
- [6] A. Mordini, K. Savov, and H. Wenzel, 2007. The Finite Element Model Updating: A Powerful Tool for Structural Health Monitoring. *Structural Engineering International*, vol. 17:pp. 352-358
- [7] JTG/T J21-01-2015 Load test method for highway bridge, P. s. R. o. C. Ministry of Transportaion of the People's Republic of China, 2015.
- [8] Code for design of highway reinforced concrete and prestressed concrete bridges and culverts JTG D62-2004, 2004. Ministry of Transportation of the People's Republic of China
- [9] Specifications for Design of Highway Steel Bridge JTG D64-2015, 2015. Ministry of Transportation of the People's Republic of China
- [10] AASHTO LRFD bridge design specifications, 6th ed, American Association of State Highway and Transportation Officials, Washington DC, USA, 2012.
- [11] Wong k, Structural health monitoring and safety evaluation of Stonecutters Bridge under the in-service condition (Bridge Maintenance, Safety, Management and Life-Cycle Optimization), 2010. Boca Raton: Crc Press-Taylor & Francis Group (in English), pp. 2648-2655.
- [12] Schommer S., Nguyen V., Maas S., Zürbes A., 2017. Model updating for structural health monitoring using static and dynamic measurements. *Procedia Engineering*, vol. 199: 2146-2153
- [13] Liu M, Frangopol D, Kim S, 2009. Bridge safety evaluation based on monitored live load effects. *Journal of Bridge Engineering*, vol. 14, issue 4: 257-269
- [14] Zhang W, Shi B, Zhang Y, Liu J, Zhu Y, 2007. The strain field method for structural damage identification using Brillouin optical fiber sensing. *Smart Materials and Structures*, vol. 16, issue 3: 843-850
- [15] Wang X, Hu N, Fukunaga H, Yao Z, 2001. Structural damage identification using static test data and changes in frequencies. *Engineering Structures*, vol. 23, issue 6: 610-621
- [16] Catbas F, Aktan A, 2002. Condition and damage assessment: Issues and some promising indices. *Journal of Structural Engineering*, vol. 128, issue 8:1026-1036
- [17] Laory I, Hadj Ali N, Trinh T, Smith I, 2012. Measurement system configuration for damage identification of continuously monitored structures. *Journal of Bridge Engineering*, vol. 17, issue 6: 857-866
- [18] Yang Y, Yang J, 2018. State-of-the-Art Review on Modal Identification and Damage Detection of Bridges by Moving Test Vehicles. *International Journal of Structural Stability and Dynamics*, vol. 18, issue 2.
- [19] Chen X, Zhu H, Chen C, 2005. Structural damage identification using test static data based on grey system theory. *Journal of Zhejiang University: Science*, vol. 6 A, issue 8: 790-796
- [20] Nguyen V, Schommer S, Maas S, Zürbes A, 2016. Static load testing with temperature compensation for structural health monitoring of bridges. *Engineering Structures*, vol. 127: 700-718
- [21] Xu Y, Zhang C, Zhan S, Spencer B, 2018. Multi-level damage identification of a bridge structure: a combined numerical and experimental investigation. *Engineering Structures*, vol. 156: 53-67
- [22] Alexandra J R., 2014. Bridge Structural Health Monitoring using Statistical Damage Detection and Advanced Load Rating Methods. *Dissertations & Theses - Gradworks*.
- [23] Posenato D., Lanata F., Inaudi D., 2008. Model-free data interpretation for continuous monitoring of complex structures. *Advanced Engineering Informatics*. Vol. 22: 135-144



- [24] Feng D., Feng M., 2018. Computer vision for SHM of civil infrastructure: From dynamic response measurement to damage detection – A review. *Engineering Structures*. Vol. 156:105-117.

GEOSPATIAL AND TEMPORAL ANALYSES OF RURAL AREA FOR VEGETATION ANALYSIS

Paulina Raeva and Karel Pavelka, Jr.

Czech Technical University in Prague, Faculty of Civil Engineering, Department of Geomatics, Prague, Thákurová 2077/7, Czech Republic; paulina.raeva@fsv.cvut.cz, karel.pavelka1@fsv.cvut.cz

ABSTRACT

The current paper aims at presenting multitemporal monitoring of two crop fields using close-range aerial photogrammetric techniques with a combination of different sensors. A fixed-wing unmanned aerial vehicle was used to map the crops regularly in 2016 and 2017. The goal of the following study is to show the experimental results of an enhanced keypoint number extraction of NIR and TIR images and the importance of radiometric calibration of close-range data.

KEYWORDS

RPAS, UAV, multispectral data, agriculture

INTRODUCTION

The progression of technology has resulted in technical devices taking over many human labours in our daily life routines. This fact could be, on one hand, worrying but on the other hand, prosperous for many specialities. The advent of unmanned aerial systems (UAS) was first in the military sector, likewise many other geodetic devices, such as GNSS receivers which we nowadays cannot do without. Therefore, UAS or also RPAS (Remotely Piloted Aircraft Systems) have made their presence significant in Geodesy, Photogrammetry and Geoinformatics. Nowadays, they play an important role in monitoring agriculture, forestry or archaeology.

Aircraft with a fixed-wing is primarily focused on mapping vast and flat fields [1], for example, agricultural ones, moreover, they are the preferable platform for multitemporal aerial mapping. According to European research [2], unmanned aircraft have the advantage to help farmers take better care of their field and boost their yield. Bearing in mind the unstable weather conditions, the soil heterogeneity etc, farmers need a dynamic attitude toward atomization. As some others state [3] the RPAS is one of the possible ways to aid farmers in optimizing their profit and improve production.

STUDY AREA

Background of the study

This study began at the Department of Geomatics in 2016. It is a part of a project on mapping battlefield engravings built during the Thirty Years' War [4]. The RPAS mapping was provided to find remnants of an artillery camp fortification. Later, it was stated that these remnants are situated elsewhere but the imagery was used to evaluate the possible implementation of close-range multispectral photogrammetry in agriculture. The reason to carry out an agronomic survey was the information stated in the database LPIS that most of the fields suffer from a significant



percentage of soil erosion. The authors then reckoned that it would be challenging to trace problematic wet field spots with the help of a thermal infrared camera.

Location

The area of interest is nearby the village of Vysoké Sedlečte (49.83°N, 12.77°E), in the Pilsen Region in the Czech Republic (Figure 1 b). The average elevation is 570 m above sea level (Figure 1 a).



Fig. 1(a,b) – a: DMS 1 generation, CUZK; b: test fields near Vysoké Sedlečte

Crop description

In the current study, three crops were examined – spring barley, corn and winter wheat. The spring barley is usually planted in January. It does not need much watering because this may lead to decomposition of the crop. Spring barley grows in cool and dry areas and ripens for 60-70 days. Barley in the Czech Republic is harvested in the same period as wheat – July, August. The optimal growing conditions for winter wheat though are in high-drained soil.

The crop fields are situated in the cadastral territory of Vysoké Sedlečte. Detailed information is taken from the Land Parcel Information System (LPIS). According to the Czech State Investment Fund for Agriculture [5] the crops cultivated in field №3304/7 (according to LPIS) in 2016 were barley, corn and triticale and in 2017 winter wheat and barley.

METHODS AND TECHNIQUES

Flight campaigns

We used the fixed-wing platform eBee which is at disposal at the Department of Geomatics. It is completely autonomous and flies according to a pre-set flight plan which is created in eMotion. The basics of the flight plan are: setting a take-off location, start waypoint and location for landing and home waypoints in case of emergency. The core of a good flight plan is to set the take-off location to be higher than the area to be mapped. Moreover, crucial for the take-off and landing location is to be set against the upcoming wind. The flight campaigns took place in April, June and July 2016 and 2017. Every month the area was mapped with both near-infrared (NIR) and thermal infrared (TIR) sensor.



Near-infrared camera

For better understanding the crop health, we used a 4-band multispectral sensor. It is the multiSPEC 4C modified professional. This camera can capture images outside of the visible electromagnetic spectrum, it produces images in green, red, red-edge and near infra-red parts of the spectrum. The central wavelengths of the bands are as follows: green – 550nm, red – 660 nm, red-edge 735nm and NIR – 790nm [6]. The full camera resolution is 1.2Mpx. The camera takes imagery only in TIFF. The multiSPEC 4C has an irradiance sensor on top of it which helps the pre-flight calibration process and enables providing with absolute reflectance measurements. Radiometric calibration was performed before each flight. For this purpose, a radiometric target was put horizontally on the ground and a few images were taken from a 50 cm distance. The radiometric target is captured in all four bands. These images were later used in the post-processing procedure.

Thermal infrared camera

For better understanding the relationship between soil and crops, a thermal mapping was performed. We used the thermoMAP by senseFly. This is an advanced professional imaging solution for solar, industrial and agronomic inspections. It is capable of capturing imagery between 7.5 and 13.5 with a central wavelength – 10000.5 nm, the photo size is 640x512 pixels with 14 cm ground sampling distance (GCD) at 75 m flying altitude [7]. The capture rate is 7.5 photos per second or 7.5 frames per sec when shooting video footage. The scene temperature is between -40°C to 160°C with a temperature resolution of 0.1°C. This camera could be considered as an uncooled thermal infrared camera. The uncooled thermal cameras keep their temperature approximately equal to the ambient one, therefore, the temperature controlling system is simpler. These cameras base their system on bolometer technology.

DATA PROCESSING

The multispectral images were stored in 8bit TIFF with a resolution of 1280 x 960 with a focal length of 4mm. As the camera has four bands, four different folders were automatically created in the directory of the input imagery. Each of these folders contains the images from only one spectral band. We used Pix4Dmapper for our post-processing [8]. The software uses the Structure-from-Motion algorithm which searches for matching features in the dataset of overlapping digital images. The software automatically recognizes the band of each image. The thermal images were stored in 16bi TIFF with a resolution of 640 x 512 and a focal length of 9mm. The pixel values of the thermal images are stored in nanometers. Two processing templates were created for both image types. The difference is in the input values for keypoint extraction – 15 000 for NIR and 20 000 for TIR (Table 1 and Table 2). The important part for the camera calibration step with TIR is to opt for an alternative calibration pipeline which does not take into account oblique images with a Z angle larger than 35° based on the keypoint matching the software performs Automatic Aerial Triangulation (AAT) and Block Bundle Adjustment (BBA). The AAT is the process of determining X, Y and Z ground coordinates of the individual points based on the image coordinate measurements [9]. Figures 2 and 3 show the pixel errors, the average direction and magnitude of the reprojection error for each pixel. The number of automatically matched points is colour-coded between black and white. White indicates that more than 16 automatic points were extracted at the pixel location. Black, on the other hand, indicates that no points have been extracted. The number of extracted and matched keypoints was computed. The maximum number of keypoints for NIR (20 000) was reached only in the green-band images. Images from red, red-edge and NIR bands produced a lower number of keypoints. The maximum number of keypoints extracted from TIR images was approximately 12 000. Therefore, enhancing this number did not improve the image pairs



matching. It is important to indicate the fact that all NIR and TIR images have vignetting meaning they have shaded or blur edges. The edge vignetting is caused by the lens itself.

Tab. 1 - Comparison of the number of image keypoints in all four bands. only the green-band images reached the set values – 15 000

	Green		Red		Red-Edge		NIR	
	Keypoints	Matching	Keypoints	Matching	Keypoints	Matching	Keypoints	Matching
Median	12265	6022	12859	6065	12128	3653	11976	3607
Min	11320	831	12362	1614	11525	1031	11441	711
Max	15000	7242	13193	7270	12774	5362	12960	5433
Average	12298	5663	12816	5718	12128	3669	12021	3510

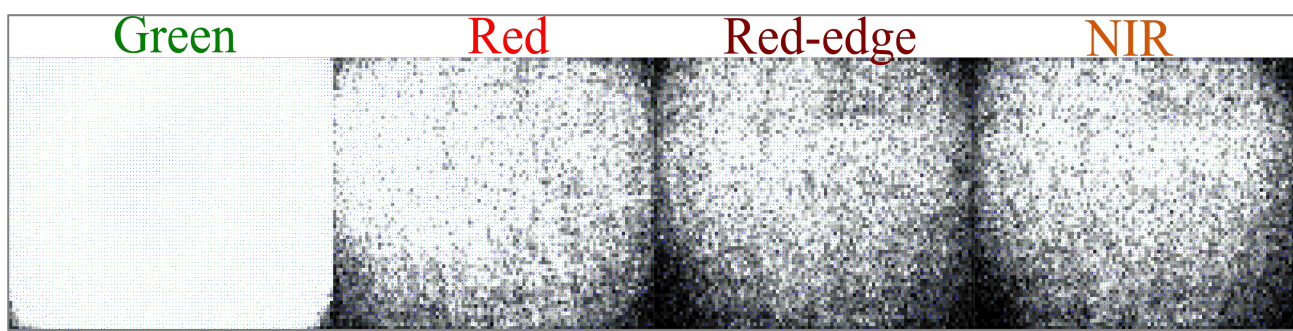
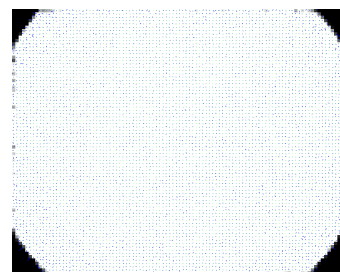


Fig. 2 – Keypoints extraction from all NIR band images. The white colour stands for more than 16 extractions and black – 0 extractions.

Tab. 2 - Number of keypoints extracted from the TIR images. The set value of 20 000 was not reached.

	IR	
	Keypoints	Matching
Medium	8387	3419
Min	5652	514
Max	11178	6253
Average	8405	3443



The Structure-from-Motion enables the formation of a sparse point cloud from all extracted and matched points. The sparse pointcloud serves as a base for the creation of a dense pointcloud. The average point number and density for the NIR projects is 9 mil. and 3 points [m³] and for the TIR – 7mil and 2 points [m³].

Creating DSM and Reflectance Maps

To create a Digital Surface Model (DSM), the dense pointcloud is used as a base. By default, the DSM is created with the same GSD resolution. The multispectral datasets resulted in a GSD of approximately 16cm/pix and the thermal ones – 20÷21 cm/pix. In this study, no orthophoto maps were created but reflectance maps instead. These two are quite similar in computation as both are corrected for perspective and the pixel values are obtained as a weighted average of the



pixels in the original images, corresponding to the particular pixel. Each reflectance pixel map represents the object reflectance or in other words, the pixel values are the values of the electromagnetic wavelengths.

To create a corrected reflectance map, one must apply radiometric corrections, especially when using a modified multispectral camera and comparing multitemporal datasets. Every object could be characterized with a spectral reflectance $\rho(\lambda)$ which could be defined as a ration between the intensity of the reflectance energy M_r and the intensity of the incident one M_i for a certain wavelength (λ)[10]:

$$\rho(\lambda) = \frac{M_r(\rho)}{M_i(\rho)} \cdot 100 [\%] \quad (1)$$

The reflectance values for the 4-band multispectral camera are given in Table 3.

Tab. 3 - Reflectance values of the radiometric panel for all camera bands

Green	17.12%	0.1712
Red	20.32%	0.2032
Red-Edge	24.68%	0.2468
NIR	35.13%	0.3513

The reflectance R [%] is computed according to (2) where DN stands for ‘digital number’, i – band and a, b are coefficients.

$$R = a_i DN + b_i \quad (2)$$

Index Maps

Thanks to the different spectral bands and the combinations between them, the so-called vegetation indices VI were computed. There are many types of VI classifications but for the current study, a few VI were used which are classified as ration VI.

The Normalized Difference Vegetation Index was applied to all multispectral imagery. The NDVI relates to the green biomass during vegetation growth. It relates to the difference between the reflected energy in the NIR and red part of the electromagnetic spectrum. The formula is as follows [11]:

$$NDVI = \frac{\rho_{NIR} - \rho_{RED}}{\rho_{NIR} + \rho_{RED}} \quad (3)$$

The second we computed is the Green Normalized Difference Index which is quite similar to the previous one. It uses the reflected energy in the green part of the spectrum instead of the red one. It is more sensitive to chlorophyll in the plants. The formula is as follows:

$$GNDVI = \frac{\rho_{NIR} - \rho_{GREEN}}{\rho_{NIR} + \rho_{GREEN}} \quad (4)$$

Moreover, we can calculate another important VI thanks to the multiSPEC 4c camera. This the normalized Difference Red-Edge Index (NDRE). This VI indicates the rapid change in vegetation reflectance between the visible and infrared light. NDRE is also sensitive to chlorophyll in plants. Its formula is:

$$NDRE = \frac{\rho_{NIR} - \rho_{RED-EDGE}}{\rho_{NIR} + \rho_{RED-EDGE}} \quad (5)$$

Last, but by no means, the least important index calculated is the temperature index TI. It is nor used very often in agriculture, but it gives relevant information about the soil moisture. As



stated in the description, the study fields are prone to erosion. In this case, it is essential to map the field with a thermal camera. The thermal reflectance maps contain information about the reflectance not only from the crop surface but also from the soil in case of sparse vegetation. Moreover, the electromagnetic waves of the camera are longer which provides reflectance even from beneath the soil. This information is converted into Celsius, according to the formula:

$$Temp [^{\circ}C] = 0.01 * ref. value - 100, \quad (6)$$

Where ref. value stands for the reflectance values in each pixel.

RESULTS

The results of the computation are index maps with the same colour-scheme for better understanding the crop changes in time. In Figure 4 we showed a comparison of NDVI and TI index of the spring barley for April and June 2016 and 2017. Problematic spots show similar behaviour during both years (indicated in a circle), e.g. the lower the NDVI the higher the temperature. This could mean either sparse vegetation or problematic soil pattern.

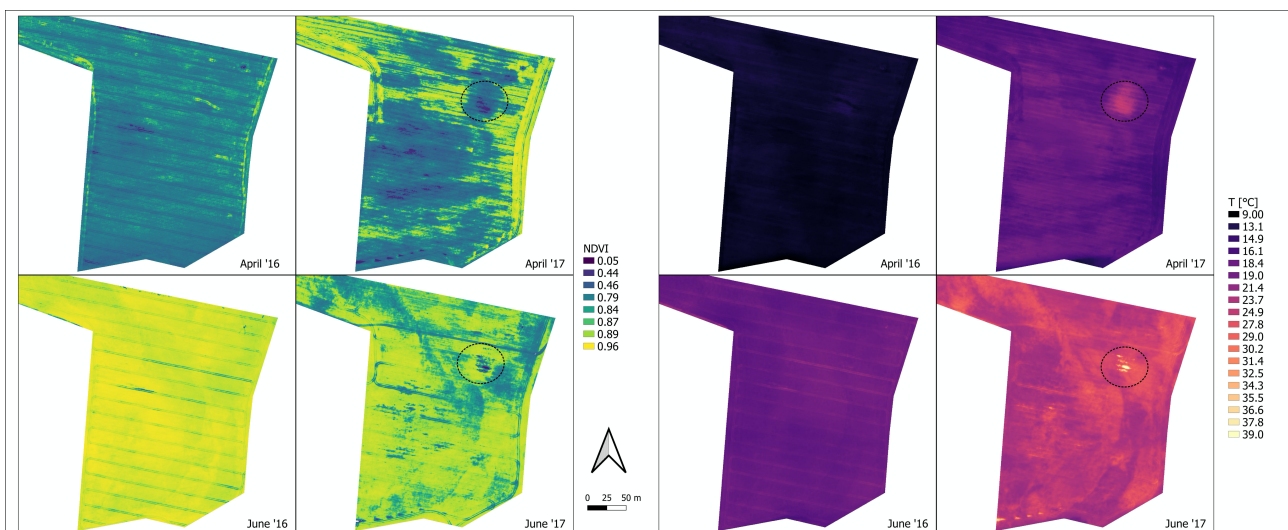


Fig. 3 – Comparison between NDVI and TI maps from 2016 and 2017 for spring barley. Spots with similar behaviour are indicated in a circle.

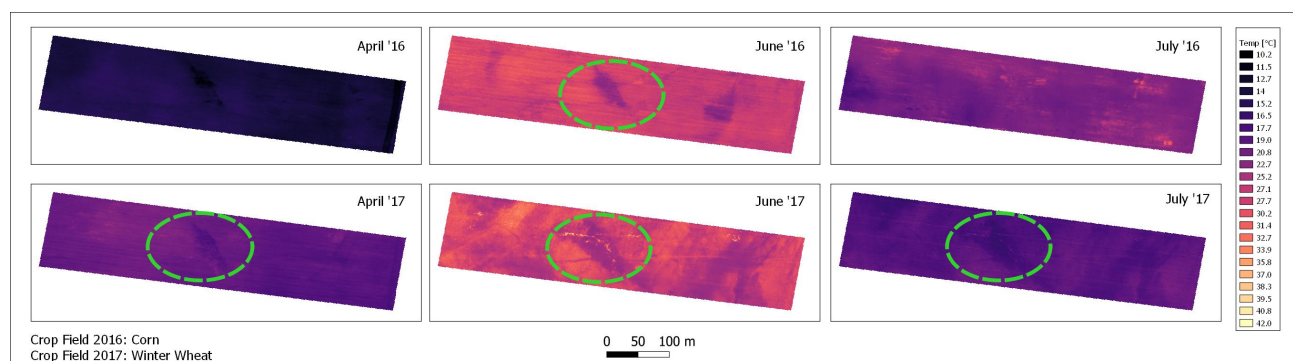


Fig. 5 – Comparison between TI maps from 2016 and 2017 for corn and winter wheat. Spots with similar behaviour are indicated in a circle.

The TI maps for the cornfield are shown in Figure 5. Again, it was noticed a spot which remains problematic during both years. The spot shows a lower temperature than its surroundings. We prepared a histogram comparison for the spring barely field for July 2017 in order to study the distribution of index values (Figure 6). We also added a SAVI (Soil Adjusted Vegetation Index) to the comparison.

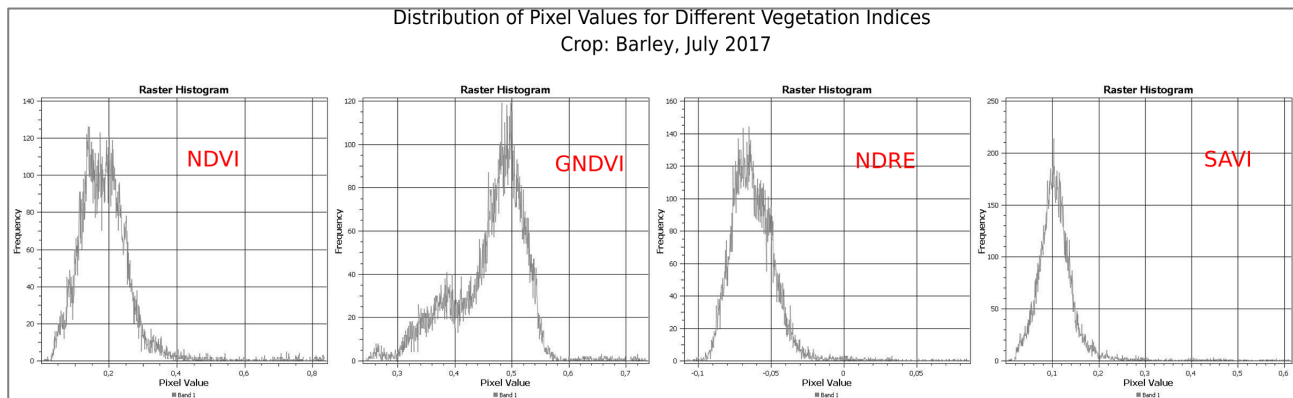


Fig. 6 – Distribution of pixel values for different vegetation indices – NDVI, GNDVI, NDRE and SAVI. The evaluated crop is spring barely in July 2017 – before harvesting.

EXPERIMENTS

This experiment is based on the importance of the radiometric calibration of the NIR images. Thus, two datasets of the cornfield were computed with no radiometric calibration and the NDVI values were compared. The datasets are from June and August 2016. The results for the crop field in June are:

Tab. 4 - Comparison of calibrated and non-calibrated DN for June 2016 – a cornfield

Cornfield June 2016	minNDVI	modeNDVI	maxNDVI	Stand. Deviation σ
Calibration	0,33	0,43	0,90	0,03
No Calibration	0,14	0,25	0,86	0,04

Tab. 5 - Comparison of calibrated and non-calibrated DN for August 2016 - a cornfield

Cornfield August 2016	minNDVI	modeNDVI	maxNDVI	Stand. Deviation σ
Calibration	0,47	0,95	0,96	0,02
No Calibration	0,31	0,91	0,94	0,03

MinNDVI stands for the minimum values, mode – the most frequent value and max – the maximum values.

ANALYSES AND DISCUSSION

The theoretical background seems easy to apply in close-range photogrammetry techniques. Unfortunately, this is not the case as one have to deal with preparing a current pre-



flight plan with bigger overlap than the theoretical 60% lateral and 80% longitudinal as applied in classic aerial photogrammetry. Mapping with a TIR camera like thermoMAP means providing a 90% overlap in both sides as the resolution is quite low and the post-processing, namely, camera calibration requires a certain amount of perpendicular to the terrain photographs. The same applies to the NIR multispectral cameras. Another challenge is the post-processing of the great amount of imagery. At first attempts. Not all NIR or TIR images were oriented. That is why in this study, we opted for an enhanced number of keypoints. The results show that 15 000 keypoints can be extracted only from the green-band photographs. And with these apriori value, the extracted points from the other bands (red, red-edge and NIR) are approximately around 10 000. The case is similar to computing TIR images. We have chosen to extract 20 000 keypoints, because of low image resolution means fewer matches between the images. Unfortunately, the maximum number of extracted keypoints was 12 000. Nonetheless, the challenge of processing TIR images were not over. Correct computation of a reflectance map is possible only when the camera positions are calibrated with an alternative pipeline method. This method, though, excludes oblique photos with more than 35-degree rotation. This is the reason why a large number of TIR were automatically ignored while processing. Any other calibration methods lead to ambiguities and distorted relative models. After computing the Bundle Block Adjustment with the NIR and TIR datasets, it was noticed the presence of lens vignetting. This leads to no point extraction from the image edges. Removing the vignetting from the TIR images will be a goal in our future work.

We experimented to test the importance of radiometric calibration of the DN when dealing with multitemporal monitoring of the same area. The results indicate differences between the calibration and non-calibrated values. Despite the fact, the maximum values are practically the same, the biggest difference are notices in the minimum and mode values.

We created statistical models in order to combine all the information from the VI computation. The graphical results may be sometimes misleading for people outside of the Remote Sensing sphere. Farmers should be provided with statistical analyses to better plan the future vision of their digital farms. Figure 7 shows the development of the spring barley field for 2016 and 2017 in months April, June and July.

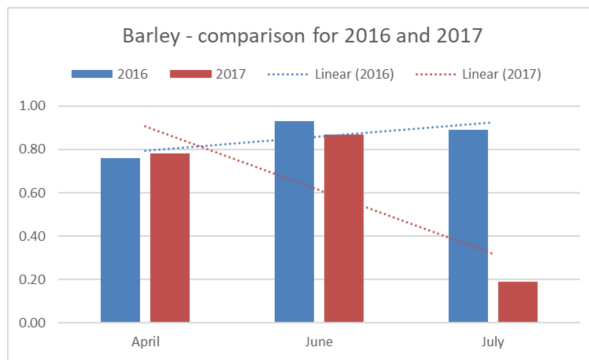


Fig. 7 – Comparison of NDVI values from 2016 and 2017 for spring barley.

The similar behaviour between NDVI and TI in problematic spots was noticeable, for instance in Figure 3. These spots may be due to dry erosion. The correlation and dependence of these two indices could be simply explained with the fact that the soil similarly reflects electromagnetic light in both NIR and TIR parts of the spectrum.

An overall comparison of all computed VI for the same field is shown in Figure 8. In 2016 its cultivated crop was corn and in 2017 – winter wheat.

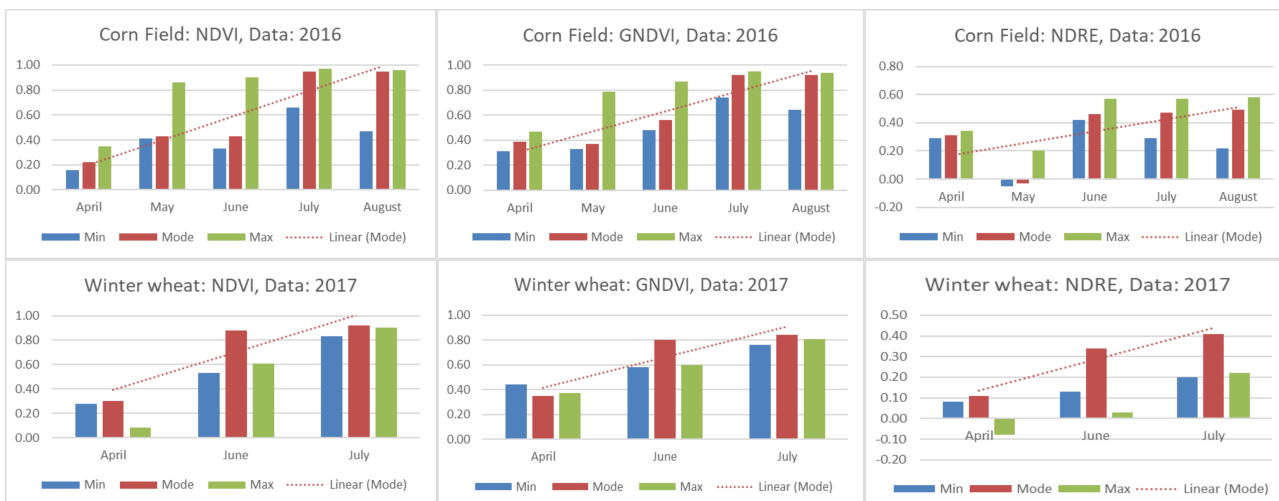


Fig. 8 – Development of the same field with two difference crops – corn (2016) and winter wheat (2017)

Future work for the authors will be to explain this correlation statistically with more data from different sensors. Future experiments will also include computing VI resist to soil refraction, e.g. SAVI (Soil Adjusted Vegetation Index) and seek for correlation between VI and TI. According to Figure 6 SAVI values are similar to the normal distribution. Moreover, NDVI and SAVI use the same spectral bands which means SAVI could be a more reliable index for multispectral close-range photogrammetric analyses

ACKNOWLEDGEMENTS

This paper is part of the project 161 -1612053A155 Development and Application of Modern Devices and Techniques for Spatial Data Acquisition, Processing, Analysis and Visualization funded by the Czech Technical University in Prague.

REFERENCES

- [1] K. Pavelka, J. Šedina, J. Pacina, L. Plánka, J. Karas, and V. Šafář, *RPAS Remotely Piloted Aircraft System*. Prague: České vysoké učení technické v Praze, 2016.
- [2] SESAR Joint Undertaking, “European Drones Outlook Study,” no. November, p. 93, 2016.
- [3] J. Lukáš *et al.*, “Využití bezpilotních prostředků v zemědělství 1.část,” 2016.
- [4] T. Janata, “Research Project on Engraving of the Thirty Years’ War Battlefields,” *Geodeticický a kartografický obzor*, Prague, p. 7, 2018.
- [5] SZIF, “Státní zemědělský intervenční fond,” 2020. [Online]. Available: <https://www.szif.cz/en?setCookie=true>.
- [6] SenseFly Ltd, *multiSPEC 4C CameraUser Manual*, no. February. 2017.
- [7] SenseFly Ltd, *thermoMAP Camera*. 2017.
- [8] Pix4D, *Pix4Dmapper 4.1 User Manual*. Lausanne, 2020.
- [9] P. R. Wolf, B. A. Dewitt, and B. E. Wilkinson, *Elements of Photogrammetry with Applications in GIS*. McGraw-Hill Education, 2014.
- [10] L. Halounová and K. Pavelka, “Dálkový průzkum Země,” p. 182, 2008.
- [11] J. W. Rouse, R. H. Haas, J. A. Schell, D. W. Deering, and J. C. Harlan, “Monitoring the Vernal Advancement and Retrogradation (Greenwave effect) of Natural Vegetation,” 1974.

FILTRATION VELOCITY OF WATER IN COARSE PLASTIC PARTICLES

Lukáš Svoboda, Tomáš Picek, Štěpán Zrostlík and Mikoláš Kesely

Czech Technical University in Prague, Faculty of Civil Engineering, Department of Hydraulics and Hydrology, Prague 6, Thákurova 7/2077, Czech Republic; lukas.svoboda.2@fsv.cvut.cz

ABSTRACT

Experimental investigation of the effect of particle geometry on the values of hydraulic conductivity using 5 plastic particle fractions of different shapes and sizes is presented in this paper. Conducted experiments serve as a background for ongoing research focused on sediment transport of erodible bed in tilting flume. When a flowing mixture of water and particles evolves above a stationary bed, the determination of flow rate of water filtered through stationary bed is very important in order to estimate the inaccuracy of total flow rate trough the flume. In order to evaluate the amount of infiltrate water, experiments were carried out in both laminar and turbulent flow regimes. The transition area was identified, and the results show only small effect of particle geometry on the transition between regimes. Experimentally identified values of hydraulic conductivity were used to calculate the amount of infiltrate water in the tilting flume for different inclination angles. Experimentally identified values of hydraulic conductivity are, for example, useful in designing industrial water filters, as the materials used to conduct experiments and those in filters are similar.

KEYWORDS

Hydraulic conductivity, Filtration, Plastic particles

INTRODUCTION

The necessity to determine the amount of infiltrate water flowing through the homogenous porous media occurred when working on a research project focused on intense sediment transport in open channel flow [1]. Porous materials can be very roughly characterized by the value of hydraulic conductivity, which is a commonly used parameter in various branches of civil engineering (for example in water or environmental management). The hydraulic conductivity is most frequently used to calculate the flow rate trough the porous materials. The computations are realized by the generally known Darcy's law equation [2,3].

METHODS AND EXPERIMENTAL SET UP

Our experimental evaluation of the hydraulic conductivity was carried out in an experimental cell situated in the Water Engineering Laboratory at Faculty of Civil Engineering of Czech Technical University in Prague. Experimental cell was made of transparent plexiglass. Height of cell was 1.05 m and dimension of rectangular cross-section was 0.22 m x 0.20 m (Fig. 1). The direction of the water flow through the cell was from the bottom to the top. The inflow rate was adjusted using a control valve on the inlet. The total flow rate was measured by mass method on the outlet. Tested porous material was placed between two steel sieves in order to mitigate the effects of buoyancy and hydrodynamic pressure.





Fig. 1 – Photo of experimental cell

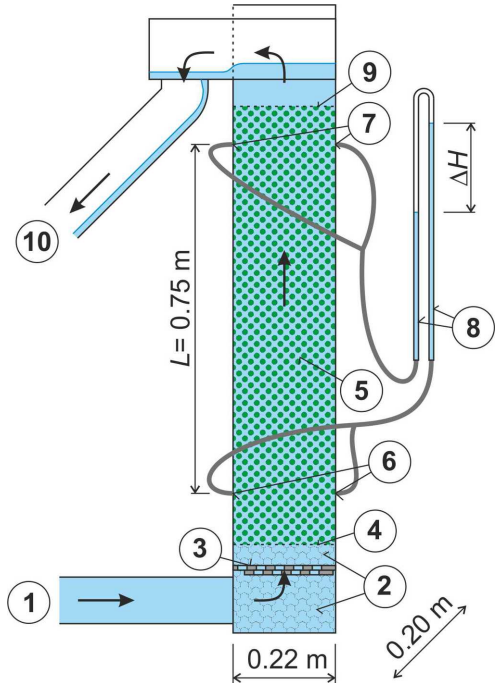


Fig. 2 – Schematic of experimental cell – 1 - inflow, 2 – geotextile, 3 – system of meshes, 4 and 9 - steel sieve, 5 – tested material, 6 and 7 – connection of U-tube, 8 – U-tube, 10 – outflow

Materials

Five fractions of plastic particles of different sizes and shapes were used to conduct the experiments, and as this work is connected to our earlier experiments in tilting flume [1], tested materials are identical. Properties of the particle fractions are given in Tab. 1 and photos of the particles can be seen in Figures 3 – 7.

Tab. 1 - Properties of used materials – d_1 and d_2 - diameters, h – height, d_{esp} - equivalent spherical diameter, ρ_s – density, P – porosity

Quantities	units	F30	F60	HSF3	TLT25	TLT50
d_1	mm	4.05	6.43	3.32	4.99	4.75
d_2	mm		5.78	2.54		
h	mm	2.24	5.14	3.89	2.08	4.9
d_{esp}	mm	3.65	6.42	3.18	4.23	5.41
ρ_s	kg/m ³	1368	1419	1358	1381	1307
P	-	0.38	0.38	0.40	0.40	0.40

Where d_1 is the major axis length of the particle ellipse cross section and d_2 is the minor axis length, h is the averaged height of a particle (maximum dimension in case of tri-axial ellipsoid HSF3, and height of the remaining particle fractions F30, F60, TLT25 and TLT50), value of porosity, P , was measured using a graduated cylinder, d_{esp} is the diameter of the equivalent sphere derived from the volume of the averaged particle of each fraction.

Regarding shape of the particles, F30 and TLT25 can be described as contact lenses, F60 and TLT50 as cylinder with concave and convex face and the HSF3 a tri-axial ellipsoid. [1]





Fig. 3 – F30



Fig. 4 – F60



Fig. 5 – HSF3



Fig. 6 – TLT25



Fig. 7 – TLT50

Procedures

All materials were put in the cell filled with water and simultaneously mixed to attainment a random position of particles as in the experiment of a sediment transport in the tilting flume.

The air on the particles was removed from the experimental cell by repeated mixing using a steel rod during the cell filling procedure. In order to achieve similar experimental conditions to those of our earlier experiments, focused on sediment transport of erodible bed in tilting flume, no additional stress was applied to the surface of the particle bed (which would achieve higher degree of particle consolidation). The temperature of flowing water was in ranging from 14 to 24 °C.

Various experimental measurements covering wide range of flow rates were performed in order to determine possible range of hydraulic conductivity values in both laminar and turbulent flow regimes. Experimental procedure consisted of four steps. First step was to set the flow rate. Second step was to wait for the flow and pressure conditions to stabilize. After the stabilization period, the pressure heights difference ΔH was measured between lower and upper pressure sampling using a U-tube and hydraulic gradient i was calculated as a ratio of ΔH and the distance between lower and upper pressure sampling L .

The third step was the determination of flow rate by equation $Q = V/t$. First, a water sample was taken in the given time t , then weight of the water sample m was measured. The value of the density ρ , used in the calculations, was derived from the temperature of the water sample. Finally, the volume of the sample was given by equation $V = m/\rho$.

The last step was to calculate the value of the hydraulic conductivity k using a standard Equation 1 [2]

$$k = \frac{L}{\Delta H} \cdot \frac{Q}{A} \quad (1)$$

Where A ($0.22 \times 0.20 = 0.044 \text{ m}^2$) is the area of cross section and Q is the flow rate of water.

RESULTS

Hydraulic conductivity

Calculated values of hydraulic conductivity are plotted in Fig. 8 against the flow rate. Results show, that the values of hydraulic conductivity are affected by the size and shape of pores between particles, which are mostly affected by the shape and the size of the particles. Value of the hydraulic conductivity is affected by the volume of the pore, which is directly proportional to the volume of the particle, and thus a simple trend is expected: The larger the particle, the higher value of hydraulic conductivity.

This applies to all particles except the TLT25 and F30 fractions. The F30 particles are smaller than TLT25, yet calculated values of hydraulic conductivity for TLT25 are smaller than those calculated values for F30.

However, the difference between hydraulic conductivity values is small, and could be caused by the difference in the shapes of the particle fractions. F30 particles (contact lenses) are more curved than TLT25 (contact lenses).

The values of hydraulic conductivity decrease with an increase of the flow rate, which indicates a turbulent flow regime (see Fig. 8.), the region of more or less constant value of hydraulic conductivity in the Figure 8 indicates a laminar flow regime.

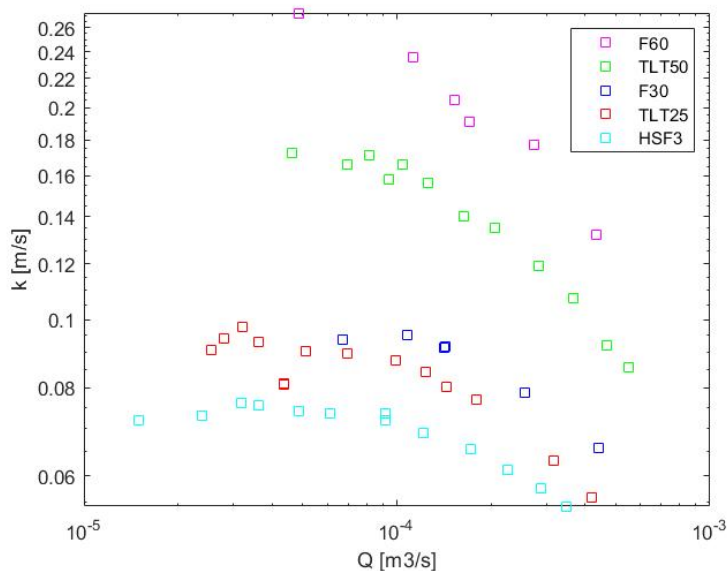


Fig. 8 – Calculated values of hydraulic conductivity (logarithmic scale)

Comparison of Reynolds number critical values and the transition between laminar and turbulent flow regimes

Hydraulic conductivity is given not only by properties of the particles but also by flow rate of water. The determination of hydraulic conductivity is based on Darcy's law (linear relationship $v_i = k \cdot i$, where i is the hydraulic gradient and k the hydraulic conductivity). It should be noted that the constant value of hydraulic conductivity is applicable only in laminar flow regime. In turbulent flow



regime the relationship between v_f and i is non-linear and the value of k must be modified when the Darcy's law is used in the turbulent flow regime. [2,3]

A standard procedure for evaluation of the flow regime is to calculate the value of the Reynolds number and then compare the value to a critical one, which corresponds to point of transition between the regimes. In particular conditions of our experiments, equation (2) can be used:

$$Re_n = d_{por} \cdot u \cdot \frac{\rho}{\eta} \quad (2)$$

Where d_{por} is the effective pore diameter, u is the mean velocity of the flow in pore, which was calculated with the use of v_f and area of pore, ρ is the liquid density, and η its viscosity. [3]

The value of Re at the point of the transition is for the flow in straight tubes somewhere between 2000-4000, but in porous materials the value of Re should be smaller. [3,5]

Another equation, which can be used to calculate the value of Reynolds number, is Equation (3):

$$Re_f = \frac{1}{0.75 \cdot P + 0.23} \cdot \frac{v_f \cdot d_{ef}}{v} \quad (3)$$

Where P is the porosity, v_f is the mean velocity given by Q/A , d_{ef} is the effective grain size (which, in case of materials of uniform grain size, can be substituted by medium size of the particles) and v is the kinematic viscosity ($v = \eta/\rho$) (3). [4]

The value of Re at the point of transition valid for the flows of ground water is 7 – 10 according to the research by Pavlovsky [4,5].

In Fig. 9 hydraulic gradient i is plotted against the velocity of the flow through the sediment layer v_f for all of the particles used in our experiments. Continuous lines interlace the points for small values of velocity of the flow through the sediment layer, where linear relationship between v_f and i is applicable. All of the measured points where linear relationship is applicable are marked by crosses. The results show, that the rise of the velocity of the flow through the sediment layer is linear at first, but changes to non-linear with rising hydraulic gradient. It has been proven in the literature that the point at which the trend changes from linear to non-linear indicates the point of the transition between laminar and turbulent flow regimes. [3]

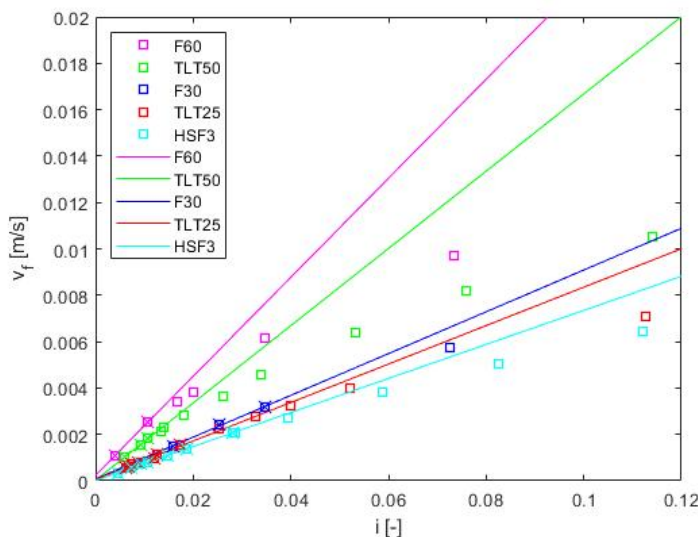


Fig. 9 – Relationship between hydraulic gradient and velocity of the flow through the sediment layer. Legend: continuous line – a linear relationship between v_f and i valid for laminar flow regime, square with a cross – points in laminar part, square – points in turbulent part

In order to determine the threshold between laminar and turbulent flow regimes, values of Reynolds number were calculated using the equations 2 and 3. The values of the velocity of the flow through the sediment layer used in the calculations were taken from Fig. 9 where the relationship of $v_f - i$ changes from linear to non-linear. The point of transition was determined by linear interpolation of adjacent points, first, point 1, and 2, next 1, 2, 3 etc. When the line started changing the last point of penultimate step, was sign as the threshold. The results of the calculations were compared to the limits values reported in mentioned publication. [2, 3, 5]

In equation 2, the size of effective pore diameter is used. In our calculations, the parameter is defined by equation 6, which is derived from equation 4 and 5. Where V_{por} is volume of a pore, V_{par} is volume of particles, P is porosity, d_{por} is diameter of a pore and d_{par} is the diameter of the equivalent sphere particle.

$$P = \frac{V_{por}}{V_{por} + V_{par}} \quad (4)$$

$$\frac{V_{por}}{V_{par}} = \frac{d_{por}^3}{d_{par}^3} \quad (5)$$

$$d_{por} = d_{par} \cdot \left[\frac{P}{1-P} \right]^{1/3} \quad (6)$$

Tab. 2 – Calculated values of Reynolds number

Quantities	units	TLT25	TLT50	F30	F60	HSF3
Re_f	-	12.1	18.2	22.0	30.6	12.1
Re_n	-	14.0	21.1	25.4	35.3	14.0



Tab. 2 shows the values of Reynolds number (Re_n) calculated from Equations 2 and 3. When the Equation 2 is used, resulting Re_n values for all particle fractions are between 14 – 36. These results correspond with the notice reported by Hillel. When the Equation 3 is used, resulting Re_n values for all particle fractions are between 12 – 31, which is very close to the values reported by Pavlovsky.[4,5] The value of Re at the point of transition for straight tube is 2000 – 4000, but in porous materials it should be significantly less. This is due to the fact that the pores are not connected to each other as straight tube, but they are randomly distributed what is given by their shapes, size etc. [3, 4], which can be seen in the Figure 10. [3,5]



Fig. 10 – Photo of F60

Comparison of flow rates above and in the deposit layer

The ongoing research [1] to which this experiment is connected is focusing on investigation of internal structure of steady uniform, turbulent open-channel flows over an inclined granular bed in the upper plane regime with intense transport of sediment. The flow can be divided into three layers. Stationary bed of deposited particles at the bottom of the channel forms the first layer. A second layer above the stationary bed of particles, through which the particles are transported we call the transport layer. Third and last layer is that of clear water. It is necessary to know the flow rate of the mixture, which is equal to the total flow rate through the flume minus the flow rate of infiltrate water in order to evaluate the conducted experiments.

Mean velocity of the flow through the sediment can be determined for given hydraulic slope and material on the basis of relationship " $v_f - l'$ ", which can be derived from Fig. 9, where velocity of the flow through the sediment layer is plotted against hydraulic gradient. Experiments in the tilting flume were performed under steady and uniform flow conditions (when constant height of the sediment bed was achieved across the whole length of the flume), therefore the hydraulic gradient is considered to be equal to the slope of the tilting flume. Ratio of velocity of the flow through the sediment layer v_f and velocity of the flow above the bed v_s against the hydraulic gradient can be seen in Figure 11. Velocity of the flow above the bed v_s is given by ratio of flow rate and profile area above the bed. The flow rate above the bed is given by the difference between the total flow rate through flume and through the sediment, which was determined by using the procedures described in this paper. Based on the ratio of v_f/v_s , the ratio of heights of flow layers above the stationary bed and the thickness of the deposit layer, it is possible to determine the flow rate through sediment.

The experiments were conducted in rectangular tilting flume of width equal to 0.20 m. Resulting database includes various test runs that cover quite broad range of inclination angles, total flow rates and layer heights. To make some sense of investigated values, overview of the ranges can be seen below in Table 3. Further details on conducted experiments can be seen in authors previous work [1].

Tab. 3 – Measuring range (i – slope of tilting flume, Q_{flume} – value of whole flow in tilting flume, h_{deposit} – height of deposit layer, $h_{\text{transport}}$ – height of transport layer)

Material	i [-]		Q_{flume} [l.s-1]		h_{deposit} [mm]		$h_{\text{transport}}$ [mm]	
	min	max	min	max	min	max	min	max
F30	0.0268	0.0517	5.80	6.38	20	53	38	50
F60	0.0119	0.0794	8.24	10.26	19	64	53	77
HSF3	0.0050	0.0580	6.03	11.98	18	62	29	98
TLT25	0.0060	0.0671	6.16	8.09	18	55	44	100
TLT50	0.0080	0.0547	10.00	15.90	17	60	29	101

The Figure 11 shows that the ratio of velocities increases with increasing slope of water surface, which means, that with increasing slope the velocity of infiltrate water increases with higher rate, than the velocity in upper layers of the flow. This is caused by the increasing number of suspended particles in the flow above the deposit layer, which reduces the mean velocity of the transport layer as increasing concentration of particles provide more resistance to the flow.

Just to roughly quantify the v_f/v_s ratio, for higher slopes the values can reach up to a few percent.

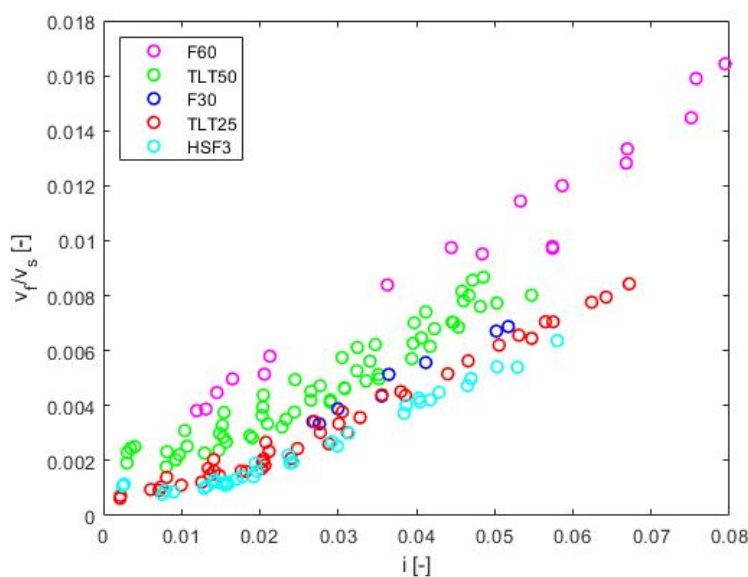


Fig. 11 - Ratio of v_f and v_s against the hydraulic gradient

CONCLUSIONS

5 plastic particle fractions of different shapes and sizes were experimentally investigated in order to obtain their specific values of hydraulic conductivity. Analysis of the results showed, that



the values of hydraulic conductivity are by both, the size and the shape of the particles. While the size of the particle has a major effect on the value of the hydraulic conductivity, results also show that effect of the shape of the particles is not negligible.

Further analysis showed that the flow regime has also a strong effect on the values of hydraulic conductivity. While constant value of hydraulic conductivity can be applied under laminar conditions, in turbulent flow regime the value of hydraulic conductivity must be modified, as the corresponding value can be significantly lower, when the Darcy's law is used.

When experimentally identified values of hydraulic conductivity were used to calculate the amount of infiltrate water in a tilting flume for different inclination angles, results showed, that the ratio of the velocity in the sediment layer and the velocity above the stationary values increase with the increasing inclination of water surface.

ACKNOWLEDGEMENTS

The research has been supported by the Czech Science Foundation through the grant project No. 16-21421S.

REFERENCES

- [1] Matoušek V., Bareš V., Krupička J., Picek T., Zrostlík Š., 2015. Experimental investigation of internal structure of open-channel flow with intense transport of sediment. Journal of Hydrology and Hydromechanics, vol. 63: 318–326 pp
- [2] Darcy, H. P. G., 1856, Les Fontaines Publiques de la Ville de Dijon, Victor Dalmont
- [3] Hillel D., 2004, Introduction to environmental soil physics, Boston, Elsevier Academic Press, pp. 184 – 195
- [5] Agroskin, I.I., Dmitrijev, G.T., Pikalov, F.I., 1954, Handbook of hydraulic, (Leningrad and Moscow) (in Russian), 399 pp (in Russian)
- [4] Másiar E., Kamenský J., 1989. Hydraulika pre stavebných inžinierov II, (Alfa, Bratislava) 26 pp (in Slovak)
- [5] Idelchik, I. E., Steinberg M. O., MALYAVSKAYA Greta R., MARTYNENKO Oleg G., 2003. Handbook of hydraulic resistance. 3rd Edition, (Jaico Publishing House) 77 pp

DESIGN OF HIGH-SPEED RAILWAY (HSR) LONG-DISTANCE TUNNEL INDEPENDENT CONTROL NETWORK

Alhossein Mohamed and Peng Qiyuan

School of Transportation and Logistics, Southwest Jiaotong University Chengdu 610031, China ;
mxhx83@163.com, qiyuan-peng@swjtu.edu.cn

ABSTRACT

Establishing a high-speed railway long-distance tunnel independent control network according to "one point and one direction" will often produce lateral deviation and long and short chains in the joint section. It is necessary to take technical measures such as control network rotation or long and short chain to solve. Combined with the case of a network of independent control network for a long-distance tunnel of a high-speed railway in China, based on the results of the original reference ellipsoid and line control points, the central meridian (L_0) of the tunnel project center with the longitude of the tunnel is plotted, and the average tunnel elevation of the tunnel is Projection earth height (H_0), coordinate transformation calculation and relative stability and reliability analysis of existing line plane control points; select one stable control point of tunnel entrance and exit as starting point, in new projection parameters (L_0 Under H_0), the overall adjustment is carried out to establish an independent control network for the long tunnel. The results show:

- (1) The tunnel independent control network established by the method has high precision and uniform error, which can meet the requirements of network construction precision and improve the tunnel penetration accuracy;
- (2) "One point one direction" Compared with this method, the joint segment control point ($S = 9.1$ km) with the same baseline file, starting point and projection parameters, the maximum coordinate difference Δx is -63.4 mm, Δy is 85.3 mm, requiring technical processing;
- (3) The method can solve the problems of large lateral deviation and long and short chain of the connecting section, and ensure the smooth connection between the tunnel and the adjacent structure.

KEYWORDS

HSR, Control, Tunnels, Network

INTRODUCTION

According to the length of the Railway Tunnel Design Code (TB10003—2016), the tunnel is divided into: short tunnel ($L \leq 500$ m), medium long tunnel ($500 < L \leq 3000$ m), long tunnel ($3000 < L \leq 10000$ m) and extra-long tunnel ($L > 10000$ m) [1]. The "High-speed Railway Engineering Measurement Specification" (TB10601-2009) stipulates that the engineering independent coordinate system is a plane rectangular coordinate system established by projection of arbitrary central meridian and elevation projection surfaces. When the line plane control network (CPI, CPII) at both ends of the tunnel entrance is not in a projection belt, an independent tunnel construction control network can be established. It is advisable to use the tunnel average elevation surface as the reference plane and take the central meridian of the tunnel project center line as the coordinate projection; the construction independent coordinate system with the tunnel long straight line or



curved tunnel tangent (or common tangent) as the coordinate axis, the selection of the coordinate axis should be Convenient for construction [2].

Yang Liu and Zuo Zhigang explored the method of changing the projection datum and the central sub-line to weaken the deformation length of the control network. The one-to-one direction method was used to establish the tunnel independent control network [3]. Ye Changxuan studied the fixed-width control of the special long-distance tunnel, and used the method of controlling the rotation of the network to solve the lateral deviation of the connecting section [4]. Yang Xuefeng and Liu Chenglong used two methods to check and analyse the direction angle of the independent control network of the long tunnel group, and established the independent control network of the long tunnel group by point-by-point method [5]. Hong Jianghua and Shi Debin et al. studied the layout, observation scheme, accuracy evaluation and penetration error of the planar GPS network of the long tunnel [6]. All these research results have certain practical significance for improving the penetration accuracy of the control network outside the tunnel. However, the tunnel independent control network established by the one point one direction method often leads to large lateral deviation and long and short chains. It is easy to handle in the subgrade, and it is more difficult to eliminate when the bridge is connected with the tunnel.

The research ideas of this paper are: Based on the original reference ellipsoid reference and the results of the existing line control points, the central meridian (L_0) projected by the center line of the tunnel engineering center is used to project the earth height (H_0) with the tunnel mean rail elevation, and the existing plane control points are respectively switched to the independent control network coordinate system (L_0 , H_0), analyse the stability and reliability of the starting point, select a stable and reliable control point of the tunnel entrance and exit as the starting point for the overall adjustment, and establish under the new projection parameters (L_0 , H_0) Tunnel independent control network.

The tunnel's independent control network established by the method can effectively solve the long and short chain and the lateral deviation, and does not need to rotate or set the long-short chain and other post-processing measures to ensure the smooth connection between the tunnel and the adjacent structure.

THE NECESSITY OF ESTABLISHING AN INDEPENDENT CONTROL NETWORK FOR LONG TUNNELS

Control projection length deformation value

The projection length deformation value refers to the discrepancy between the measured length and the inversed coordinate value after the correction of the two dimensions [7]. In the construction measurement process, in order to ensure the relative accuracy between adjacent points in the construction control network, it is necessary to control the projection length deformation value within a certain range. The railway engineering control network is a long and narrow strip network, and its projection length deformation value is affected by factors such as the elevation of the point, the elevation of the projection surface and the central meridian [8]. In order to improve the relative accuracy of adjacent points in the railway control network and control the projection length deformation value, the "High-speed Railway Engineering Measurement Specification" (TB10601-2009) stipulates that "the projection length deformation value of the coordinate system on the elevation surface of the corresponding line rail surface design is not more than 10mm /km".

Tunnel penetration needs

The tunnel penetration error can be divided into vertical, horizontal and elevation penetration errors from the spatial distribution. The elevation penetration error can be controlled by



the precision levelling technology. The longitudinal penetration error only affects the distance (or mileage), and the transverse penetration error has a direct impact on the tunnel quality. Once the tunnel penetration surface deviation is too large, it is difficult to correct it by technical means. It is usually necessary to carry out secondary construction of the lined section (or the inverted section), causing huge economic losses. The tunnel independent control network generally builds a network at a time, covering all construction work areas. The control points have high precision, the orientation of the holes is accurate, and the error of the whole network is uniform, which is beneficial to the construction measurement surveys and checks.

Construction measurement needs

In addition to the main tunnel entrance and exit, the long tunnel often has auxiliary tunnels such as inclined shafts, horizontal tunnels or parallel guide holes. The general terrain is complex and often spans several engineering coordinate systems. For different engineering coordinate systems, control points often need to be swapped for calculations and are prone to errors. Therefore, it is necessary to establish a unified independent coordinate system. The "High-speed Railway Engineering Measurement Specification" (TB10601-2009) stipulates that "when the line plane control network (CPI, CPII) at both ends of the tunnel entrance is not in a projection belt, an independent control network of tunnel construction can be established."

"TWO-POINTS METHOD" ESTABLISHES AN INDEPENDENT CONTROL NETWORK FOR LONG TUNNELS

Generally, the tunnel meridian is used as the coordinate projection central meridian, and the average elevation of the tunnel rail surface is used to project the earth's height. The existing plane control points are respectively converted into the tunnel independent control network coordinate system to carry out the stability of the existing control points. After the reliability analysis, each control point of the tunnel entrance and exit is selected as the starting point, and the overall adjustment is performed under the coordinate system of the independent control network to establish an independent control network for the long tunnel. The steps of the "two-point method" network construction are as follows:

- (1) Selection of points and network design. Combined with the topographical features, geological conditions, traffic conditions and original plane control points of each tunnel construction operation area, the site selection and burial of piles are carried out in each tunnel construction operation area, and each construction area is buried with 3 to 4 plane control piles.
- (2) Select the projection parameters. Take the longitude of the tunnel engineering center as the central meridian (L_0) of the coordinate projection, and take the average tunnel elevation of the tunnel as the projection height (H_0).
- (3) Starting point coordinate conversion calculation. Convert the existing planar control points to the tunnel independent control network coordinate system (L_0, H_0).

Perform closed loop, repeated baseline test and three-dimensional unconstrained network adjustment on the tunnel GPS network. After meeting the tolerance requirements, perform stability and reliability analysis of the starting point. Then select one control point of the tunnel entrance and exit as the starting point. The overall adjustment is performed under the new projection reference to establish a tunnel independent control network.

The side length and angle detection are performed on the independent control network constructed, and the accuracy of the independent control network is evaluated.

CONSTRUCTION OF INDEPENDENT CONTROL NETWORK

Project overview

A railway Wulingshan tunnel (double-line single-hole) is located in Cili County, Zhangjiajie City, Hunan Province. The starting distance is DK234 + 491. 2 ~ DK243+535. 3, which is east-west and 9.044 km long. The tunnel is located in the middle and low mountainous areas of Wuling Mountain, with an altitude of 550 to 800 m. The tunnel is only provided with one construction guide, which is located at the entrance of the tunnel and intersects the tunnel with the DK235+460. The tunnel entrance elevation is 389. 442 m, the exit rail elevation is 458. 9082 m, and the plane position is between 110°45' and 110°51'. The longitudinal slope of the tunnel's body is: 17. 4‰ /8. 8 m, 17. 5‰ /4950 m, 6‰ /600 m, - 6‰ /3485. 3 m. DK240 +365. 634 ~ DK241+562. 069 On the curve of R = 7 000, DK242+754. 763 to the exit on the curve of R = 4 500, the rest are on the straight-line segment.

The Wulingshan Tunnel has 4 plane control points (co-points with elevation), 2 tunnel entrances (CP I163 and CP I164), and 2 tunnel exits (CPI165 and CPI166), both of which are high-speed rail standards. There are no control points around. Obstructed, the soil is hard and well preserved. The tunnel reference ellipsoid is consistent with the entire line, and the basic ellipsoid parameters of the 2000 national geodetic coordinate system (long semi-axis $a = 6\ 378\ 137$ m, flattening $\alpha = 1 /298. 257\ 222\ 101$) are used, crossing two engineering coordinate systems, see Table 1.

Tab. 1 - Wulingshan Tunnel Construction Coordinate System

Coordinate system number	Central meridian	Projection surface height /m	Elevation anomaly /m	Starting mileage	
				start point	end point
CK-12	110°45'	315	-25	DK231+000	DK235+000
CK-13	110°50'	375	-25	DK234+700	DK248+100

Network shape design

The hole's subnet and other subnets are interconnected to form a main network, and the hole's subnet is arranged in a geodetic quadrilateral. The newly buried control points are placed in places with wide vision, good visibility, solid soil and not easy to damage. Existing control points are included in the tunnel independent control network, as shown in Figure 1.

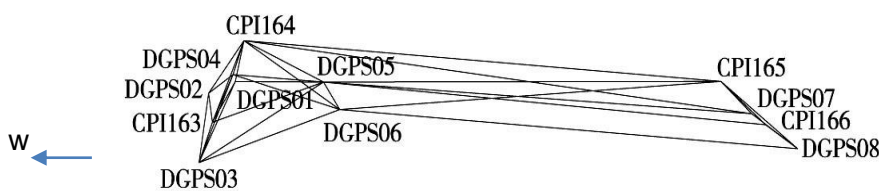


Fig. 1 - Distribution of control points in Wulingshan tunnel

Network construction accuracy level

According to the "High-speed Railway Engineering Measurement Specification" (TB10601-2009), the independent control network of Wulingshan Tunnel is established according to the accuracy of the first-class GPS network of high-speed railway. The specific precision control indicators are shown in Table 2 and Table 3.

Tab. 2 - Plane control network accuracy requirements

grade	Fixed error a /mm	Proportional error coefficient b/ (mm /km)	Error in baseline orientation / ("")	Relative error of side length between constraint points	Relative error of the weakest side length after constraint adjustment
First Class	5	1	≤0.9	1/500 000	1/250 000

Tab. 3 - Basic technical requirements for GPS surveying operations

Type	Project	Precision index
Static measurement	Satellite altitude angle / (°)	≥ 15
	Total number of active satellites	≥ 4
	Effective observation time of any satellite in the time period /min	≥ 30
	Length of time /min	≥ 120
	Number of observation periods	≥ 2
	Data sampling interval /s	15~ 60
	PDOP or GDOP	≤ 6

Projection parameter selection

The Wulingshan tunnel is a slope with a plane longitude between 110° 45' and 110°51' and a rail elevation of 389 to 479 m. Take the average meridian 110°48' as the central meridian of the independent coordinate system, and take the average elevation surface 434 m as the projection height.

Starting point coordinate conversion calculation

Referring to the original reference ellipsoid, the tunnel inlet ends CP I163, CPI164 (110° 45', 315 m), the exit end CP I165, CP I166 (110° 5', 375 m) are respectively converted to the Wulingshan tunnel independent coordinate system ($L_0 = 110^{\circ}48'$, $H_0 = 434$ m) [9].

Baseline solution and 3D unconstrained adjustment

Independent control network data processing includes baseline vector solution and network adjustment. The baseline vector solution uses GPS random post-processing commercial software. The satellite ephemeris uses the broadcast ephemeris uniformly [10]. The synchronization observation time is not less than 120 min in any period, and the number of effective satellites in any period is not less than 4, and the observation value of the same period is calculated. The data rejection rate is less than 10% [2], and the asc baseline vector file is exported after the solution is completed. When the network adjustment is performed, the asc baseline vector file is imported into the data post-processing software. First, the independent baseline loop and the repeated baseline are calculated. Check that all independent closed loop closure differences and duplicate baselines are within the specification tolerance, and select the network. The three-dimensional rectangular coordinates of the control point CPI165 are unconstrained adjustments for the starting point, confirming that the three-dimensional baseline vector residual is within the specification tolerance.

Checking of start point relative stability

In the Wulingshan tunnel, one or two CPI points are selected for entrance and exit. This time, CPI164, CPI165 and CPI166 are selected, of which CPI164 is located at the tunnel entrance and CPI165 and CPI166 are located at the tunnel exit. Considering the distribution of points (see Figure 1), CP I164 and CP I166 are used to analyse the positional mismatch and the relative accuracy of the side length (points spacing 8 518. 550 1 m). CPI165 is close to CPI166 (points spacing 903. 449 1 m), CPI165 as an auxiliary point, only the azimuth analysis. The plane



coordinates ($L = 110^\circ 48'$, $H = 434$ m) obtained by three-dimensional unconstrained adjustment of CPI164, CPI165 and CPI166 are compared with the conversion results, and the side length between adjacent points is calculated. Azimuth and angle, and comparative analysis, to determine the relative stability and reliability of the three plane control points.

“Two-point method” constraint adjustment

Taking CPI164 and CPI166 as the starting point, the constraint is adjusted by the tunnel independent coordinate system $L = 110^\circ 48'$ and $H = 434$ m. The error of the baseline side azimuth of the weakest edge DGPS05-DGPS06 after adjustment is $MA = 0.83''$, the relative length error of the side length $MS = 0.17$ cm, the relative accuracy is $1/259\,648$ (ie 3.851×10^{-6} , the relative length error of the side length is $<1/250\,000$), which satisfies the accuracy requirements of the high-speed rail first-class GPS network in the specification.

Independent control network reliability analysis

In order to verify the reliability of the independent control network [11], a triangle is selected for each angle of the construction area (tunnel entrance, exit and route) of the Wulingshan tunnel for angle and distance inspection. The test data is shown in Table 4 and Table 5.

Tab. 4 - Comparison of measured side length of total station with GPS side length

Side name	Total station measurement /m	After the projection is corrected /m	GPS point inverse value /m	Mismatch value / mm	Projection length deformation value / (mm /km)
DGPS01 ~CPI164	528. 669 1	528. 668 7	528. 664 9	3. 8	4. 96
DGPS01 ~CPI163	628. 680 9	628. 680 4	628. 676 3	4. 1	4. 54
DGPS02 ~DGPS04	458. 262 6	458. 267 4	458. 269 3	- 1. 9	- 4. 15
DGPS02 ~DGPS03	877. 586 7	877. 595 9	877. 593 8	2. 1	2. 39
DGPS07 ~CPI165	640. 342 3	640. 343 2	640. 345 6	- 2. 4	- 3. 75
DGPS07 ~DGPS08	862. 950 3	862. 951 6	862. 954 5	- 2. 9	- 2. 21

Tab. 5 - Total station measured azimuth and GPS comparison

Corner name	Total station measurement / ($^\circ$ ' '')	GPS coordinate Back calculation / ($^\circ$ ' '')	Mismatch value / ('')	Back point	Measurement station	Front point
DGPS01	200 43 25. 3	200 43 25. 6	- 0. 3	CPI164	DGPS01	CPI163
DGPS02	130 36 58. 1	130 36 56. 7	1. 4	DGPS04	DGPS02	DGPS03
DGPS07	171 25 24. 6	171 25 25. 3	- 0. 7	CPI165	DGPS07	DGPS08

It can be seen from Table 4 that the maximum projection length deformation value of the independent control network is 4.96 mm /km, which meets the requirements of the high-speed rail specification not to be greater than 10 mm /km. Table 5 shows the maximum difference between the total station measurement azimuth and the GPS back-calculated azimuth is $1.4''$, the total station instrument detection data is in good agreement with the GPS data, and the reliability of the Wulingshan tunnel independent control network meets the requirements.



COMPARISON AND ANALYSIS OF NETWORK CONSTRUCTION METHODS WITH ONE POINT - ONE DIRECTION

In order to facilitate comparative analysis, the Wulingshan tunnel independent control network was established in one direction using the same baseline file, starting point and projection parameters. Taking CP I164 as the starting point, CP I166 is the direction point, the orientation $\theta = 125^{\circ}18'22.92''$, the central meridian $L = 110^{\circ}48'$, and the earth height $H = 434$ m. After the one point one direction adjustment [12], the error of the baseline side orientation of the weakest edge DGPS05-DGPS06 is $MA=0.77''$, the relative length error of the side length is $MS=0.15$ cm, and the relative accuracy is 1/294 772 (the relative error is <1 /250 000), which satisfies the accuracy requirements of the high-speed rail first-class GPS network in the specification, the coordinates are poor. See Table 6.

Tab. 6 - Control points poor statistics

Point No.	One point one direction network construction results		Two-point method network construction results		mismatching value	
	X/m	Y/m	North coordinate	East coordinate	dx/mm	dy/mm
CPII64	3 226 587. 404 8	497 361. 112 9	3 226 587. 404 8	497 361. 112 9	0. 0	0. 0
DGPS04	3 226 298. 375 3	497 004. 061 5	3 226 298. 379 4	497 004. 065 6	- 4. 1	- 4. 1
DGPS01	3 226 204. 761 4	496 996. 314 9	3 226 204. 766 4	496 996. 319 2	- 5. 0	- 4. 3
DGPS02	3 226 280. 893 5	496 546. 120 3	3 226 280. 897 3	496 546. 129 9	- 3. 8	- 9. 6
CPII63	3 225 932. 682 3	496 429. 555 6	3 225 932. 690 3	496 429. 566 6	- 8. 0	- 11. 0
DGPS05	3 225 522. 743 0	498 252. 804 4	3 225 522. 755 8	498 252. 794 1	- 12. 8	10. 3
DGPS03	3 225 593. 401 4	496 000. 644 5	3 225 593. 413 6	496 000. 660 4	- 12. 2	- 15. 9
DGPS06	3 225 096. 947 1	498 321. 623 5	3 225 096. 965 0	498 321. 612 4	- 17. 9	11. 1
CPII65	3 222 482. 730 9	503 930. 822 2	3 222 482. 779 0	503 930. 745 3	- 48. 1	76. 9
DGPS07	3 221 892. 425 6	504 178. 999 7	3 221 892. 480 9	504 178. 919 8	- 55. 3	79. 9
CPII66	3 221 664. 065 2	504 312. 956 3	3 221 664. 123 2	504 312. 874 8	- 58. 0	81. 5
DGPS08	3 221 155. 679 5	504 628. 346 3	3 221 155. 742 9	504 628. 261 0	- 63. 4	85. 3

It can be seen from the analysis that the same baseline calculation file and projection parameters, the one-point direction and the "two-point method" can meet the accuracy requirements of the high-speed rail first-class GPS network, and the control point coordinates are different: the reference point difference is small, the direction point difference large, and increasing with distance, reaching a maximum at the exit end of the tunnel. In combination with Table 6, it can be seen that the DGPS08 (distance from the reference point of about 9.1 km) has a poor coordinate Δx of -63. 4 mm and Δy of 85. 3 mm. The analysis shows that the coordinate is poorly affected by the distance and orientation [13], CPII64 CPII66 coordinate orientation $\theta = 125^{\circ}18'22.92''$, located in the second quadrant, see Figure 2, the control point difference Δx is negative, Δy is a positive value and both increase with distance. Combined with the mid-line data of the Wulingshan tunnel line, the angle between the center line point tangent of the DGPS08 corresponding line and the reference direction of the control network is $61^{\circ}43'08''$, and the calculated DGPS08 corresponding center line point is 50.4 mm left, resulting in a long chain 93. 6 mm, the lateral deviation has already affected the tunnel exit connecting section, and needs to be



controlled by the control network rotation, otherwise it will cause the structure of the tunnel exit section to be displaced and connected.

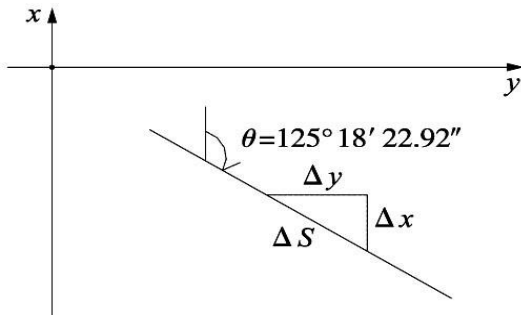


Fig. 2 - Azimuth versus coordinate influence

TRANSVERSE PENETRATION ERROR PREDICTION ANALYSIS

The influence of the control network outside the tunnel on the lateral penetration error is related to the point error of the entry point, the azimuth error of the entry hole, the angle between the entry point and the connection point of the penetration point and the tangent of the penetration point line [14]. After the establishment of the outside control network, the penetration error prediction formula in the "High-speed Railway Engineering Measurement Specification" (TB10601-2009) should be calculated to verify whether the accuracy of the outside control network meets the requirements of the penetration measurement.

$$M^2 = \sigma_{\Delta x}^2 \cos^2 \alpha_F + \sigma_{\Delta y}^2 \sin^2 \alpha_F + \sigma_{\Delta x \Delta y}^2 \sin^2 2 \alpha_F$$

Where $\sigma_{\Delta x}$, $\sigma_{\Delta y}$, $\sigma_{\Delta x \Delta y}$ — the variance and covariance of the x, y coordinate deviations derived from the entrance and exit to the point of penetration;

α_F — penetration plane orientation.

The Wulingshan Tunnel is 9. 044 km long and is constructed separately from the entrance, levelling and exit planes. The flat guide is located at the entrance of the tunnel and is placed at the entrance of the tunnel at 1 km. Therefore, it is included in the tunnel entrance. It is estimated that the tunnel entrance and exit will be about 4. 5 km, and the middle part of the tunnel will be DK239 + 013 as the pre-measurement. The entrance point of the tunnel entrance is DGPS02 and the direction is DGPS03. The entrance point of the tunnel exit is DGPS07, and the orientation point is CP I165. The tunnel transverse penetration error is expected [15] see Table 7.

The estimated lateral penetration error of the Wulingshan Tunnel is 10.1 mm, which is less than the error value of 45 mm [2] in the case of $7 \text{ km} \leq L < 10 \text{ km}$ in the High-Speed Railway Engineering Measurement Specification (TB10601-2009), which satisfies the requirements.

Tab. 7- Estimation of horizontal penetration measurement of Wulingshan tunnel

Penetration mileage	Lateral penetration error /mm	Entrance entry point	Entrance orientation point	exit entry point	Exit orientation point	direction
DK239+013	10. 1	DGPS02	DGPS03	DGPS07	CPI165	33 01 22. 9

CONCLUSION

The "two-point method" can not only achieve sufficient accuracy, meet the tunnel penetration requirements, but also effectively solve the problems of large lateral deviation and long



and short chains. The "two-point method" can not only achieve sufficient accuracy, meet the tunnel penetration requirements, but also effectively solve the problems of large lateral deviation and long and short chains.

ACKNOWLEDGEMENT

Authors are thankful to the anonymous reviewers for their valuable comments.

REFERENCES

- [1] National Railway Administration. TB 10003—2016 Railway Tunnel Design Specification [S]. Beijing: China Railway Publishing House, 2017
- [2] Ministry of Railways of the People's Republic of China. TB 10601—2009 High-speed railway engineering measurement specification [S]. Beijing: China Railway Publishing House, 2009
- [3] Yang Liu, Zuo Zhigang. Tunnel independent control network construction method [J]. Railway Investigation, 2011(4): 21-23.
- [4] Ye Changyi. Extra-long tunnel plane independent control network layout [J]. Railway Construction Technology, 2013(3) : 95-98
- [5] Yang Xuefeng, Liu Chenglong. Network construction method for independent control network of high-speed railway tunnel group[J]. Journal of Railway Science and Engineering, 2013(6) : 79-83
- [6] Hong Jianghua, Shi Debin, et al. The measurement and accuracy analysis of the plane GPS control network of Xuefeng Mountain long tunnel group [J]. Railway Survey, 2012(1) : 21-24
- [7] Zhao Junsheng, Liu Yanchun, et al. Discussion on the length deformation of Gaussian projection [J]. Ocean Mapping, 2007(3): 9-11
- [8] Kong Xiangyuan, Guo Jiming. Control surveying [M]. Wuhan: Wuhan University Press, 2015: 99-100
- [9] Feng Difei, Hu Shengwu. Research on VB-based Gaussian Projection Coordinates Swap Program [J]. Journal of Henan Urban Construction College, 2015(4) : 38-43
- [10] National Quality Supervision, Inspection and Quarantine Bureau of the People's Republic of China. GB / T 18314—2009 Global Positioning System (GPS) Measurement Specification [S]. Beijing: China Standards Press, 2009
- [11] Xia Wei. GPS control network optimization design and data processing research [D]. Changchun: Jilin University, 2015
- [12] Ma Yafei, Zheng Zhifeng. The application of point one direction method in establishing independent coordinate system of tunnel [J]. Surveying and Mapping Technology and Equipment, 2017(4) : 65-67
- [13] Lu Chao. The application of vector inner and outer product in the inverse calculation of linear coordinate azimuth [J]. Henan Science and Technology, 2015(18) : 80-81
- [14] Fu Hongping, Guo Jiming, et al. Research on prediction method of special tunnel penetration error [J]. Bulletin of Surveying and Mapping, 2015(2) : 80-83
- [15] Wang Zhifeng. Discussion on calculation method of transverse penetration error of GPS tunnel control network [J]. Geospatial Information, 2017(1) : 102-103